12-2019

Multi-Scale Assessment of Binding Geometries and Energetics of Aqueous Phase Reforming of Glycerol and Methanol: Towards Realistic, Accurate, and Computationally Tractable Strategies

Tianjun Xie
Clemson University

MULTI-SCALE ASSESSMENT OF BINDING GEOMETRIES AND ENERGETICS OF AQUEOUS PHASE REFORMING OF GLYCEROL AND METHANOL: TOWARDS REALISTIC, ACCURATE, AND COMPUTATIONALLY TRACTABLE STRATEGIES.

A Dissertation
Presented to
the Graduate School of
Clemson University

In Partial Fulfillment
of the Requirements for the Degree
Doctor of Philosophy
Chemical Engineering

---

by
Tianjun Xie
December 2019

Accepted by:
Dr. Rachel Getman, Committee Chair
Dr. David Bruce
Dr. Sapna Sarupria
Dr. Lindsay Shuller-Nickles

Abstract

Current biorefineries produce many downstream biomass wastes from conversion of polysaccharide feedstocks, among which are carbohydrates and oxygenates, which are often not collected for further processing. Using aqueous catalytic systems can help reduce the waste and add more value to the entire process. However, this biomass treatment is highly dependent on specialized and optimized catalysts which are lacking. To-date, most catalyst technology development is done in the petroleum industry, where the reactions of interest mostly occur in the gas phase or in non-polar solvents.

Insight into the influence of polar solvents on the conversions of biomass wastes is needed in order to optimize the catalysts and reaction systems that operate under such conditions. To acquire this insight, it is our goal to elucidate the mechanisms of two practical aqueous phase biomass conversions on an atomistic/molecular level, specifically methanol oxidation and glycerol reforming. Methanol and glycerol are important intermediates in biomass processing and can be further converted into hydrogen, alkanes, and specialty chemicals. They are good representations in terms of computational models of primary and secondary sugar alcohols, which are predominant products in biomass treatment, for example cellulose conversions. Methanol oxidation and glycerol reforming, as well as other aqueous biomass conversion reactions, are currently catalyzed by heterogeneous catalysts commonly containing Pt and other noble metals. These materials contribute to high catalyst costs. Further, without fundamental understanding of the molecular level phenomena that drive catalytic performance, it will remain difficult to develop catalysts that are active and selective for desired products. These things inhibit the widespread use of biomass as a feedstock for fuels and other chemical applications. Further, a major challenge in designing new catalysts for this type of process, as mentioned above, is that those reactions are carried out in the liquid phase, and the large density of solvent molecules surrounding the catalyst surface makes it difficult to identify important

molecular-level phenomena in experimental and computational settings.

Elucidating such phenomena is crucial to designing new low-cost catalysts with desired metrics such as selectivity, yield, and turnover rates. The catalyst design cycle begins with firstly getting a firm grip on current catalyst functionality. Due to the complexity in surface chemistry and indication from experimental results on solvent effects, there is a critical need to incorporate the aqueous environment into mechanistic studies and catalyst design. In the absence of such efforts, catalyst development for liquid phase reactions will remain difficult. This project employs a hierarchy of molecular-level modeling to identify the influence of solvent on the mechanism of glycerol reforming and the active sites in methanol oxidation. Quantum mechanics combined with molecular dynamics are used to model how the aqueous environment influences catalytic energetics, and microkinetic models are used to determine the overall solvent influence on reaction mechanisms. Finally, quantum simulations are compared with frequencies from attenuated total reflectance infrared (ATR-IR) spectroscopy in order to identify the precise active sites and present intermediates in the methanol oxidation pathway.

Dedication

I would like to dedicate this work to my family: my parents, Zhikun and Yinfen; my in-laws: Robert and Betty; and my wife: Savannah.

Acknowledgments

I would like to acknowledge the many people for their support along my 5-year academic journey. Specifically, I would like to thank: Dr. Rachel B. Getman, for being a great advisor and supporting me over these years through my research and my personal life. Without your help and guidance, I would not have achieved as much as I did within my PhD span.

Dr. David Bruce, Dr. Sapna Sarupria, and Dr. Lindsay Shuller-Nickles for accepting to be on my committee and for providing guidance through the processes of mid-term GS2 meeting and completing my academic dissertation.

Terri McAllister, Joy Rodatz, Bill Coburn, and Diana Stamey for their support with all of the administrative efforts that are related to graduate students. Especially thanks to Diana for her help of the graduation process.

Cameron Bodenschatz, Jiazhou Zhu, Xiaohong Zhang, Dr. Steven Pellizzeri, Dr. Paul Meza-Morales, Hafeera Shabbir, and Stephen Vicchio for being great lab mates and for providing thoughtful discussions, instructions, and critiques.

The graduate students in the Chemical and Biomolecular Engineering Department that made graduate school in Clemson such a great experience.

The Clemson Cyberinfrastructure and Technology Integration group for their management and support of the Palmetto Cluster, and especially Marcin Ziolkowski, and Ashwin Srinath, who were very helpful with compiling and troubleshooting software on Palmetto. Their assistance was highly valuable in being able to complete the work that went into this dissertation.

Clemson University and the National Science Foundation (Award#'s CBET- 1438325 and 1764296) for the financial support.

Contents

List of Tables

List of Figures

Chapter 1

Introduction and Background

1.1 Motivation

In order to transform the energy dependencies from traditional fossil fuel such as coal and oil, more and more countries and companies are seeking alternative sources of energy, particularly renewable sources such as biomass. Two biomass feedstocks of interest are methanol (CH_3OH) and glycerol ($C_3H_8O_3$), as they are byproducts in the production of biodiesel. It was estimated that the production of glycerol globally would reach 3 megatons in 2020 [1], whereas the world demand for glycerol would be less than 500 kilotons [2]. With such a great surplus, it is practical to seek ways to convert glycerol into useful products. One method for converting these feedstocks is aqueous phase reforming (APR). In APR, polyols [3–9], bio-oil [10, 11], cellulose [12, 13], and different types of ligno-cellulosic biomass [14, 15] can be converted to H_2 (g) and CO_2 (g) over supported metal catalysts in aqueous conditions [16–19]. The H_2 produced could be used in a biorefinery, for example, supplying the H_2 (g) needed for hydrodeoxygenation of biomass derivatives such as phenol (i.e., $C_6H_5OH + H_2 \rightarrow C_6H_6 + H_2O$) [20]. A diversity of catalytic systems, mainly based on transition VIII group metals, have been described in the literature as good candidates for APR of oxygenated hydrocarbons [21–23]. Pt-based catalysts have been shown to be the most effective among mono-metallic catalysts in terms of activity and selectivity toward H_2- rich gas in terms of selectivity [18, 23–26].

1.1.1 Aqueous Phase Reforming

In particular, APR has great potential in making the transition from nonrenewable hydrocarbon feedstocks to renewable biomass feedstocks. In addition to the utilization of renewable feedstocks, this method eliminates the need to vaporize water and the oxygenated hydrocarbon (which reduces the energy requirements). Further, due to the relatively low temperature, the production of H_2 and CO_2 can be enhanced by water-gas shift reactions (WGS), leading to low levels of CO [3, 23, 27, 28]. Previous work has laid groundwork of hydrogen production through APR of biomass-derived oxygenated hydrocarbons (such as methanol, ethylene glycol, glycerol, sorbitol, and glucose) at low temperatures (e.g., 500 K) over supported Pt catalysts [3, 23]. Pt catalysts supported on solid basic oxides exhibit excellent activity in APR [29] and most of the publications on APR are focused on Pt supported on γ-Al_2O_3, due to its high selectivity to H_2 production [3, 30, 31]. However, the expansion of this reforming technique is inhibited by the high cost of the noble metal based catalysts. Moreover, to date, H_2 yields have been low [32]. The APR process is highly dependent on the catalytic systems and the reaction conditions [5, 33]. A goal within the catalyst research community is to devise newer catalysts in order to address those problems. In order to achieve this goal, it requires improved understanding of the APR catalytic mechanism.

From a big-picture standpoint, the mechanism of APR involves three major branches: dehydrogenation (R-H* + * $\rightarrow$ R* + H*, where * are catalyst sites), decarbonylation (R-CO* + * $\rightarrow$ R* + CO*), and WGS (CO* + H_2O $\rightarrow$ * + CO_2 + H_2). However, elucidating individual steps in the different branches is not straightforward, even with experimental attempts using operando techniques [34–36]. Computational work can help shed more light on the reaction mechanism. Doing so requires overcoming issues with respect to large sizes and complex structures of APR feed molecules (which result in large reaction networks and a great number of possible catalytic intermediates) as well as the aqueous reaction conditions themselves [37, 38]. Further, the catalytic support also impacts the mechanism, with different supports having different effects [39]. In fact, there is a significant need to identify computational strategies that are able to identify and separate different phenomena such as catalyst performance, support effects, and influence of an aqueous environment, in order to gauge their influences on reaction mechanisms, generally.

1.2 Computational Studies on Catalysis

About 90% of chemical processes use catalysis [40, 41], but there is still great potential for further catalyst development. Over the last century, the search for novel catalysts was mostly based on extensive experiments guided by chemical intuition and experience. Developing next generation catalysts and catalytic processes will require a dedicated effort over an extended period of time. This effort requires a detailed look at the catalyst performance as a function of many variables such as catalyst composition, reacting chemical molecular and spatial arrangements, relative energies, etc. These are fundamental aspects that are central to catalyst design. The use of computational approaches can provide extensive knowledge on these perspectives and can overcome limitations that exist in experimental observations, by achieving results based from both qualitative and quantitative measurements, and making predictions at a detailed often molecular level.

Needless to say, there have been many computational studies that provide insight into a variety of chemical reactions. In Fig. 1.1, it shows the the exponential growth of publications citations relevant to computational chemistry.

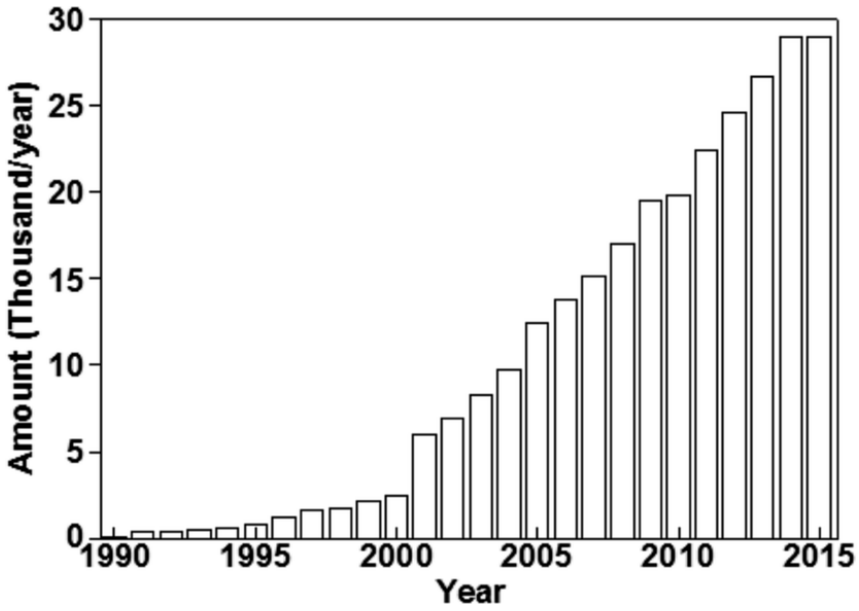

Figure 1.1: The growth of applications of calculations of metal complexes based on density functional theory over the past two decades is reflected by the exponentially increasing number of citations. Adapted from [42] with permission from The Royal Society of Chemistry.

APR process can also benefit from the aid of computational catalyst design. Currently, the

majority of the commercial catalysts for APR are based on platinum Pt, due to its good level of activity and selectivity in catalyzing aqueous phase reforming of glycerol and other sugar alcohol species [18, 37, 43–49]. However, the drawback of the noble metal cost and catalyst deactivation call for more improvement on existing catalysts and for new catalyst. These efforts require a good understanding of the complicated kinetics and mechanisms of heterogeneously catalyzed chemical reactions in the aqueous phase, which are still not fully understood. Previous exploration on this subject are visionary [34, 35] while current experimental techniques still often face obstacles in observing chemical species and identifying chemical reaction mechanisms at a molecular level. In this case, computational catalyst design provides possible solutions to model specific reaction species and steps in great details, which can provide more insight of reaction mechanism.

1.2.1 Challenges in Aqueous Phase Catalysis Modeling

In aqueous phase catalysis, the reaction mostly occurs at the interface near the solid catalyst surface, but the experimentally observed quantity is the overall, macroscopic bulk representation of those micro-level reactions. Moreover, it is unclear how exactly the reactions take place in the actual aqueous environment, since the water environment can play a role in the aqueous phase catalysis in the circumstances where water either acts as a solvent or becomes active in reactions. Such mechanistic and chemical properties of water not only influences elementary steps, but can also influence the final observable reaction metrics such as turnover rates, making them different than their analogs carried out in gaseous (vacuum) environment. However, due to the complexity of the reaction mechanism and reaction conditions, as well as the uncertainty of the constantly fluctuating water environment, understanding in this area is still lacking. The challenges arises primarily from,

1. These phenomena occur at the molecular level, and they are significantly affected by variability in catalyst composition, reaction conditions, and other tunable parameters;

2. In aqueous phase heterogeneous catalysis, there are many puzzle pieces in the role of water left to be elucidated [50, 51]. The aqueous phase environment itself introduces significant complexity to the system, which needs to be addressed properly, since water molecules influence binding energies of adsorbate and geometries, hence can alter reaction rates and pathways. Moreover, when water becomes activated, it can even participate in reactions, which can influence reaction energies and kinetic energies hence influencing part of the surface chemistry.

3. The computational techniques that are needed to provide good understanding of molecular level processes are computationally intensive, due to the needs to use quantum mechanics to compute system energies accurately (of bond breaking and forming processes) plus the need to incorporate the configurational disorder of the aqueous phase environment (meaning calculations of multiple configurations of water are needed) at realistic temperatures.

1.2.2 Overcoming Computational Obstacles

Computational strategies have contributed to understanding the mechanism of APR at molecular level details. For example, density functional theory (DFT) studies have shown that catalytic glycerol reforming follows the path α-carbon dehydrogenation $\rightarrow$ β-carbon dehydrogenation $\rightarrow$ hydroxly group dehydrogenation $\rightarrow$ decarbonlyation under vacuum [52–58]. Our group is particularly interested in how the water environment influences the catalysis. Water is known to influence catalysis in multiple ways, including altering the energies of catalytic species via hydrogen bonding and other interactions (e.g., van der Waals effects) [51, 59–73], influencing the dominant reaction pathway [60, 61, 68–70, 74–76], and participating in the catalytic chemistry (e.g., by enabling proton transfer) [74, 77]. These phenomena complicate computational attempts to simulate catalytic mechanisms under aqueous phase.

To address these challenges, our group has previously developed a multi-scale strategy for simulating catalysis under aqueous conditions [78]. In our studies, the reacting species, such as glycerol, are "large" molecules that can have a large number of possible reaction intermediates and reaction pathways. This raises a practical problem in examining all chemical species and chemical reactions for each, since each of them needs to average over an ensemble of aqueous phase surroundings. In fact, using the previously developed strategy from our group, even when carried out in a highly-automated and paralleled way [79], investigating one reaction intermediate would take about a week to get the thermodynamic energies calculated. Given that glycerol APR can include dehydrogenation, decarbonylation, dehydration, hydrolysis, water gas shift and other processes [80], to study the entire reaction network, including multiple configurations of liquid H_2O molecules for each reaction intermediate and transition state, would require a very significant amount of time and effort. Due to the large reaction network and to the need to properly model and study it in liquid conditions, we are seeking ways to reduce the computational expense of performing simulations of heterogeneously catalyzed reactions in the aqueous phase. This thesis presents our efforts aimed

at solving these puzzles with affordable computational expense by employing multi-scale strategies, coupled with scaling relations, which significantly reduce the computational expense while maintaining the results within DFT accuracy. More specifically, we developed linear scaling relations for rapid estimation of reaction energies of dehydrogenation reactions under glycerol APR and showed that the estimated results are within DFT accuracy. Further, we developed transition state scaling relations for rapid estimation of activation energies, (which are often acquired by very computationally intensive calculations) among dehydrogenation, decarbonylation, and hydrolysis reactions under glycerol APR reaction network, and we also showed this method to retain good DFT accuracy.

1.3 Dissertation Outline

The thesis will introduce our work towards helping reveal the surface chemistry of APR processes using computational approaches that are novel, accurate and efficient. The thesis contains five chapters, which are introduction and background chapter that briefly touches upon the motivation and potential significance of the projects; methodology chapter that explains the methods and tools that are related to the aqueous phase catalysis research; three technical chapters that aiming to explore thermodynamics, kinetics using established multi-scale modeling methods that are coupled with scaling relations; and application of multi-scale modeling methods in modeling realistic systems.

Chapter 2, Multi-scale Simulation Strategy and Its Application, discusses the current catalysts models in great detail. Detailed computational parameters are presented in this chapter. The goal of this chapter is to lay out the methodology of multi-scale modeling methods, which are used extensively in the following technical chapters.

Chapter 3, A DFT and MD Study of Aqueous-phase Dehydrogenation of Glycerol on Pt (1 1 1): Comparing Chemical Accuracy versus Computational Expense in Different Methods for Calculating Aqueous-phase System Energies, discusses the methodology that is developed to access thermodynamics of dehydrogenation reactions of glycerol APR. Specifically, the reaction species and their related energies are assessed by calculating reaction energies using a multi-scale modeling method named LSR/MD method.

Chapter 4, Insights into the Roles of Water on the Aqueous Phase Reforming of Glycerol, reaction network and species are assessed by calculating kinetic energies using the multi-scale mod-

eling method and dimer calculations. Later in this chapter, another type of scaling relation named transition state scaling relations are introduced and examined for accurate and efficient estimation of kinetic energies in the aqueous phase. Chapter 3 and Chapter 4 not only address the need to incorporate the liquid reaction environment, but additionally propose methods to decrease the expense of simulating relatively large catalytic intermediates.

Chapter 5, Computational Modeling of Methanol Decomposition on Pt Catalyst Supported by Alumina, presents our study outcome of reaction thermodynamics of all the chemical species binding to active sites of the Pt(1 1 1) and supported Pt. In addition, IR spectra data is compared between computed and experimental results. Conclusions of preferred binding sites and dominant species on the surface are suggested.

Conclusions and recommendations, along with appendices, can be found near the end of the thesis.

In all, this dissertation aims to shed more light upon on complicated reactions and reaction intermediates. The foci of the thesis are addressing practical problems in modeling complicated aqueous phase systems, reducing computational expense while maintaining the chemical accuracy, and validating of the computed results against real experimental conclusions. We hope this work can contribute to the computational catalysis community, in an effort towards guiding and accelerating new catalyst design.

1.4 Reference

[1] Muhammad Ayoub and Ahmad Zuhairi Abdullah. "Critical review on the current scenario and significance of crude glycerol resulting from biodiesel industry towards more sustainable renewable energy industry". *Renewable and Sustainable Energy Reviews* 16.5 (2012), 2671–2686.

[2] Yu-Chuan Lin. "Catalytic valorization of glycerol to hydrogen and syngas". *International Journal of hydrogen energy* 38.6 (2013), 2678–2700.

[3] JW Shabaker, RR Davda, GW Huber, RD Cortright, and JA Dumesic. "Aqueous-phase reforming of methanol and ethylene glycol over alumina-supported platinum catalysts". *Journal of Catalysis* 215.2 (2003), 344–352.

[4] Rupali R Davda and James A Dumesic. "Renewable hydrogen by aqueous-phase reforming of glucose". *Chemical Communications* 1 (2004), 36–37.

[5] A Iriondo, JF Cambra, VL Barrio, MB Guemez, PL Arias, MC Sanchez-Sanchez, RM Navarro, and JLG Fierro. "Glycerol liquid phase conversion over monometallic and bimetallic catalysts: Effect of metal, support type and reaction temperatures". *Applied Catalysis B: Environmental* 106.1-2 (2011), 83–93.

[6] Alexey V Kirilin, Anton V Tokarev, Leonid M Kustov, Tapio Salmi, J-P Mikkola, and Dmitry Yu Murzin. "Aqueous phase reforming of xylitol and sorbitol: comparison and influence of substrate structure". *Applied Catalysis A: General* 435 (2012), 172–180.

[7] Toshiaki Nozawa, Yuichi Mizukoshi, Akihiro Yoshida, and Shuichi Naito. "Aqueous phase reforming of ethanol and acetic acid over TiO2 supported Ru catalysts". *Applied Catalysis B: Environmental* 146 (2014), 221–226.

[8] Yi Wei, Hanwu Lei, Yupeng Liu, Lu Wang, Lei Zhu, Xuesong Zhang, Gayatri Yadavalli, Birgitte Ahring, and Shulin Chen. "Renewable hydrogen produced from different renewable feedstock by aqueous-phase reforming process". *Journal of Sustainable Bioenergy Systems* 4.2 (2014), 113.

[9] Min-Cheol Kim, Tae-Wan Kim, Hyung Ju Kim, Chul-Ung Kim, and Jong Wook Bae. "Aqueous phase reforming of polyols for hydrogen production using supported PtFe bimetallic catalysts". *Renewable energy* 95 (2016), 396–403.

[10] Chunyan Pan, Aiping Chen, Zhen Liu, Ping Chen, Hui Lou, and Xiaoming Zheng. "Aqueous-phase reforming of the low-boiling fraction of rice husk pyrolyzed bio-oil in the presence of platinum catalyst for hydrogen production". *Bioresource technology* 125 (2012), 335–339.

[11] Aiping Chen, Ping Chen, Danyan Cao, and Hui Lou. "Aqueous-phase reforming of the low-boiling fraction of bio-oil for hydrogen production: the size effect of Pt/Al2O3". *International Journal of Hydrogen Energy* 40.43 (2015), 14798–14805.

[12] Guodong Wen, Yunpeng Xu, Zhusheng Xu, and Zhijian Tian. "Direct conversion of cellulose into hydrogen by aqueous-phase reforming process". *Catalysis Communications* 11.6 (2010), 522–526.

[13] Tomáš Soták, Milan Hronec, Ivo Vávra, and Edmund Dobročka. "Sputtering processed tungsten catalysts for aqueous phase reforming of cellulose". *International Journal of Hydrogen Energy* 41.47 (2016), 21936–21944.

[14] Bahar Meryemoglu, Burcak Kaya, Sibel Irmak, Arif Hesenov, and Oktay Erbatur. "Comparison of batch aqueous-phase reforming of glycerol and lignocellulosic biomass hydrolysate". *Fuel* 97 (2012), 241–244.

[15] Burçak Kaya, Sibel Irmak, Arif Hasanoğlu, and Oktay Erbatur. "Developing Pt based bimetallic and trimetallic carbon supported catalysts for aqueous-phase reforming of biomass-derived compounds". *International Journal of Hydrogen Energy* 40.10 (2015), 3849–3858.

[16] George W Huber, Randy D Cortright, and James A Dumesic. "Renewable alkanes by aqueous-phase reforming of biomass-derived oxygenates". *Angewandte Chemie* 116.12 (2004), 1575–1577.

[17] George W Huber, Juben N Chheda, Christopher J Barrett, and James A Dumesic. "Production of liquid alkanes by aqueous-phase processing of biomass-derived carbohydrates". *Science* 308.5727 (2005), 1446–1450.

[18] R Davda Cortright, RR Davda, and James A Dumesic. "Hydrogen from catalytic reforming of biomass-derived hydrocarbons in liquid water". *Materials For Sustainable Energy: A Collection of Peer-Reviewed Research and Review Articles from Nature Publishing Group*. World Scientific, 2011, 289–292.

[19] Juan Carlos Serrano-Ruiz, Rafael Luque, and Antonio Sepúlveda-Escribano. "Transformations of biomass-derived platform molecules: from high added-value chemicals to fuelsvia aqueous-phase processing". *Chem. Soc. Rev.* 40 (11 2011), 5266–5281.

[20] Quan Bu et al. "A review of catalytic hydrodeoxygenation of lignin-derived phenols from biomass pyrolysis". *Bioresource Technology* 124 (2012), 470–477.

[21] RR Davda, JW Shabaker, GW Huber, RD Cortright, and James A Dumesic. "A review of catalytic issues and process conditions for renewable hydrogen and alkanes by aqueous-phase reforming of oxygenated hydrocarbons over supported metal catalysts". *Applied Catalysis B: Environmental* 56.1-2 (2005), 171–186.

[22] Juben N Chheda, George W Huber, and James A Dumesic. "Liquid-phase catalytic processing of biomass-derived oxygenated hydrocarbons to fuels and chemicals". *Angewandte Chemie International Edition* 46.38 (2007), 7164–7183.

[23] RR Davda, JW Shabaker, GW Huber, RD Cortright, and James A Dumesic. "Aqueous-phase reforming of ethylene glycol on silica-supported metal catalysts". *Applied Catalysis B: Environmental* 43.1 (2003), 13–26.

[24] MA Vannice. "The catalytic synthesis of hydrocarbons from H2CO mixtures over the Group VIII metals: V. The catalytic behavior of silica-supported metals". *Journal of Catalysis* 50.2 (1977), 228–236.

[25] John H Sinfelt and David JC Yates. "Catalytic hydrogenolysis of ethane over the noble metals of Group VIII". *Journal of Catalysis* 8.1 (1967), 82–90.

[26] R Alcala, M Mavrikakis, and James A Dumesic. "DFT studies for cleavage of C-C and C-O bonds in surface species derived from ethanol on Pt (111)". *Journal of Catalysis* 218.1 (2003), 178–190.

[27] George W Huber, John W Shabaker, Steven T Evans, and James A Dumesic. "Aqueous-phase reforming of ethylene glycol over supported Pt and Pd bimetallic catalysts". *Applied Catalysis B: Environmental* 62.3-4 (2006), 226–235.

[28] Aysegul Ciftci, DAJ Michel Ligthart, A Oben Sen, Arno JF van Hoof, Heiner Friedrich, and Emiel JM Hensen. "Pt-Re synergy in aqueous-phase reforming of glycerol and the water–gas shift reaction". *Journal of catalysis* 311 (2014), 88–101.

[29] Yong Guo, Muhammad Usman Azmat, Xiaohui Liu, Yanqin Wang, and Guanzhong Lu. "Effect of support's basic properties on hydrogen production in aqueous-phase reforming of glycerol and correlation between WGS and APR". *Applied energy* 92 (2012), 218–223.

[30] Nianjun Luo, Xianwen Fu, Fahai Cao, Tiancun Xiao, and Peter P Edwards. "Glycerol aqueous phase reforming for hydrogen generation over Pt catalyst–Effect of catalyst composition and reaction conditions". *Fuel* 87.17-18 (2008), 3483–3489.

[31] Kamila Koichumanova, Anna Kaisa K Vikla, Dennis JM de Vlieger, Kulathuiyer Seshan, Barbara L Mojet, and Leon Lefferts. "Towards stable catalysts for aqueous phase conversion of ethylene glycol for renewable hydrogen". *ChemSusChem* 6.9 (2013), 1717–1723.

[32] Hernán Antonio Duarte, Maria Eugenia Sad, and Carlos Rodolfo Apesteguı'a. "Bio-hydrogen production by APR of C2-C6 polyols on Pt/Al2O3: Dependence of H2 productivity on metal content". *Catalysis Today* 296 (2017), 59–65.

[33] I Coronado, M Stekrova, M Reinikainen, P Simell, Leonardus Lefferts, and J Lehtonen. "A review of catalytic aqueous-phase reforming of oxygenated hydrocarbons derived from biorefinery water fractions". *International journal of hydrogen energy* 41.26 (2016), 11003–11032.

[34] A Wawrzetz, B Peng, A Hrabar, A Jentys, AA Lemonidou, and JA Lercher. "Towards understanding the bifunctional hydrodeoxygenation and aqueous phase reforming of glycerol". *Journal of Catalysis* 269.2 (2010), 411–420.

[35] Rong He, Rupali R Davda, and James A Dumesic. "In Situ ATR-IR Spectroscopic and Reaction Kinetics Studies of Water- Gas Shift and Methanol Reforming on Pt/Al2O3 Catalysts in Vapor and Liquid Phases". *The Journal of Physical Chemistry B* 109.7 (2005), 2810–2820.

[36] Debdut Roy, Bala Subramaniam, and Raghunath V Chaudhari. "Aqueous phase hydrogenolysis of glycerol to 1, 2-propanediol without external hydrogen addition". *Catalysis Today* 156.1-2 (2010), 31–37.

[37] John W Shabaker and James A Dumesic. "Kinetics of aqueous-phase reforming of oxygenated hydrocarbons: Pt/Al2O3 and Sn-modified Ni catalysts". *Industrial & engineering chemistry research* 43.12 (2004), 3105–3112.

[38] Liang Zhang, Ayman M Karim, Mark H Engelhard, Zhehao Wei, David L King, and Yong Wang. "Correlation of Pt–Re surface properties with reaction pathways for the aqueous-phase reforming of glycerol". *Journal of Catalysis* 287 (2012), 37–43.

[39] Guodong Wen, Yunpeng Xu, Huaijun Ma, Zhusheng Xu, and Zhijian Tian. "Production of hydrogen by aqueous-phase reforming of glycerol". *International Journal of Hydrogen Energy* 33.22 (2008), 6657–6666.

[40] B Mile. "CATALYST STUDIES: CHROMATOGRAPHY" (2000).

[41] RD Magazine. "Recognizing the Best in Innovation: Breakthrough Catalyst". *R&D Mag* (2005).

[42] Shi-Chao Qi, Jun-ichiro Hayashi, and Lu Zhang. "Recent application of calculations of metal complexes based on density functional theory". *RSC Advances* 6.81 (2016), 77375–77395.

[43] Orest Skoplyak, Mark A. Barteau, and Jingguang G. Chen. "Reforming of Oxygenates for H2 Production: Correlating Reactivity of Ethylene Glycol and Ethanol on Pt(111) and Ni/Pt(111) with Surface d-Band Center". *The Journal of Physical Chemistry B* 110.4 (2006), 1686–1694.

[44] Jesse R McManus, Weiting Yu, Michael Salciccioli, Dionisios G Vlachos, Jingguang G Chen, and John M Vohs. "Biomass-derived oxygenate reforming on Pt (111): A demonstration of surface science using d-glucose and its model surrogate glycolaldehyde". *Surface Science* 606.23-24 (2012), L91–L94.

[45] Kazuhiro Takanabe, Ken-Ichi Aika, K. Seshan, and Leon Lefferts. "Mechanistic Aspects of Catalytic Steam Reforming of Biomass-related Oxygenates". *Topics in Catalysis* 49.1 (May 2008), 68.

[46] Heiko Jacobsen. ""Heterogreeneous" chemistry: Catalysts for hydrogen production from biomass". *Angewandte Chemie International Edition* 43.15 (2004), 1912–1914.

[47] Qian Xu, Yi Ma, Jing Zhang, Xiuli Wang, Zhaochi Feng, and Can Li. "Enhancing hydrogen production activity and suppressing CO formation from photocatalytic biomass reforming on Pt/TiO2 by optimizing anatase–rutile phase structure". *Journal of catalysis* 278.2 (2011), 329–335.

[48] Lili Lin et al. "Low-temperature hydrogen production from water and methanol using Pt/α-MoC catalysts". *Nature* 544.7648 (2017), 80.

[49] Aysegul Ciftci, DAJ Michel Ligthart, and Emiel JM Hensen. "Influence of Pt particle size and Re addition by catalytic reduction on aqueous phase reforming of glycerol for carbon-supported Pt (Re) catalysts". *Applied Catalysis B: Environmental* 174 (2015), 126–135.

[50] Chaoquan Hu, Siu-Wa Ting, Kwong-Yu Chan, and Wei Huang. "Reaction pathways derived from DFT for understanding catalytic decomposition of formic acid into hydrogen on noble metals". *International Journal of Hydrogen Energy* 37.21 (2012), 15956–15965.

[51] Yeohoon Yoon, Roger Rousseau, Robert S Weber, Donghai Mei, and Johannes A Lercher. "First-principles study of phenol hydrogenation on Pt and Ni catalysts in aqueous phase". *Journal of the American Chemical Society* 136.29 (2014), 10287–10298.

[52] Y. Chen, M. Salciccioli, and D. G. Vlachos. "An Efficient Reaction Pathway Search Method Applied to the Decomposition of Glycerol on Platinum". *The Journal of Physical Chemistry C* 115.38 (2011), 18707–18720.

[53] Michael Salciccioli, Weiting Yu, Mark A. Barteau, Jingguang G. Chen, and Dionisios G. Vlachos. "Differentiation of O-H and C-H bond scission mechanisms of ethylene glycol on Pt and Ni/Pt using theory and isotopic labeling experiments". *Journal of the American Chemical Society* 133.20 (2011), 7996–8004.

[54] Vassili Vorotnikov, Giannis Mpourmpakis, and Dionisios G Vlachos. "DFT study of furfural conversion to furan, furfuryl alcohol, and 2-methylfuran on Pd (111)". *Acs Catalysis* 2.12 (2012), 2496–2504.

[55] Rajeev S Assary and Larry A Curtiss. "Comparison of sugar molecule decomposition through glucose and fructose: a high-level quantum chemical study". *Energy & Fuels* 26.2 (2012), 1344–1352.

[56] Jianmin Lu, Sina Behtash, and Andreas Heyden. "Theoretical investigation of the reaction mechanism of the decarboxylation and decarbonylation of propanoic acid on Pd (111) model surfaces". *The Journal of Physical Chemistry C* 116.27 (2012), 14328–14341.

[57] Bin Liu and Jeffrey Greeley. "A density functional theory analysis of trends in glycerol decomposition on close-packed transition metal surfaces". *Physical Chemistry Chemical Physics* 15.17 (2013), 6475.

[58] Jianmin Lu, Sina Behtash, Osman Mamun, and Andreas Heyden. "Theoretical investigation of the reaction mechanism of the guaiacol hydrogenation over a Pt (111) catalyst". *ACS Catalysis* 5.4 (2015), 2423–2435.

[59] Yasuharu Okamoto, Osamu Sugino, Yuji Mochizuki, Tamio Ikeshoji, and Yoshitada Morikawa. "Comparative study of dehydrogenation of methanol at Pt(111)/water and Pt(111)/vacuum interfaces". *Chemical Physics Letters* 377.1-2 (2003), 236–242.

[60] C. Hartnig and E. Spohr. "The role of water in the initial steps of methanol oxidation on Pt(111)". *Chemical Physics* 319.1-3 (2005), 185–191.

[61] C. Hartnig, J. Grimminger, and E. Spohr. "Adsorption of formic acid on Pt(111) in the presence of water". *Journal of Electroanalytical Chemistry* 607.1-2 (2007), 133–139.

[62] C. Hartnig, J. Grimminger, and E. Spohr. "The role of water in the initial steps of methanol oxidation on Pt(2 1 1)". *Electrochimica Acta* 52.6 (2007), 2236–2243.

[63] Juan A. Santana, Carlos R. Cabrera, and Yasuyuki Ishikawa. "A density-functional theory study of electrochemical adsorption of sulfuric acid anions on Pt(111)". *Physical Chemistry Chemical Physics* 12.32 (2010), 9526.

[64] Nongnuch Artrith and Alexie M. Kolpak. "Understanding the Composition and Activity of Electrocatalytic Nanoalloys in Aqueous Solvents: A Combination of DFT and Accurate Neural Network Potentials". *Nano Letters* 14.5 (2014), 2670–2676.

[65] Ryosuke Jinnouchi, Kensaku Kodama, and Yu Morimoto. "DFT calculations on H, OH and O adsorbate formations on Pt(111) and Pt(332) electrodes". *Journal of Electroanalytical Chemistry* 716 (2014), 31–44.

[66] Jialong Liu, Xiao-Ming Cao, and P. Hu. "Density functional theory study on the activation of molecular oxygen on a stepped gold surface in an aqueous environment: a new approach for simulating reactions in solution". *Physical Chemistry Chemical Physics* 16.9 (2014), 4176.

[67] J. K. Nørskov, J. Rossmeisl, A. Logadottir, L. Lindqvist, J. R. Kitchin, T. Bligaard, and H. Jónsson. "Origin of the Overpotential for Oxygen Reduction at a Fuel-Cell Cathode". *The Journal of Physical Chemistry B* 108.46 (2004), 17886–17892.

[68] Sina Behtash, Jianmin Lu, Muhammad Faheem, and Andreas Heyden. "Solvent effects on the hydrodeoxygenation of propanoic acid over Pd(111) model surfaces". *Green Chem.* 16.2 (2014), 605–616.

[69] Sina Behtash, Jianmin Lu, Muhammad Faheem, and Andreas Heyden. "Solvent effects on the hydrodeoxygenation of propanoic acid over Pd(111) model surfaces". *Green Chem.* 16.2 (2014), 605–616.

[70] Sina Behtash, Jianmin Lu, and Andreas Heyden. "Theoretical investigation of the hydrodeoxygenation of methyl propionate over Pd (111) model surfaces". *Catal. Sci. Technol.* 4.11 (2014), 3981–3992.

[71] Mohammad Saleheen and Andreas Heyden. "Liquid-Phase Modeling in Heterogeneous Catalysis". *ACS Catalysis* 8 (2018), 2188–2194.

[72] Xiaowa Nie, Wenjia Luo, Michael J. Janik, and Aravind Asthagiri. "Reaction mechanisms of CO2 electrochemical reduction on Cu(111) determined with density functional theory". *Journal of Catalysis* 312 (2014), 108–122.

[73] Yoshihiro Gohda, Sebastian Schnur, and Axel Groß. "Influence of water on elementary reaction steps in electrocatalysis". *Faraday Discuss.* 140 (2009), 233–244.

[74] Anna Pavlova and Evert Jan Meijer. "Understanding the Role of Water in Aqueous Ruthenium-Catalyzed Transfer Hydrogenation of Ketones." *ChemPhysChem* 13.15 (2012), 3492–3496.

[75] Carine Michel, Florian Auneau, Françoise Delbecq, and Philippe Sautet. "C–H versus O–H Bond Dissociation for Alcohols on a Rh(111) Surface: A Strong Assistance from Hydrogen Bonded Neighbors". *ACS Catalysis* 1.10 (2011), 1430–1440.

[76] Carine Michel, Jérémie Zaffran, Agnieszka M. Ruppert, Joanna Matras-Michalska, Marcin Jędrzejczyk, Jacek Grams, and Philippe Sautet. "Role of water in metal catalyst performance for ketone hydrogenation: a joint experimental and theoretical study on levulinic acid conversion into gamma-valerolactone". *Chem. Commun.* 50.83 (2014), 12450–12453.

[77] J. Saavedra, H. A. Doan, C. J. Pursell, L. C. Grabow, and B. D. Chandler. "The critical role of water at the gold-titania interface in catalytic CO oxidation". *Science* 345.6204 (Apr. 2014), 1599–1602.

[78] Cameron J Bodenschatz, Sapna Sarupria, and Rachel B Getman. "Molecular-Level Details about Liquid H2O Interactions with CO and Sugar Alcohol Adsorbates on Pt (111) Calculated Using Density Functional Theory and Molecular Dynamics". *The Journal of Physical Chemistry C* 119.24 (2015), 13642–13651.

[79] Cameron J Bodenschatz, Xiaohong Zhang, Tianjun Xie, Jeremy Arvay, Sapna Sarupria, and Rachel B Getman. "Multiscale sampling of a heterogeneous water/metal catalyst interface using density functional theory and force-field molecular dynamics". *JoVE (Journal of Visualized Experiments)* 146 (2019), e59284.

[80] Nianjun Luo, Xianwen Fu, Fahai Cao, Tiancun Xiao, and Peter P Edwards. "Glycerol aqueous phase reforming for hydrogen generation over Pt catalyst–Effect of catalyst composition and reaction conditions". *Fuel* 87.17 (2008), 3483–3489.

Chapter 2

Multi-scale Simulation Strategy and Its Application

One key rationale behind multi-scale modeling is the notion of bridging different length scales in different systems. In other words, different length scales set different boundary conditions that can play an important role in material and process design, etc. However, different research disciplines (materials science, applied mechanics, atmospheric sciences, etc.) tend to focus on the research at each pertinent length scale whereas bridging multiple length scales presents a non-straightforward challenge. As the modern computational work requires more and more cross-discipline efforts, there is a rising need in academia and industry for multi-scale modeling as cost savings and accuracy in research and product design are rationalized. A wide variety of tools have been developed at each length scale level [1], that all share some common goals, which are to reduce costly large systems scale experiments, increase product quality and performance by providing more accurate predictions [2–4], and alleviate costly trial-and error iterations [5, 6]. In this thesis, a multi-scale method is applied in an effort to observe and investigate APR reactions at atomistic and molecular levels, in an effort to combine the strengths of atomistic and molecular simulations, thus bridging the gap of spatial scales between atomistic and molecular simulations. With our developed methods, we are able to explore reaction intermediates and reaction steps in the APR reaction network. Thermodynamic and kinetic results such as, binding energies, reaction energies, and activation energies are obtained using our multi-scale simulation methods. By investigating these quantitative energies, one can gain knowledge

of the dominant reaction pathways, crucial elementary steps, and stable chemical intermediates. All the effort can contribute to a better mechanistic understanding of the APR reactions of interest, and ultimately to the design of the next generation catalyst. Details of the multi-scale modeling strategy will be discussed in the following section.

2.1 Multi-scale Modeling Method

Multi-scale modeling techniques are powerful tools that empower researchers with the ability to garner their data in different time/length scales, which can be further used for optimization and development for robust ways to fine tune the computational accuracy and efficiency. Our work also requires such balance in the computational accuracy and efficiency. In general, since catalysis involves the breaking and forming of chemical bonds, quantum mechanics must be used to at least some degree; however, long simulations are challenging in quantum mechanics, as they require significant computer resources. In fact, the cost of quantum mechanical (QM) simulation scales as $O(N^3)$ or even more [7–9]. (It is to be noted here the scale factor N is not equal to the number of total atoms but instead it often scales to the total number of basis functions which is a significant number if heavy atoms are in presence). Since molecules in the liquid phase are under constant thermal motion, simulations must also include configurational sampling, i.e., they must incorporate multiple spatial arrangements of the liquid molecules, as each different spatial arrangement has a different energy. This means that multiple configurations of liquid molecules must be simulated for each catalytic species of interest. The need to use quantum mechanics and to perform multiple calculations per catalytic species can render modeling in heterogeneous catalysis under liquid phase computationally intractable. Force field based molecular dynamics (MD) simulations can be performed to reduce the time in system equilibration and sampling. MD is thus a good choice that allows to reduce the dependencies on computationally intensive DFT simulations while capturing bulk properties and ensemble averages of energies. The cost of employing MD simulations is much lower than for QM calculations, with the most straightforward cases scaling as $O(N^2)$, where N is the total number of atoms in the system. The cost is associated mainly due to electrostatic interactions term (pairwise interactions with any other atoms in the system). Since use of both DFT and MD calculations on our calculations involves complicated reaction systems and large reaction networks, it is impractical to study each catalytic species in great detail. Instead, our goal is to explore the aqueous phase

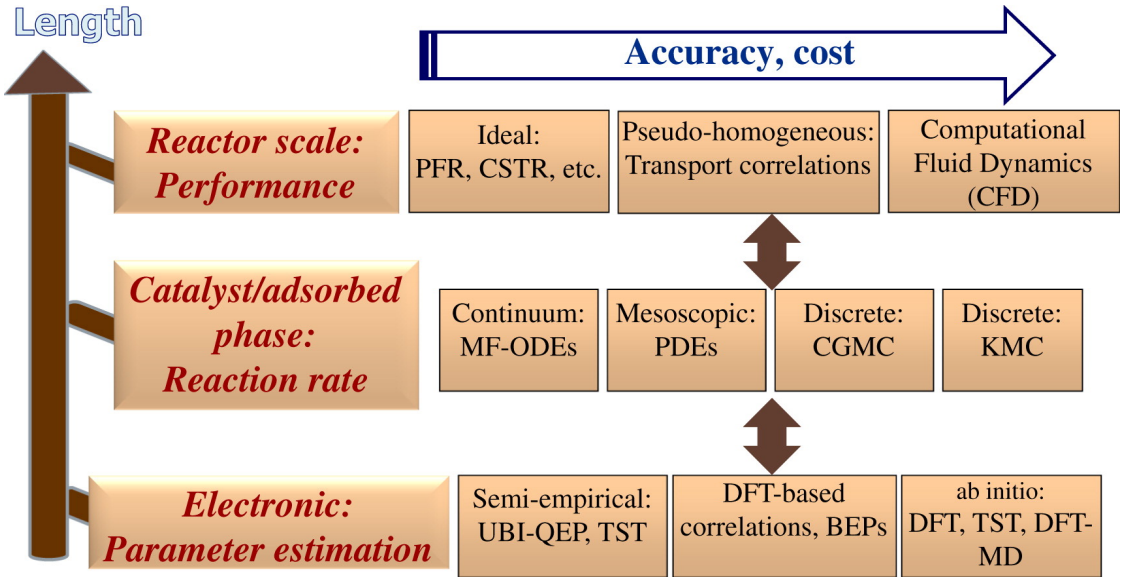

Figure 2.1: Schematic of three scales and a possible hierarchy of models at each scale. Acronyms from top to bottom: PRF, plug flow reactor; CSTR, continuously stirred tank reactor; ODE, ordinary differential equation; PDE, partial differential equation; CG-KMC, coarse-grained kinetic Monte Carlo; KMC, kinetic Monte Carlo; UBI-QEP, unity bond index-quadratic exponential potential; TST, transition state theory; DFT, density functional theory; GA, group additivity; BEP, Brønsted-Evans-Polanyi; QM/MM, quantum mechanics/molecular mechanics. Adapted from [10] with permission from Elsevier.

catalytic phenomena, which can be ahchieved by using a hybrid technique, to operate calculations at a level between MD and DFT methods (Fig. 2.1 [10]). Doing so will combine the accuracy of DFT methods with the efficiency of MD methods. In this work, we develop multi-scale simulation techniques that combine DFT/MD methods as well as linear scaling relations (LSRs) to investigate APR reactions. The LSR maintains near DFT accuracy while significantly reducing computational expense [11, 12], making it possible to model the large reaction networks associated with conversions of biomass waste streams. In these approaches, DFT is mainly used to the optimize geometries and calculate energies of catalytic species, while MD is used to equilibrate bulk water structures and provide ensembles of liquid configurations. LSRs are used to rapidly estimate thermodynamic and kinetic energies for a large number of catalytic species, allowing us to systematically study the glycerol aqueous phase reforming reaction network.

Water molecules have significant influence on catalytic phenomena, such as interacting with catalytic species (e.g., via dispersion forces and hydrogen bonding) [13–34], participating in catalytic reactions [13, 18–20, 27, 33, 35–39], and influencing reaction pathways and/or catalytic rates [13,

22, 23, 27, 31, 34, 37, 39–43]. Modeling of these phenomena has been performed using QM (Fig. 2.2 provides a flowchart showing how a DFT simulation is conducted) and/or ab initio molecular dynamics (AIMD) [13, 14, 18, 24, 26, 33, 37, 39, 40, 44, 45], force field based molecular dynamics (MD) [46], and quantum mechanics/molecular mechanics (QM/MM) [21]. In AIMD and MD, the atoms in the system are moved pursuant to Newton's equations of motion according to the forces acting upon them. In AIMD, the system energy and forces are calculated with QM, whereas in MD, the system energy and forces are calculated using force fields, which are algebraic expressions that are parameterized based on experimental or QM data. (Fig. 2.3 provides a flowchart showing how a MD simulation is conducted.)

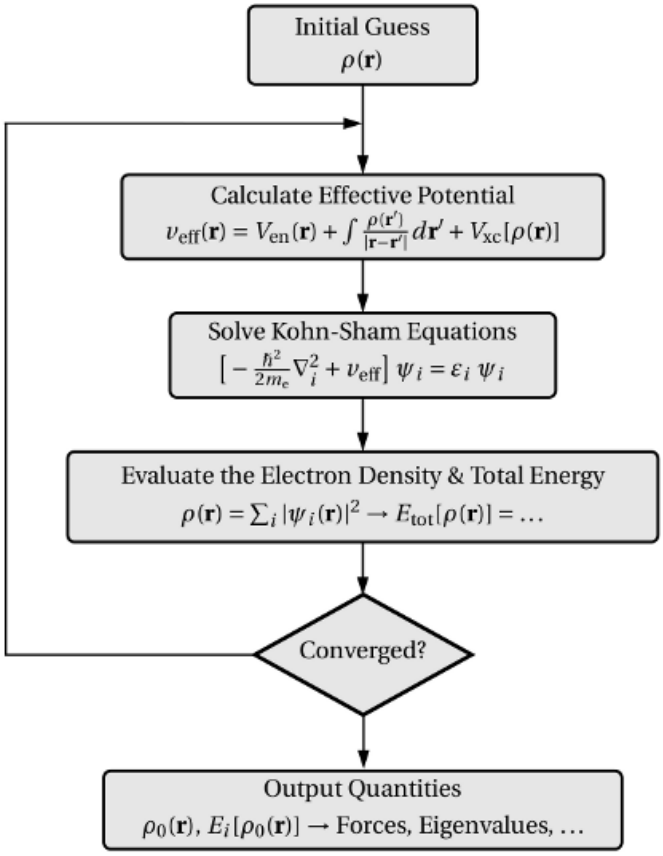

Figure 2.2: Typical work flow of a DFT simulation [47].

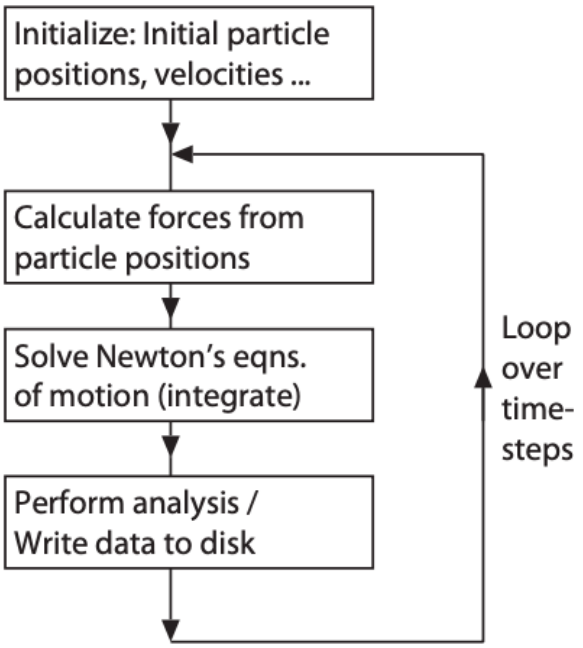

Figure 2.3: Typical work flow of a force field molecular dynamics simulation.

2.2 Using Linear Correlations to Reduce Computational Expense

2.2.1 Using Linear Scaling Relationships to Estimate Reaction Energies

A key step in the DFT method is the relaxation of the reaction intermediate, which is often done under vacuum. It has been shown previously that the energies of 'large' surface adsorbates (e.g. glycerol) in vacuum can be approximated with reasonable accuracy using LSRs [48–55], eliminating the need to explicitly calculate their energies in DFT. We use an LSR in our developed method [11], which we call LSR/ MD. In this method, an extended LSR is used to compute the vacuum-phase binding energies of glycerol dehydrogenation intermediates. Normally, the LSR is able to compute the binding energies of C, H and O containing adsorbates as linear combinations of the binding energies of the central atoms (here, C and O). In this work, the LSR is extended into a function of groups of atoms, in contrast with traditionally of central binding atoms. For instance, the fragment

of the carbon backbone of dehydrogenated glycerol can be CH_2OH, CHOH, COH, CH_2O, CHO and CO, i.e.

$$E^{\text{vac}}_{\text{bind}}(\text{CH}_{y'}\text{O—CH}_{y''}\text{O—CH}_{y'''}\text{O}) = \gamma(E(\text{CH}_{y'}\text{O}) + E(\text{CH}_{y''}\text{O}) + E(\text{CH}_{y'''}\text{O})) + \xi \tag{2.1}$$

where y is the total number of hydrogen atoms in the reaction intermediate, which has stoichiometry $C_3H_yO_3$; y', y" and y"' are the numbers of hydrogen atoms that are bound to the different groups (y' + y" + y"' =y); and γ and ξ are the slope and intercept of the fitting, which are obtained via linear regression.

2.2.2 Using Transition State Scaling Relationships to Estimate Activation Energies

We established transition state scaling (TSS) relationships [56–63] to estimate the energies of transition states involved in dehydrogenation and decarbonylation reactions involving C3 catalytic intermediates. We additionally construct TSS relationships for hydrogenolysis reactions (R-OH* + * $\rightarrow$ R* + OH*) involving C3 species. To investigate the ability of H_2O to participate in the catalysis, we additionally simulate water-mediated dehydrogenation (R-H* + $n$$H_2O$* $\rightarrow$ R* + $H_{(2n+1)}O_n$*) and hydrogenolysis steps (R-OH* + $H_{(2n+1)}O_n$* $\rightarrow$ R* + $(n+1)H_2O$*).

Without TSS, activation energies would have to be explicitly calculated with DFT. For example, the activation energy for an aqueous phase reaction, $E^{\text{aq}}_{\text{act}}$ is calculated as

$$E^{\text{aq}}_{\text{act}} = E(\text{TS*}) - E(\text{IS*}) \tag{2.2}$$

where IS stands for initial state and in this work is the reactant species. E(TS*) is the electronic energy of the transition state, which is calculated with DFT is often hard to obtain. With an existing TSS, it can be now estimated without needing to perform DFT by

$$E(\text{TS}) = aE(\text{FS}) + b \tag{2.3}$$

where a and b are linear fitting parameters. That is, with a TSS, the transition state energy can be known as long as the final state (FS) energy, i.e., the energy of the products, is known. This

greatly reduces the computational expense needed to calculate activation energies, since the cost of calculating local minima on the potential energy surface is significantly smaller than for transition states. More discussions and specifications of TSS method we used are presented in Chapter 4.

2.3 MD/DFT Multi-scale Modeling Strategy

In order to emulate the experimental settings and further to ensure the search of important reaction steps and reaction intermediates that correspond to the reaction conditions of interest, we reported a protocol involving a multi-scale modeling strategy that combines MD and DFT to interrogate system properties under realistic reaction conditions. More specifically, the temperature (T) and pressure (P), and the bulk density of the water (ρ) at the MD stage of the multi-scale strategy, are determined using a sequence of statistical mechanics ensembles NVE, NPT and NVT simulations. The role of the first NVE run is to optimize the system structure, to allow the system to reach a 'good' pre-equilibrium state to start NPT simulations. The second run, NPT, regulates the pressure so that the water stays within liquid phase. The last run, NVT conserves the volume of the system, and it is used to yield desired liquid water configurations for more detailed examination in DFT. These three types of MD simulations are used in a sequence in order to determine the appropriate cell volume/size for both DFT and MD calculations.

In our published work, we present a 6-step work flow that can determine the simulation cell dimension that is reliable and requires minimal human intervention. This thesis demonstrates the use of the protocol for generating configurations of liquid H_2O that can be used to calculate quantities of interest in aqueous phase heterogeneous catalysis [64]. A brief scheme of determination of the simulation cell is as following,

1. Generate the adsorbate structure
2. Add explicit H_2O molecules
3. Determine the proper height of the supercell (i.e., the density at the simulation temperature)
4. Generate configurations of H_2O molecules using MD
5. Determine the hydrogen bond lifetime for proper time sampling
6. Sample configurations of liquid H_2O molecules

7. Use the configurations in DFT (or AIMD, QM/MM, etc.)

2.4 Pt (1 1 1) Catalyst System

As a common approach to represent the active catalyst component Pt, simulations in Chapters 3 and 4 of this dissertation utilize catalyst surfaces that are modeled as single crystal Pt (1 1 1), created from an optimized bulk structure of pure Pt slab, yielding a DFT calculated lattice constant of 3.967Å (compared experimental value of 3.924Å [65]). Pt(1 1 1) was created by cleaving to expose the (1 1 1) facet, as the active terrace sites for aqueous phase heterogeneous catalysis study. In the following work, 3-layer monoclinic 3×3 Pt (1 1 1) and 3-layer orthogonal 4×4 Pt (1 1 1) catalyst surfaces are used (see Figure 3.1 and Figure 4.1). Note this is a well-established and widely-used model for Pt based catalyst systems. More advanced models based on this model that take into other factors that could also be influential, for example, the catalyst supports and their effects on the surface chemistry, are discussed in Chapter 5.

Surface species can bind to the Pt (1 1 1) catalyst via various high symmetry sites on the Pt (1 1 1) terraces, including atop site, bridge site, FCC site and HCP site, as shown in Figure 2.4. Unless otherwise specified, all chemical species in this dissertation were isolated in individual simulation boxes, and the surface coverages for all adsorbed surface species were modeled at constant values, i.e. 1/9 or 1/16 monolayer (a monolayer, ML, is defined as a single, closely packed layer of atoms, where the number of adsorbates per surface metal atom is equal to one – accordingly, the catalyst systems employed in this work consist of 9 Pt atoms and 16 Pt atoms within the x-y plane). This means that all the dissociated atoms/fragments were removed from the original cell.

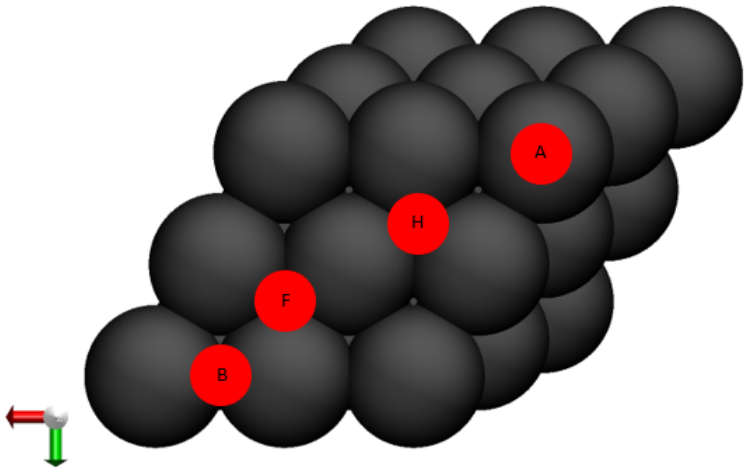

Figure 2.4: Binding sites across the Pt(1 1 1) surface (unit cell). The large dark grey particles denote Pt atoms on the surface. The small red circles denote the binding positions of the sites. The letters H, F, A and B denote the HCP, FCC, Atop and bridge sites, respectively.

2.5 Density Functional Theory and Force Field Molecular Dynamics Calculations

In this section, quantum calculations based on DFT are discussed. Commercial software, The Vienna Ab initio Simulation Package (VASP) [66–69], which is a plane wave based computational package, is used for atomic scale materials modelling, e.g. electronic structure calculations, from first principles. Descriptions of DFT calculations will be divided into three subsections, based on the functionality of DFT calculations: geometry optimization, single point energy calculation, transition state searches using climbing image-nudged elastic band method (CI-NEB) [70, 71] and dimer method calculations [72]. An introduction of MD method and specifications are included in this section.

2.5.1 DFT Simulation Setup

Projector augmented wave (PAW) [73, 74] pseudopotentials were used to model the core electrons to an energy cutoff of 400 eV. Exchange and correlation of the valence electrons were captured with the Perdew-Burke-Ernzerhof (PBE) [75] form of the generalized gradient approximation

(GGA). Gaussian smearing with a smearing factor of 0.1 eV was employed. The D2 dispersion correction method developed by Grimme et al. [76] was applied to improve the description of long range dispersion interactions by PBE functional. The choice of dispersion correction has been shown to influence the energies of adsorption on metal surfaces [77–79]. In our most recent work in Chapter 5, dispersion correction is done by the more advanced D3 method with Becke-Jonson (BJ) damping implemented [80, 81], which addresses the divergence of the repulsive potential in close distances. Automatically generated Monkhorst-Pack [82] Γ-centered $7 \times 7 \times 1$ k-point meshes were applied to sample the first Brillouin zones. Electronic structure calculations were performed iteratively, and electronic structures were considered to be converged when the energy difference between subsequent iterations fell below 10^{-6} eV. Geometries of catalytic species were located using quasi-Newton based geometry relaxation [83] and were considered to be converged when the maximum force on all non-fixed atoms fell below 0.03 eV/Å. The computational time for such procedure to finish varies from hours to weeks depending on the initial structure, type of the simulations, the system dimensions and the computational hardware.

2.5.1.1 Single Point Energy Calculation

This procedure differs from regular DFT geometry optimization procedures that a single point energy calculation calculates the energy, wave function and other requested properties at a single fixed geometry. It can be done first at the beginning of a study on a new molecule to check out the nature of its wave function and electronic energy of the system at a low expense, prior to a full DFT geometry optimization which would require a lot more computational expense and would suffer if the initial setting are incorrect. It is also frequently carried out after a geometry optimization, or for a geometry that is prohibitively large to carry out a regular geometry optimization procedure.

2.5.1.2 Climbing Image-nudged Elastic Band Calculation

The Nudged Elastic Band (NEB) method is a technique for finding transition paths (and corresponding barriers along the energy paths) between given initial and final states [70, 84, 85]. The method involves constructing a "band" of images the system and relaxing those states by adding spring forces along the band by projecting out the component of the force due to the potential perpendicular to the band . Normally there are images created between known reactants and products through linear interpolation. This method then optimizes these intermediate images along the re-

action path. After convergence, each image will find the lowest energy possible while maintaining equal-spacing to their adjacent images.

The Climbing Image-nudged Elastic Band (CI-NEB) method was firstly developed by Henkelman et al. [71], improved based upon the original NEB method. In the CI-NEB method, the highest energy image is driven up to a single saddle point. By implementing this, the middle image does not experience the spring forces along the band. Instead, the true force along the tangent is the inverted force. In this way, the image will land on its maximized energy along the band, and minimize in all other directions, i.e. near or at the saddle point. After convergence, vibrational frequencies simulations can be conducted using DFT, to confirm the only existing imaginary reaction vibrational mode is along the predicted reaction coordinate. With the confirmation from vibrational frequencies simulations and visualization, a transition state along with the activation barrier, which is illustrate as in Figure. 2.5.

In this work, we use the CI-NEB method. Electronic structure is converged after the energy difference between subsequent iterations fall below 10^{-6} eV. Force convergence is set to be when the maximum force on all non-fixed atoms fall below 0.5 eV/Å. We use the results to input into a dimer simulation, which refines the transition state geometry further.

2.5.1.3 Dimer Calculation

Another popular method in searching for transition states is called the dimer method [72]. It is complimentary to the CI-NEB or NEB method because it does not require the knowledge of the final state to generate the path from a reactant to a product. Instead, in order to locate the local minimum of a nearby potential energy surface, an initial guess is provided. The dimer method will evolve the configuration from the given guess structure and converge it to a saddle point. After convergence, vibrational frequencies simulations can be conducted using DFT, to confirm the only existing imaginary reaction vibrational mode is along the predicted reaction coordinate. With the confirmation from vibrational frequencies simulations and visualization, a transition state along with the activation barrier, illustrated as E_{A} in Fig. 2.5. Alternatively, dimer method is used to reveal unknown chemical reactions and search in random directions for saddle points. In some simple systems, reaction endpoints can be guessed, and the NEB can provide reasonable guidelines for reaction pathways.

In our work, the dimer method is used for searching of transition state species under

known/proposed reaction paths. Albeit its precision and reliability in transition state searching and activation energy calculations, dimer simulation can be very time consuming. Additional computational complexity comes from failed simulations and there is little prior information until the dimer simulation was deemed failed under manual inspections. In fact, simulations of dimer set up is still dependent on some human intuition, such as proposed reaction paths and simulation parameters. In attempt to tackle the computational expense problem on searching for transition states of chemical reactions, we developed an energy descriptor based approach based on transition state scaling (TSS). The details of the background, implementation, and results of TSS will be covered in Chapter 4.

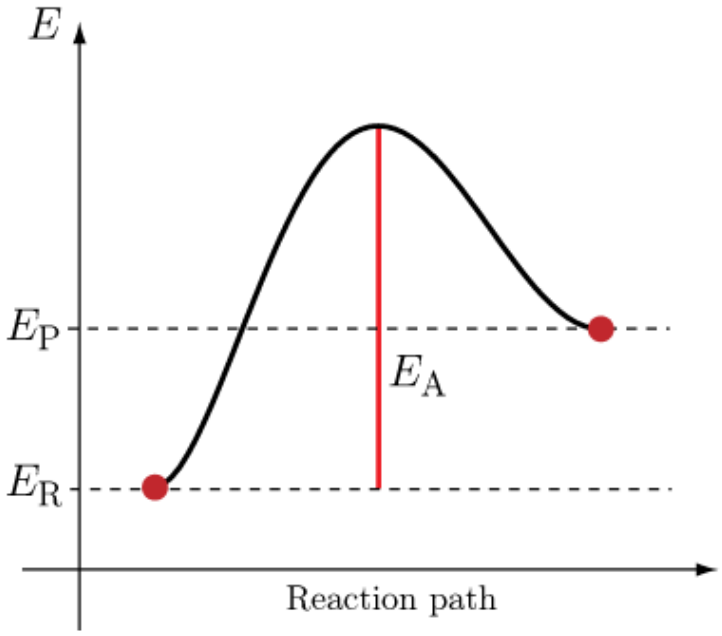

Figure 2.5: Plot for energy variation between the reactant and product for a reaction. In order for the reactant to be activated, an energy barrier (red vertical line), so-called activation energy E_A must be overcome.

2.5.2 Force Field Based Molecular Dynamics Simulations

MD simulations are performed with the Large-scale Atomic/ Molecular Massively Parallel Simulator (LAMMPS) [86] in the NVT ensemble. The target temperature is set at 500 K with the Nose–Hoover thermostat [87]. This temperature is chosen to replicate the experimental conditions of

aqueous-phase reforming of oxygenated hydrocarbons [27, 88–90]. MD simulations are performed for 5 ns (5×10^{-9} s) with 1 fs (10^{-15} s) time steps, where the first 2 ns are used for system equilibration and the remaining 3 ns are used for the production runs. Atomic quantities and thermodynamic information are reported every 100 fs. Non-bonded water–water, water–adsorbate and water–Pt interactions are calculated with Lennard-Jones + Coulomb (LJ + C) potentials, with LJ parameters and partial electronic charges (Coulomb parameters) for adsorbates, H_2O and Pt taken from the optimized potentials for liquid simulations (OPLS) [91], TIP3P [92] and INTERFACE force fields [93], respectively. Cross-terms for the LJ interactions are computed using Lorentz-Berthelot mixing rules [94, 95]. A total of 36 H_2O molecules are present in the simulation boxes. Note the system size was limited in order to allow feasible DFT energy calculations. The x-y plane of the simulation box is set to equal to the dimensions of chosen catalyst model. The vertical dimension is determined using the sequence of the NVE, NPT and NVE workflow, as previously presented in this chapter. During MD simulations, these H_2O molecules provide an explicit solvation environment as they form a liquid film $\sim$ 20 Å, which is stabilized near the surface region. Similar liquid water films were observed at 500 K using TIP3P water in MD by Ismail et al. [96] and Longhi et al. [97].

2.6 Reference

[1] Sidney Yip. *Handbook of materials modeling*. Springer Science & Business Media, 2007.

[2] Dimitrios Maroudas. "Multiscale modeling of hard materials: Challenges and opportunities for chemical engineering". *AIChE Journal* 46.5 (2000), 878–882.

[3] Paul Sherwood, Bernard R Brooks, and Mark SP Sansom. "Multiscale methods for macromolecular simulations". *Current opinion in structural biology* 18.5 (2008), 630–640.

[4] Z Xia, WA Curtin, and PWM Peters. "Multiscale modeling of failure in metal matrix composites". *Acta Materialia* 49.2 (2001), 273–287.

[5] Paul T Bauman, J Tinsley Oden, and Serge Prudhomme. "Adaptive multiscale modeling of polymeric materials with Arlequin coupling and Goals algorithms". *Computer methods in applied mechanics and engineering* 198.5-8 (2009), 799–818.

[6] Mark F Horstemeyer. "Multiscale modeling: a review". *Practical aspects of computational chemistry*. Springer, 2009, 87–135.

[7] Rick A Kendall and Herbert A Früchtl. "The impact of the resolution of the identity approximate integral method on modern ab initio algorithm development". *Theoretical Chemistry Accounts* 97.1-4 (1997), 158–163.

[8] DR Bowler, R Choudhury, MJ Gillan, and T Miyazaki. "Recent progress with large-scale ab initio calculations: the CONQUEST code". *physica status solidi (b)* 243.5 (2006), 989–1000.

[9] Satoshi Yokojima and GuanHua Chen. "Linear scaling calculation of excited-state properties of polyacetylene". *Physical Review B* 59.11 (1999), 7259.

[10] Michael Salciccioli, Michail Stamatakis, S Caratzoulas, and Dion G Vlachos. "A review of multiscale modeling of metal-catalyzed reactions: Mechanism development for complexity and emergent behavior". *Chemical Engineering Science* 66.19 (2011), 4319–4355.

[11] Tianjun Xie, Sapna Sarupria, and Rachel B Getman. "A DFT and MD study of aqueous-phase dehydrogenation of glycerol on Pt (1 1 1): comparing chemical accuracy versus computational expense in different methods for calculating aqueous-phase system energies". *Molecular Simulation* 43.5-6 (2017), 370–378.

[12] Tianjun Xie, Cameron J Bodenschatz, and Rachel B Getman. "Insights into the roles of water on the aqueous phase reforming of glycerol". *Reaction Chemistry & Engineering* 4.2 (2019), 383–392.

[13] Jialong Liu, Xiao-Ming Cao, and P Hu. "Density functional theory study on the activation of molecular oxygen on a stepped gold surface in an aqueous environment: a new approach for simulating reactions in solution". *Physical Chemistry Chemical Physics* 16.9 (2014), 4176–4185.

[14] Yasuharu Okamoto, Osamu Sugino, Yuji Mochizuki, Tamio Ikeshoji, and Yoshitada Morikawa. "Comparative study of dehydrogenation of methanol at Pt (1 1 1)/water and Pt (1 1 1)/vacuum interfaces". *Chemical physics letters* 377.1-2 (2003), 236–242.

[15] Juan A Santana, Carlos R Cabrera, and Yasuyuki Ishikawa. "A density-functional theory study of electrochemical adsorption of sulfuric acid anions on Pt (111)". *Physical Chemistry Chemical Physics* 12.32 (2010), 9526–9534.

[16] Nongnuch Artrith and Alexie M Kolpak. "Understanding the composition and activity of electrocatalytic nanoalloys in aqueous solvents: A combination of DFT and accurate neural network potentials". *Nano letters* 14.5 (2014), 2670–2676.

[17] Ryosuke Jinnouchi, Kensaku Kodama, and Yu Morimoto. "DFT calculations on H, OH and O adsorbate formations on Pt (111) and Pt (332) electrodes". *Journal of Electroanalytical Chemistry* 716 (2014), 31–44.

[18] Sanket K Desai, Venkataraman Pallassana, and Matthew Neurock. "A periodic density functional theory analysis of the effect of water molecules on deprotonation of acetic acid over Pd (111)". *The Journal of Physical Chemistry B* 105.38 (2001), 9171–9182.

[19] Zheng-Qing Huang, Bo Long, and Chun-Ran Chang. "A theoretical study on the catalytic role of water in methanol steam reforming on PdZn (111)". *Catalysis Science & Technology* 5.5 (2015), 2935–2944.

[20] Chun-Ran Chang, Zheng-Qing Huang, and Jun Li. "Hydrogenation of molecular oxygen to hydroperoxyl: An alternative pathway for O 2 activation on nanogold catalysts". *Nano Research* 8.11 (2015), 3737–3748.

[21] Muhammad Faheem and Andreas Heyden. "Hybrid quantum mechanics/molecular mechanics solvation scheme for computing free energies of reactions at metal-water interfaces". *Journal of chemical theory and computation* 10.8 (2014), 3354–3368.

[22] Sina Behtash, Jianmin Lu, Osman Mamun, Christopher T Williams, John R Monnier, and Andreas Heyden. "Solvation effects in the hydrodeoxygenation of propanoic acid over a model Pd (211) catalyst". *The Journal of Physical Chemistry C* 120.5 (2016), 2724–2736.

[23] Sina Behtash, Jianmin Lu, Eric Walker, Osman Mamun, and Andreas Heyden. "Solvent effects in the liquid phase hydrodeoxygenation of methyl propionate over a Pd (1 1 1) catalyst model". *Journal of catalysis* 333 (2016), 171–183.

[24] Yeohoon Yoon, Roger Rousseau, Robert S Weber, Donghai Mei, and Johannes A Lercher. "First-principles study of phenol hydrogenation on Pt and Ni catalysts in aqueous phase". *Journal of the American Chemical Society* 136.29 (2014), 10287–10298.

[25] Jens Kehlet Nørskov, Jan Rossmeisl, Ashildur Logadottir, LRKJ Lindqvist, John R Kitchin, Thomas Bligaard, and Hannes Jonsson. "Origin of the overpotential for oxygen reduction at a fuel-cell cathode". *The Journal of Physical Chemistry B* 108.46 (2004), 17886–17892.

[26] Dmitry Skachkov, Chitturi Venkateswara Rao, and Yasuyuki Ishikawa. "Combined first-principles molecular dynamics/density functional theory study of ammonia electrooxidation on Pt (100) electrode". *The Journal of Physical Chemistry C* 117.48 (2013), 25451–25466.

[27] David D Hibbitts, Brett T Loveless, Matthew Neurock, and Enrique Iglesia. "Mechanistic role of water on the rate and selectivity of Fischer–Tropsch synthesis on ruthenium catalysts". *Angewandte Chemie International Edition* 52.47 (2013), 12273–12278.

[28] Omar Ali Abdelrahman, Andreas Heyden, and Jesse Q Bond. "Analysis of kinetics and reaction pathways in the aqueous-phase hydrogenation of levulinic acid to form gamma -valerolactone over Ru/C". *ACS catalysis* 4.4 (2014), 1171–1181.

[29] Hui-Fang Wang and Zhi-Pan Liu. "Formic acid oxidation at Pt/H2O interface from periodic DFT calculations integrated with a continuum solvation model". *The Journal of Physical Chemistry C* 113.40 (2009), 17502–17508.

[30] Sina Behtash, Jianmin Lu, Muhammad Faheem, and Andreas Heyden. "Solvent effects on the hydrodeoxygenation of propanoic acid over Pd (111) model surfaces". *Green Chemistry* 16.2 (2014), 605–616.

[31] Sina Behtash, Jianmin Lu, Muhammad Faheem, and Andreas Heyden. "Solvent effects on the hydrodeoxygenation of propanoic acid over Pd(111) model surfaces". *Green Chem.* 16.2 (2014), 605–616.

[32] Matthew M Montemore, Oliviero Andreussi, and J Will Medlin. "Hydrocarbon adsorption in an aqueous environment: A computational study of alkyls on Cu (111)". *The Journal of chemical physics* 145.7 (2016), 074702.

[33] C. Hartnig and E. Spohr. "The role of water in the initial steps of methanol oxidation on Pt(111)". *Chemical Physics* 319.1-3 (2005), 185–191.

[34] Carine Michel, Jérémie Zaffran, Agnieszka M Ruppert, Joanna Matras-Michalska, Marcin Jędrzejczyk, Jacek Grams, and Philippe Sautet. "Role of water in metal catalyst performance for

ketone hydrogenation: a joint experimental and theoretical study on levulinic acid conversion into gamma-valerolactone". *Chemical Communications* 50.83 (2014), 12450–12453.

[35] C. Hartnig, J. Grimminger, and E. Spohr. "The role of water in the initial steps of methanol oxidation on Pt(2 1 1)". *Electrochimica Acta* 52.6 (2007), 2236–2243.

[36] Bhushan N Zope, David D Hibbitts, Matthew Neurock, and Robert J Davis. "Reactivity of the gold/water interface during selective oxidation catalysis". *Science* 330.6000 (2010), 74–78.

[37] Anna Pavlova and Evert Jan Meijer. "Understanding the Role of Water in Aqueous Ruthenium-Catalyzed Transfer Hydrogenation of Ketones." *ChemPhysChem* 13.15 (2012), 3492–3496.

[38] J. Saavedra, H. A. Doan, C. J. Pursell, L. C. Grabow, and B. D. Chandler. "The critical role of water at the gold-titania interface in catalytic CO oxidation". *Science* 345.6204 (Apr. 2014), 1599–1602.

[39] Sanket Desai and Matthew Neurock. "A first principles analysis of CO oxidation over Pt and Pt66. 7% Ru33. 3%(111) surfaces". *Electrochimica Acta* 48.25-26 (2003), 3759–3773.

[40] Yoshihiro Gohda, Sebastian Schnur, and Axel Groß. "Influence of water on elementary reaction steps in electrocatalysis". *Faraday Discuss.* 140 (2009), 233–244.

[41] Xiaowa Nie, Wenjia Luo, Michael J. Janik, and Aravind Asthagiri. "Reaction mechanisms of CO2 electrochemical reduction on Cu(111) determined with density functional theory". *Journal of Catalysis* 312 (2014), 108–122.

[42] Carine Michel, Florian Auneau, Françoise Delbecq, and Philippe Sautet. "C–H versus O–H Bond Dissociation for Alcohols on a Rh (111) Surface: A Strong Assistance from Hydrogen Bonded Neighbors". *ACS catalysis* 1.10 (2011), 1430–1440.

[43] Matthew Neurock, Sally A Wasileski, and Donghai Mei. "From first principles to catalytic performance: tracking molecular transformations". *Chemical engineering science* 59.22-23 (2004), 4703–4714.

[44] Matteo Farnesi Camellone and Dominik Marx. "On the impact of solvation on a Au/TiO2 nanocatalyst in contact with water". *The journal of physical chemistry letters* 4.3 (2013), 514–518.

[45] Juan A Santana, Juan J Mateo, and Yasuyuki Ishikawa. "Electrochemical hydrogen oxidation on Pt (110): a combined direct molecular dynamics/density functional theory study". *The Journal of Physical Chemistry C* 114.11 (2010), 4995–5002.

[46] Cameron J Bodenschatz, Sapna Sarupria, and Rachel B Getman. "Molecular-Level Details about Liquid H2O Interactions with CO and Sugar Alcohol Adsorbates on Pt (111) Calculated Using Density Functional Theory and Molecular Dynamics". *The Journal of Physical Chemistry C* 119.24 (2015), 13642–13651.

[47] Wolfgang Gös. *Hole trapping and the negative bias temperature instability.* eingereicht an der Technischen Universität Wien, 2011.

[48] Jaime Gómez-Díaz and Núria López. "Mechanistic switch between oxidative (Andrussow) and nonoxidative (Degussa) formation of HCN on Pt (111) by density functional theory". *The journal of physical chemistry C* 115.13 (2011), 5667–5674.

[49] Omar Ali Abdelrahman, Andreas Heyden, and Jesse Q Bond. "Analysis of kinetics and reaction pathways in the aqueous-phase hydrogenation of levulinic acid to form γ-valerolactone over Ru/C". *ACS catalysis* 4.4 (2014), 1171–1181.

[50] Aravind Asthagiri and Michael J Janik. *Computational catalysis.* Royal Society of Chemistry, 2013.

[51] Lars C Grabow, Felix Studt, Frank Abild-Pedersen, Vivien Petzold, Jesper Kleis, Thomas Bligaard, and Jens K Nørskov. "Descriptor-based analysis applied to HCN synthesis from NH3 and CH4". *Angewandte Chemie International Edition* 50.20 (2011), 4601–4605.

[52] Frank Abild-Pedersen, Jeff Greeley, Felix Studt, Jan Rossmeisl, TR Munter, Poul Georg Moses, Egill Skulason, Thomas Bligaard, and Jens Kehlet Nørskov. "Scaling properties of adsorption energies for hydrogen-containing molecules on transition-metal surfaces". *Physical review letters* 99.1 (2007), 016105.

[53] Jeffrey Greeley. "Theoretical heterogeneous catalysis: scaling relationships and computational catalyst design". *Annual review of chemical and biomolecular engineering* 7 (2016), 605–635.

[54] Glenn Jones, T Bligaard, Frank Abild-Pedersen, and Jens Kehlet Nørskov. "Using scaling relations to understand trends in the catalytic activity of transition metals". *Journal of Physics: Condensed Matter* 20.6 (2008), 064239.

[55] Isabela C Man et al. "Universality in oxygen evolution electrocatalysis on oxide surfaces". *ChemCatChem* 3.7 (2011), 1159–1165.

[56] J.K. Nørskov et al. "Universality in Heterogeneous Catalysis". *Journal of Catalysis* 209.2 (2002), 275–278.

[57] P. Ferrin, D. Simonetti, S. Kandoi, E. Kunkes, J. A. Dumesic, J. K. Nørskov, and M. Mavrikakis. "Modeling Ethanol Decomposition on Transition Metals: A Combined Application of Scaling and Brønsted-Evans-Polanyi Relations". *Journal of the American Chemical Society* 131.16 (2009), 5809–5815.

[58] Bin Liu and Jeffrey Greeley. "Decomposition Pathways of Glycerol via C–H, O–H, and C–C Bond Scission on Pt(111): A Density Functional Theory Study". *The Journal of Physical Chemistry C* 115.40 (2011), 19702–19709.

[59] Bin Liu, Lei Cheng, Larry Curtiss, and Jeffrey Greeley. "Effects of van der Waals density functional corrections on trends in furfural adsorption and hydrogenation on close-packed transition metal surfaces". *Surface Science* 622 (2014), 51–59.

[60] Bin Liu, Mingxia Zhou, Maria K. Y. Chan, and Jeffrey P. Greeley. "Understanding Polyol Decomposition on Bimetallic Pt–Mo Catalysts—A DFT Study of Glycerol". *ACS Catalysis* 5.8 (2015), 4942–4950.

[61] Y. Chen, M. Salciccioli, and D. G. Vlachos. "An Efficient Reaction Pathway Search Method Applied to the Decomposition of Glycerol on Platinum". *The Journal of Physical Chemistry C* 115.38 (2011), 18707–18720.

[62] R Alcala. "DFT studies for cleavage of C-C bond and C-O bonds in surface species derived from ethanol on Pt(111)". *Journal of Catalysis* 218.1 (2003), 178–190.

[63] David Loffreda, Françoise Delbecq, Fabienne Vigné, and Philippe Sautet. "Fast Prediction of Selectivity in Heterogeneous Catalysis from Extended Brønsted-Evans-Polanyi Relations: A Theoretical Insight". *Angewandte Chemie* 121.47 (2009), 9140–9142.

[64] Cameron J Bodenschatz, Xiaohong Zhang, Tianjun Xie, Jeremy Arvay, Sapna Sarupria, and Rachel B Getman. "Multiscale sampling of a heterogeneous water/metal catalyst interface using density functional theory and force-field molecular dynamics". *JoVE (Journal of Visualized Experiments)* 146 (2019), e59284.

[65] David R Lide. *CRC handbook of chemistry and physics: a ready-reference book of chemical and physical data*. CRC press, 1995.

[66] Georg Kresse and Jürgen Hafner. "Ab initio molecular dynamics for liquid metals". *Physical Review B* 47.1 (1993), 558.

[67] Georg Kresse and Jürgen Furthmüller. "Efficient iterative schemes for ab initio total-energy calculations using a plane-wave basis set". *Physical review B* 54.16 (1996), 11169.

[68] Georg Kresse and Jürgen Furthmüller. "Efficiency of ab-initio total energy calculations for metals and semiconductors using a plane-wave basis set". *Computational materials science* 6.1 (1996), 15–50.

[69] Georg Kresse and D Joubert. "From ultrasoft pseudopotentials to the projector augmented-wave method". *Physical Review B* 59.3 (1999), 1758.

[70] Graeme Henkelman, Blas P Uberuaga, and Hannes Jónsson. "A climbing image nudged elastic band method for finding saddle points and minimum energy paths". *The Journal of chemical physics* 113.22 (2000), 9901–9904.

[71] Graeme Henkelman and Hannes Jónsson. "Improved tangent estimate in the nudged elastic band method for finding minimum energy paths and saddle points". *The Journal of chemical physics* 113.22 (2000), 9978–9985.

[72] Graeme Henkelman and Hannes Jónsson. "A dimer method for finding saddle points on high dimensional potential surfaces using only first derivatives". *The Journal of chemical physics* 111.15 (1999), 7010–7022.

[73] G. Kresse and J. Hafner. "Ab initiomolecular dynamics for open-shell transition metals". *Physical Review B* 48.17 (Jan. 1993), 13115–13118.

[74] G. Kresse and D. Joubert. "From ultrasoft pseudopotentials to the projector augmented-wave method". *Physical Review B* 59.3 (1999), 1758–1775.

[75] John P. Perdew, Kieron Burke, and Matthias Ernzerhof. "Generalized Gradient Approximation Made Simple". *Physical Review Letters* 77.18 (1996), 3865–3868.

[76] Stefan Grimme. "Semiempirical GGA-type density functional constructed with a long-range dispersion correction". *Journal of Computational Chemistry* 27.15 (2006), 1787–1799.

[77] Martin Korth. "Error estimates for (semi-) empirical dispersion terms and large biomacromolecules". *Organic & biomolecular chemistry* 11.38 (2013), 6515–6519.

[78] Wei Liu, Victor G Ruiz, Guo-Xu Zhang, Biswajit Santra, Xinguo Ren, Matthias Scheffler, and Alexandre Tkatchenko. "Structure and energetics of benzene adsorbed on transition-metal surfaces: Density-functional theory with van der Waals interactions including collective substrate response". *New Journal of Physics* 15.5 (2013), 053046.

[79] Neyvis Almora-Barrios, Giuliano Carchini, Piotr Błoński, and Núria López. "Costless derivation of dispersion coefficients for metal surfaces". *Journal of chemical theory and computation* 10.11 (2014), 5002–5009.

[80] Stefan Grimme, Jens Antony, Stephan Ehrlich, and Helge Krieg. "A consistent and accurate ab initio parametrization of density functional dispersion correction (DFT-D) for the 94 elements H-Pu". *The Journal of chemical physics* 132.15 (2010), 154104.

[81] Stefan Grimme, Stephan Ehrlich, and Lars Goerigk. "Effect of the damping function in dispersion corrected density functional theory". *Journal of computational chemistry* 32.7 (2011), 1456–1465.

[82] James D. Pack and Hendrik J. Monkhorst. ""Special points for Brillouin-zone integrations"". *Physical Review B* 13.12 (1976), 5188.

[83] Péter Pulay. "Convergence acceleration of iterative sequences. The case of SCF iteration". *Chemical Physics Letters* 73.2 (1980), 393–398.

[84] H Jónsson, G Mills, and KW Jacobsen. *Classical and quantum dynamics in condensed phase simulations*. 1998.

[85] Søren Smidstrup, Andreas Pedersen, Kurt Stokbro, and Hannes Jónsson. "Improved initial guess for minimum energy path calculations". *The Journal of chemical physics* 140.21 (2014), 214106.

[86] Steve Plimpton. "Fast parallel algorithms for short-range molecular dynamics". *Journal of computational physics* 117.1 (1995), 1–19.

[87] Glenn J Martyna, Michael L Klein, and Mark Tuckerman. "Nosé–Hoover chains: The canonical ensemble via continuous dynamics". *The Journal of chemical physics* 97.4 (1992), 2635–2643.

[88] Guodong Wen, Yunpeng Xu, Huaijun Ma, Zhusheng Xu, and Zhijian Tian. "Production of hydrogen by aqueous-phase reforming of glycerol". *International Journal of Hydrogen Energy* 33.22 (2008), 6657–6666.

[89] David L King, Liang Zhang, Gordon Xia, Ayman M Karim, David J Heldebrant, Xianqin Wang, Tom Peterson, and Yong Wang. "Aqueous phase reforming of glycerol for hydrogen production over Pt–Re supported on carbon". *Applied Catalysis B: Environmental* 99.1-2 (2010), 206–213.

[90] Yunpeng Xu, Zhijian Tian, Guodong Wen, Zhusheng Xu, Wei Qu, and Liwu Lin. "Production of CO x-free hydrogen by alkali enhanced hydrothermal catalytic reforming of biomass-derived alcohols". *Chemistry letters* 35.2 (2006), 216–217.

[91] William L Jorgensen and Julian Tirado-Rives. "The OPLS [optimized potentials for liquid simulations] potential functions for proteins, energy minimizations for crystals of cyclic peptides and crambin". *Journal of the American Chemical Society* 110.6 (1988), 1657–1666.

[92] Daniel J Price and Charles L Brooks III. "A modified TIP3P water potential for simulation with Ewald summation". *The Journal of chemical physics* 121.20 (2004), 10096–10103.

[93] Hendrik Heinz, Tzu-Jen Lin, Ratan Kishore Mishra, and Fateme S Emami. "Thermodynamically consistent force fields for the assembly of inorganic, organic, and biological nanostructures: the INTERFACE force field". *Langmuir* 29.6 (2013), 1754–1765.

[94] HA Lorentz. "Ueber die Anwendung des Satzes vom Virial in der kinetischen Theorie der Gase". *Annalen der physik* 248.1 (1881), 127–136.

[95] M Schoen and C Hoheisel. "The mutual diffusion coefficient D 12 in binary liquid model mixtures. Molecular dynamics calculations based on Lennard-Jones (12-6) potentials: I. The method of determination". *Molecular Physics* 52.1 (1984), 33–56.

[96] Ahmed E Ismail, Gary S Grest, and Mark J Stevens. "Capillary waves at the liquid-vapor interface and the surface tension of water". *The Journal of chemical physics* 125.1 (2006), 014702.

[97] Giovanna Longhi, Alberto Ceselli, Sandro L Fornili, Sergio Abbate, Leopoldo Ceraulo, and Vincenzo Turco Liveri. "Molecular dynamics of electrosprayed water nanodroplets containing sodium bis (2-ethylhexyl) sulfosuccinate". *Journal of Mass Spectrometry* 48.4 (2013), 478–486.

Chapter 3

A DFT and MD Study of Aqueous-phase Dehydrogenation of Glycerol on Pt (1 1 1): Comparing Chemical Accuracy versus Computational Expense in Different Methods for Calculating Aqueous-phase System Energies

3.1 Abstract

Understanding reaction mechanisms is a crucial step to better catalyst design; however, this understanding is often limited for reactions in the aqueous phase due to uncertainties in how fluctuations in the structure of liquid water may influence catalytic thermodynamics and kinetics.

Characteristic quantities for example reaction energies, are among the most investigated list. Knowing if a reaction is endothermic or exothermic, and further how does it compare to other parallel reactions, can be a powerful tool to screen reactions and even materials such as catalysts. In this chapter, we present a combination of density functional theory (DFT) and classical force field based molecular dynamics (MD) to simulate the structures of liquid water and to assess its influence on the catalytic thermodynamics of Pt-catalyzed aqueous phase reforming (APR) of glycerol ($C_3H_8O_3$). While this developed multi-scale simulation strategy is used for its balanced chemical accuracy and efficiency, challenge still exists, that exploring the comprehensive reaction network, including various reaction branches of glycerol APR requires a significant number of coupled DFT and MD calculations and pre and post processing. We present the linear scaling relations (LSRs), which can treat energies of interest of different surface species in terms of linear combination of their energy descriptors. This not only can greatly reduce the computational effort to calculate such aqueous phase catalytic thermodynamics, but also enables an alternative way to screen potential dominant reaction species and reaction pathways. It is shown that this method is both computationally tractable and accurate. This chapter will cover the derivation of this method, and its application to efficiently interrogate the structures of liquid water and its energetic contribution to the water- catalyst interface.

3.2 Introduction

In this work, we identify an approach that can be used to study glycerol APR intermediates in aqueous conditions in a way that captures the liquid environment and the large reaction network yet remains computationally tractable. Prior studies from the groups of Greeley [1, 2], and Vlachos [3] have provided detailed information on the geometries and energies of different adsorbates and transition states in catalytic glycerol decomposition under vacuum conditions. Our group is interested in how water influences the energies of these reaction intermediates and transition states. The liquid water environment introduces complexity into the simulations for at least two reasons. One, water molecules interact with surface intermediates [4–10], which can influence their energies or even adsorption geometries. Two, in some cases it is necessary to include multiple configurations of H_2O molecules in the calculations, due to configurational disorder in the structure of liquid water. This increases the cost of the computational analysis, since multiple H_2O configurations must be sampled over for each reaction intermediate [11]. Given that glycerol APR can include dehydrogenation, de-

carbonylation, dehydration, hydrolysis, water gas shift and other processes [12], to study the entire reaction network, including multiple configurations of H_2O molecules for each reaction intermediate and transition state, would require a significant amount of effort. Due to the large reaction network and the need to study it in liquid conditions, we are seeking ways to reduce the computational expense of performing simulations of heterogeneously catalysed reactions in aqueous phase.

In this work, we use computational strategies to investigate intermediates and reactions in Pt(1 1 1)-catalysed glycerol dehydrogenation under liquid water. We explore three methods for calculating the aqueous-phase energies of glycerol and its derivatives of dehydrogenation. In one method, the adsorbate geometries and binding energies in vacuum are determined with density functional theory (DFT), and H_2O configurations are generated in classical molecular dynamics (MD) simulations. The water–adsorbate interaction energies (needed to compute the binding energies and reaction energies in aqueous conditions) are then calculated using DFT single point calculations performed on some of the H_2O–adsorbate configurations generated in MD [11]. In the second method, vacuum-phase binding energies and adsorbate geometries are determined in DFT, H_2O configurations are generated in MD and the H_2O–adsorbate interaction energies are calculated from the classical potentials employed in the MD simulations. In the third method, a linear scaling relationship (LSR) [4, 13–19] is used to compute the adsorbate binding energies, H_2O configurations are generated in MD and the water–adsorbate interaction energies are calculated using the classical potentials in MD. In the third method, the adsorbate structures needed in the MD simulations are produced through 'coarse' (i.e. partial) geometry relaxations in DFT. We find the second and third methods achieve good computational efficiency while attaining good accuracy for calculating reaction energies in the aqueous phase when compared to the results of the first method (which is an adaptation of a method previously published by our group [11]); however, they give significantly different results for the H_2O–adsorbate interaction energies.

3.3 Methods

3.3.1 Model Structures: General Details

Different model systems in this work are comprised of intermediates in the glycerol decomposition pathway adsorbed to platinum(1 1 1) at low coverage under vacuum and liquid water. The total coverage of adsorbates on the Pt(1 1 1) surfaces is held at 1/9 monolayer (ML), where 1 ML

refers to 1 adsorbate molecule per surface metal atom. Initial guesses for adsorbate geometries are made by referencing prior work from the Greeley [1, 2], and Vlachos [3] groups. Final adsorbate geometries are determined using geometry relaxations in DFT. Configurations of liquid water molecules are determined using MD.

3.3.2 DFT calculations

DFT calculations were performed based on information provided in Chapter 2 section 5.

3.3.3 MD Simulations

MD simulations are performed with the Large-scale Atomic/ Molecular Massively Parallel Simulator (LAMMPS) [20] in the NVT ensemble. The target temperature is set at 500 K with the Nose–Hoover thermostat [21]. This temperature is chosen to replicate the experimental conditions of aqueous-phase reforming of oxygenated hydrocarbons [22–25]. MD simulations are performed for 5 ns (5×10^{-9} s) with 1 fs (10^{-15} s) time steps, where the first 2 ns are used for system equilibration and the remaining 3 ns are used for the production runs. Atomic quantities and thermodynamic information are reported every 100 fs. Non-bonded water-water, water–adsorbate and water–Pt interactions are calculated with Lennard-Jones + Coulomb (LJ + C) potentials, with LJ parameters and partial electronic charges (Coulomb parameters) for adsorbates, H_2O and Pt taken from the optimised potentials for liquid simulations (OPLS) [26], TIP3P [27] and INTERFACE force fields [28], respectively. Cross-terms for the LJ interactions are computed using Lorentz–Berthelot mixing rules [29, 30]. All LJ cross-term coefficients and partial charges used in the LJ + C potentials are given in SI Section 2 of Reference [31], which is available at https://www.tandfonline.com/doi/abs/10.1080/08927022.2017.1285403. In this chapter, unless otherwise stated, all SI occurrences refer to this electronic source. A total of 36 H_2O molecules are present in the simulation boxes. Note the system size was limited in order to allow feasible DFT energy calculations. During MD simulations, these H_2O molecules provide an explicit solvation environment as they form a liquid film, which is stabilised near the surface region. Similar liquid water films were observed at 500 K using TIP3P water in MD by Ismail et al. [32] and Longhi et al. [33].

3.3.4 Simulation Supercell

In this chapter, a close-pack 3-layer 3×3 $p(3\frac{\sqrt{2}}{2} \times 3\frac{\sqrt{2}}{2} - R60^{c}irc)$ Pt (111) surface is discussed as the simulated catalyst. The $3\frac{\sqrt{2}}{2}$ in the $p(3\frac{\sqrt{2}}{2} \times 3\frac{\sqrt{2}}{2} - R60^{c}irc)$ expression indicates the corresponding a and b dimensions of the unit cell, with respect to the lattice parameter of the primitive cell of Pt; the $R60^{c}irc$ indicates the angle formed in between lattice vector $\boldsymbol{a}$ and lattice vector $\boldsymbol{b}$ is $60^{c}irc$. The lateral dimensions of the mono-clinic Pt (111) slab can be found in Figure 3.1. Surfaces with the same periodicity are reported in various existing literature [34–41] due to easy implementation and computational efficiency. However, a major concern of applying this model is the lateral interactions on the x-y plane when the cells are expanded in periodic boundary conditions (PBC), which is caused by the $3\frac{\sqrt{2}}{2}$ cell shape. In our published work [31] (SI Section 3), it has been shown that small adsorbed molecules such as methanol and its derivatives are suitable for this type of unit cell, as the binding energies for those small chemical species on the 3×3 Pt (111) surface are with in ~ 0.15 eV (1 eV = 96.49 kJ/mol) of their analogues calculated on a larger 6×6 Pt (111) surface. The distance between the topmost layer of Pt atoms and the bottommost layer of Pt atoms in the next periodic image is 34 Å, which allows for the incorporation of H_2O molecules into the supercells and minimises the interactions between periodic images in the vertical dimension. The total size of the super cells is thus $a = b = 8.416$ Å, $c = 38.524$ Å, $\alpha = \beta = 90.0^{c}irc$, $\gamma = 60.0^{c}irc$ (volume = 2363 Å^3). These super cells are used in both the DFT and MD simulations. In DFT calculations of these super cells, $7 \times 7 \times 1$ Γ-centred Monkhorst-Pack k-point grids [42] are used to integrate over the first Brillouin zones.

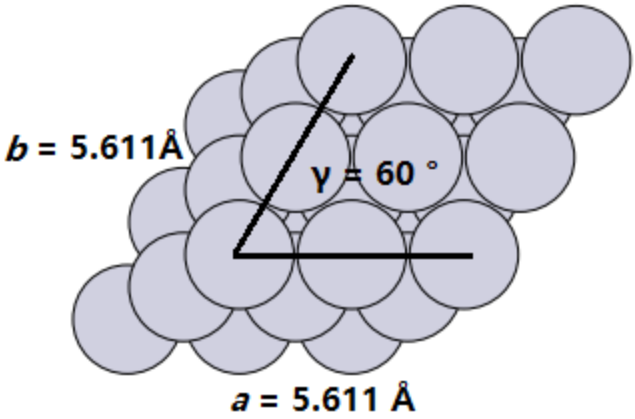

Figure 3.1: Top view of $p(3\frac{\sqrt{2}}{2} \times 3\frac{\sqrt{2}}{2} - R\ 60^{c}irc)$ Pt (111) catalyst model (unit cell). The light grey circles denote Pt atoms of the surface. Information about a, b, and γ is labeled in the graph.

3.3.5 Gas-phase Molecules and Radicals

Energies of gas-phase molecules, including fully saturated molecules and radicals, are calculated in non-cubic 14.000 Å × 13.014 Å × 13.029 Å super cells. Spin polarisation is included as appropriate. The k-point grid is $1 \times 1 \times 1$.

3.3.6 Methods and quantities for calculating energies in aqueous phase

In this work, we compare three ways for computing the energies of reaction intermediates in the presence of liquid H_2O. They are detailed below.

3.3.6.1 Full DFT/MD method

The first method is a modification of the strategy published previously by our group [11]. Briefly, the procedure is as follows:

1. Adsorbate structures are optimised using DFT under vacuum.

2. In our previously published procedure, the converged structures were then placed under sheets of ice and allowed to re-relax. The intended purpose of introducing the ice sheet was to capture any geometry differences that might occur in the presence of H_2O molecules. In general, we find that this step has a minor effect on the structures and energies of the adsorbates considered in work of SI Section 4.

3. The systems are then simulated in MD. In these simulations, the H_2O molecules are allowed to move according to Newton's equations of motion, but the adsorbate is held fixed.

4. Ten different configurations of H_2O molecules are selected from the MD trajectory. These are obtained by sampling every 100 timesteps during the production stage. The energies of these configurations are calculated in DFT as single points (i.e. without relaxing any of positions of any of the atoms). These DFT energies are averaged, and the result is taken as the averaged electronic energy of the aqueous-phase system. (As discussed below, in this step, an additional 10 DFT single points need to be performed on the identical H_2O configurations but with the adsorbate removed [11]. These single point energies are needed to compute the water–adsorbate interaction energies.)

We consider this procedure, which we call full DFT/MD, to be our standard, since the energies are calculated with DFT. However, since the energies calculated with DFT use H_2O configurations produced with a classical force field, this method could comprise some amount of uncertainty, since the exact positions of the local minima and the forces along the potential energy surface are different, depending on whether DFT or the classical force field is used to generate it. We discuss some possible sources of uncertainty in SI Sections 5 and 6. As shown below, a more useful quantity than the aqueous-phase system electronic energy is the water-adsorbate (i.e. the water-$C_3H_yO_3$*) interaction energy, i.e. $E_{\mathrm{int}}(C_3H_yO_3)$ [27],

$$\Delta E_{\mathrm{int}}(C_3H_yO_3) = E(\mathrm{Pt} + H_2O + C_3H_yO_3) - E(\mathrm{Pt} + H_2O) - E(\mathrm{Pt} + C_3H_yO_3) + E(\mathrm{Pt}) \quad (3.1)$$

where E stands for electronic energy. In this equation, the configurations of H_2O molecules used to calculate E(Pt + H_2O) are the same as those used to calculate E(Pt + H_2O + $C_3H_yO_3$). Still, to obtain E_{int} requires an additional 10 DFT calculations, needed to calculate E(Pt + H_2O). Thus, a total of 21 DFT calculations are required to calculate the interaction energy for one adsorbate in the full DFT/MD approach: 1 in step 1 and 20 in step 3. Given that the pathway for glycerol APR involves hundreds of possible reaction intermediates, this method is too computationally expensive for routine use.

3.3.6.2 Vacuum DFT/MD method

In this work, we evaluate two alternative methods for reducing the computational expense needed to calculate E_{int}. In the first alternative, which we call the Vacuum DFT/MD method, we eliminate step 3 from the procedure enumerated above, which requires 20 DFT single point calculations. In this method, E_{int} is calculated directly from the MD simulations, using pair- wise LJ + C interaction energies calculated between the atoms in the adsorbate and the atoms in water. Note that this direct MD energy calculation method does not attain quantum accuracy; however, it offers notable computational efficiency since the averaging of E_{int} in MD simply requires the completion a MD trajectory, which takes about 1/10th of the time required to perform the 20 DFT single point calculations that would be needed in the full DFT/MD method. In addition, the ensemble averages of the interaction energies can be calculated using many configurations from the MD production run, rather than just the 10 that are used in full DFT/MD. (That said, we find that for the systems studied in this work, the averages and uncertainties of the interaction energies calculated using LJ + C potentials in MD from 10 configurations versus 30,000 configurations are nearly identical. See SI Section 7.) Using the LJ + C energies directly from MD, 20 of the 21 DFT calculations needed to compute E_{int} are eliminated in this method.

3.3.6.3 LSR/MD Method

This method uses an established linear scaling relashionship (LSR) to obtain binding energies and correlate them to reaction energies. Detailed derivation of the LSR is discussed in Chapter 2 Section 2.2.

The second part of LSR/MD method uses the MD simulator to eliminate the need to compute the binding energies of reaction intermediates with DFT. However, the structures of these intermediates are still needed as input for the MD simulations needed to obtain $E_{\text{int}}(C_3H_yO_3)$. In order to reduce the computational expense associated with obtaining these structures, we use 'coarsely converged' structures in our LSR/MD method, i.e. where geometry relaxations of $C_3H_yO_3$ intermediates are performed until the maximum atomic force falls below 0.5 eV/Å (compared to 0.03 eV/Å needed for full convergence) [31]. In general, geometry relaxations performed using coarse convergence take 80 fewer iterations to converge than the analogues that are converged to 0.03 eV/Å. Further, the differences in E_{int} using these coarsely converged structures in the LSR/MD method

are found to be within the error bars of the E_{int} calculated using the fully converged structures in the vacuum DFT/MD method (SI Section 8). Note that these coarsely converged structures are only used to provide a reasonable adsorbate structures for the MD simulations and not to obtain any DFT energies.

3.3.6.4 Derivation of Aqueous-phase Reaction Energies

To evaluate these different methods, we use them to compute binding energies and reaction energies along the glycerol dehydrogenation pathway. The binding energies of reaction intermediates under vacuum can be calculated in two ways: with DFT energies or using the LSR. Using DFT energies, the equation is,

$$E^{\text{vac}}_{\text{bind}}(\text{C}_3\text{H}_{y'}\text{O}_3) = E(\text{Pt} + \text{C}_3\text{H}_{y'}\text{O}_3) - E(\text{Pt}) - E(\text{C}_3\text{H}_{y'}\text{O}_3(\text{g})) \tag{3.2}$$

Where $E(\text{C}_3\text{H}_{y'}\text{O}_3(\text{g}))$ is the energy of gas-phase $\text{C}_3\text{H}_{y'}\text{O}_3$, which can be either a saturated molecule or an unsaturated fragment. It is previously reported that $E^{\text{vac}}_{\text{bind}}$ can be summed with the water–adsorbate interaction energy (E_{int}) to obtain the aqueous-phase binding energy [11],

$$E^{\text{aq}}_{\text{bind}}(\text{C}_3\text{H}_{y'}\text{O}_3) = E^{\text{vac}}_{\text{bind}}(\text{C}_3\text{H}_{y'}\text{O}_3) + E_{\text{int}} \tag{3.3}$$

Which represents the chemical formula $\text{C}_3\text{H}_y\text{O}_3(\text{g})$ + Pt(aq) → $\text{C}_3\text{H}_y\text{O}_3$–Pt(aq). Similarly, the reaction energies for aqueous-phase dehydrogenations, i.e. $\text{C}_3\text{H}_y\text{O}_3$—Pt(aq) + Pt(aq) → $\text{C}_3\text{H}_{y-1}\text{O}_3$–Pt(aq) + H–Pt(aq), are calculated by summing the reaction energies in vacuum with the change in the water–adsorbate interaction energies going from reactants to products. Using values from DFT, the reaction energies in vacuum are calculated as follows:

$$E^{\text{vac}}_{\text{rxn}}(\text{C}_3\text{H}_{y'}\text{O}_3 \rightarrow \text{C}_3\text{H}_{\text{y-1}}\text{O}_3) = E(\text{Pt} + \text{C}_3\text{H}_{\text{y-1}}\text{O}_3) - E(\text{Pt} + \text{C}_3\text{H}_{\text{y}}\text{O}_3) + E(\text{H}) \tag{3.4}$$

where $E(\text{H})$ is the energy of single adsorbed H atom. When the LSR/MD method is used, DFT energies are not available, and $E^{\text{vac}}_{\text{rxn}}(\text{C}_3\text{H}_{y'}\text{O}_3 \rightarrow \text{C}_3\text{H}_{\text{y-1}}\text{O}_3)$ can be calculated from the binding

energies obtained from the LSR, i.e.

$$E^{\mathrm{vac}}_{\mathrm{rxn}}(\mathrm{C_3H_{\mathit{y'}}O_3} \rightarrow \mathrm{C_3H_{y\text{-}1}O_3}) = E^{\mathrm{vac}}_{\mathrm{bind}}(\mathrm{C_3H_{y\text{-}1}O_3}) - E^{\mathrm{vac}}_{\mathrm{bind}}(\mathrm{C_3H_yO_3}) + E(\mathrm{C_3H_{y\text{-}1}O_3}(g)) - E(\mathrm{C_3H_yO_3}(g)) + E(\mathrm{H}) \tag{3.5}$$

where $E(\mathrm{C_3H_{y\text{-}1}O_3}(g))$, $E(\mathrm{C_3H_yO_3}(g))$, and $E(\mathrm{H})$ are calculated with DFT. The derivation of eqn. 3.5 is provided in SI Section 9. The aqueous-phase reaction energy (for both cases) is then given by

$$E^{\mathrm{aq}}_{\mathrm{rxn}}(\mathrm{C_3H_{\mathit{y'}}O_3} \rightarrow \mathrm{C_3H_{y\text{-}1}O_3}) = E^{\mathrm{vac}}_{\mathrm{rxn}}(\mathrm{C_3H_{\mathit{y'}}O_3} \rightarrow \mathrm{C_3H_{y\text{-}1}O_3}) + \Delta E_{\mathrm{int}} \tag{3.6}$$

where ΔE_{int} the difference between the E_{int} of the product and the E_{int} of the reactant.

3.3.6.5 Summary of methods and how $E^{\mathrm{vac}}_{\mathrm{bind}}$ and E_{int} are calculated

We now have three different methods for calculating the energies of aqueous-phase systems:

- 'Full DFT/MD,' as reported by Bodenschatz et al. [11] (except that the step (1a), which re-converges the vacuum structures under ice, is eliminated).
- 'Vacuum DFT/MD,' which calculates E_{int} using pairwise LJ + C potentials in MD.
- 'LSR/MD,' which obtains $E^{\mathrm{vac}}_{\mathrm{bind}}(\mathrm{C_3H_{\mathit{y}}O_3})$ from the LSR in eqn. 2.1, uses coarsely converged adsorbate structures in MD and calculates E_{int} using pairwise LJ + C potentials in MD.

These methods, along with the associated methods for calculating E_{int} are summarised in Table 3.1. The 'Steps' are previously discussed in the text.

Table 3.1: Methods used to compute the energies of reaction intermediates used in this work and descriptions of how $E_{\mathrm{int}}(C_3H_yO_3)$ and $E_{\mathrm{int}}(C_3H_yO_3)$ are calculated for each method.

Method	**Step (1)**	**Step (2)**	**Step (3)**	$E_{\mathrm{bind}}^{\mathrm{vac}}(C_3H_yO_3)$ calculation	$E_{\mathrm{int}}(C_3H_yO_3)$ calculation
Full DFT/MD	Structure converged to 0.03 eV/Å	Configurations of water obtained with MD	Single point energies calculated with DFT	From fully converged structures, using DFT	From DFT, as described above (20 calculations necessary)
Vacuum DFT/MD	Structure converged to 0.03 eV/Å	Configurations of water obtained with MD	Energies calculated in MD	From fully converged structures, using DFT	Directly from MD, using structures converged to 0.03 eV/Å in DFT
LSR/MD	Structure converged to 0.50 eV/Å	Configurations of water obtained with MD	Energies calculated in MD	linear scaling relationship, using (equation (\ref{LSR}))	Directly from MD, using structures converged to 0.50 eV/Å in DFT

3.3.6.6 Adsorbates and reactions used for energy comparisons

There are 84 possible intermediates (including glycerol) in the pathway for the total dehydrogenation of glycerol, and 250 possible elementary dehydrogenation reactions, involving both C–H and O–H dissociation. Table 3.2 categorises the 84 adsorbates into 8 tiers based on their hydrogen contents, with Tier 1 representing the stoichiometry $C_3H_7O_3$, and Tier 8 representing $C_3H_0O_3$. The analysis below is performed on a subset comprising 35 of these adsorbates, chosen based on the following criteria. We selected a maximum of five intermediates from each tier, and we focused on intermediates that exhibited the largest, most exothermic aqueous-phase dehydrogenation reaction energies, calculated using the three approaches discussed above. Starting from the selected 35 intermediates, 70 dehydrogenation reactions were considered, which exhibit different levels of exothermicity and endothermicity.

Table 3.2: intermediates from the glycerol dehydrogenation pathway, categorized into different tiers by their hydrogen contents.

Tier	Formula	Intermediates
1	$C_3H_7O_3$	CHOH–CHOH–CH_2OH, CH_2OH–COH-CH_2OH, CH_2O–CHOH–CH_2OH, CH_2OH–CHO–CH_2OH
2	$C_3H_6O_3$	CHOH–CHOH–CHOH, CH_2O–COH–CH_2OH, CHOH–COH–CH_2OH, CHOH–CHO–CH_2OH, CH_2O–CHO–CH_2OH, COH–CHOH–CH_2OH, CHO–CHOH–CH_2OH, CH_2O–CHOH–CH_2O, CHOH–CHOH–CH_2O, CH_2OH–CO–CH_2OH
3	$C_3H_5O_3$	COH–CHOH–CHOH, CO–CHOH–CH_2OH, COH–CHOH–CH_2O, CHOH–CO–CH_2OH, CHOH–COH–CH_2O, CHOH–COH–CHOH, COH–COH–CH_2OH, COH–CHO–CH_2OH, CH_2O–CHO–CH_2O, CH_2O–CO–CH_2OH, CHOH–CHO–CH_2O, CH_2O–COH–CH_2O, CHO–CHOH–CHOH, CHO–COH–CH_2OH, CHO–CHO–CH_2OH, CHO–CHOH–CH_2O
4	$C_3H_4O_3$	COH–COH–CHOH, COH–COH–CH_2O, CHOH–CO–CH_2O, COH–CHO–CH_2O, CHOH–CO–CHOH, COH–CO–CH_2OH, CO–COH–CH_2OH, COH–CHO–CHOH, COH–CHOH–COH, CHO–COH–CHOH, CO–CHOH–CHOH, CHO–CO–CH_2OH, CHO–COH–CH_2O, CHO–CHO–CHOH, CO–CHOH–CH_2O, CHO–CHOH–COH, CH_2O–CO–CH_2O, CO–CHO–CH_2OH, CHO–CHOH–CHO, CHO–CHO–CH_2O
5	$C_3H_3O_3$	CHOH–COH–CO, CHOH–CHO–CO, COH–CHOH–CO, CH_2O–COH–CO, COH–COH–CHO, CHOH–CO–CHO, CHO– CHOH–CO, COH–COH–COH, CH_2OH–CO–CO, CHOH–CO– COH, CH_2O–CHO–CO, CH_2O–CO–CHO, CH_2O–CO–COH, CHO–CHO–CHO, CHO–CHO–COH, CHO–COH–CHO, COH–CHO–COH
6	$C_3H_2O_3$	CH_2O–CO–CO, CHO-CHO–CO, CHO–CO–CHO, CHOH–CO–CO, CHO–CHO–CO, CHO–CO–COH, COH–CHO–CO, COH–COH–CO, COH–CO–COH, CO–CHOH–CO
7	$C_3H_1O_3$	CHO–CO–CO, CO–CHO–CO, COH–CO–CO, CO–COH-CO
8	$C_3H_0O_3$	CO–CO–CO

note: intermediates that were calculated in this work are underlined.

3.4 Results

Vacuum-phase binding energies, aqueous-phase binding energies, interaction energies and aqueous-phase reaction energies for the 35 intermediates/70 reactions discussed above are calculated using the three methods discussed above and compared in Figures 1–3 and Tables S10–S12 in SI.

In the remainder of this section, we compare results calculated with the Vacuum DFT/MD and LSR/MD methods with the full DFT/MD method, since we consider the full DFT/MD method to be the standard. We use two statistics to evaluate the vacuum DFT/MD and LSR/MD methods: (1) the correlation coefficient, R^2, obtained by creating a best fit line for an energy calculated with the method of interest versus the same energy but calculated with the full DFT/MD method; and (2) the mean absolute error (MAE), which is the average of the absolute value of the difference between an energy calculated with the method of interest and the same energy but calculated with the full DFT/MD method. A comparison of E_{int} is provided in Figure 3.2. In calculating E_{int}, the main difference between the vacuum DFT/MD and LSR/MD methods and the full DFT/MD method is whether the interaction energies are calculated with LJ + C potentials (vacuum DFT/MD and LSR/MD) or with DFT (full DFT/MD). Figure 3.2 shows that the correlation between the interaction energies calculated with LJ + C potentials and those calculated with DFT is weak, with R^2 values of 0.39 and 0.25 for the Vacuum DFT/MD and LSR/MD methods, respectively. Further, the MAEs, which assesses the accuracies of the methods, are 0.43 and 0.48 eV, respectively. These values are larger than our chosen MAE tolerance of 0.3 eV. This value was chosen to be consistent with the literature [14, 43, 44].

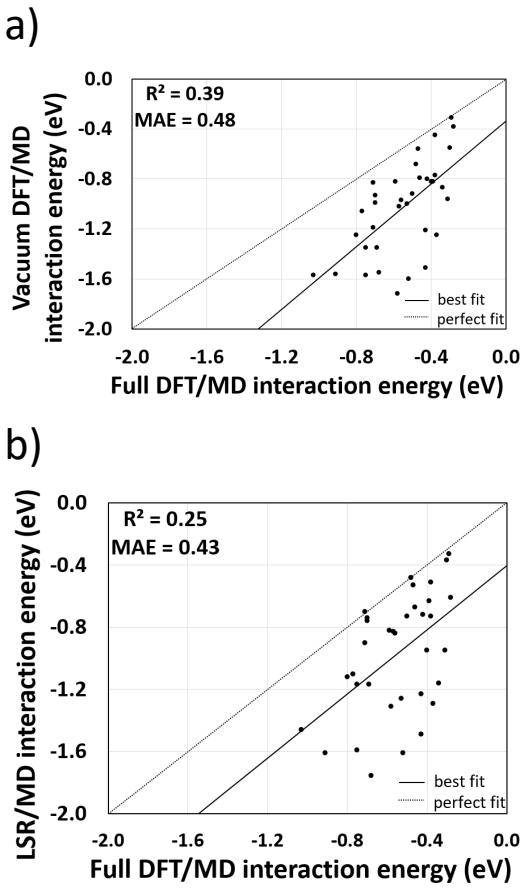

Figure 3.2: (a) comparison of the water–adsorbate interaction energies calculated using the full DFT/MD and vacuum DFT/MD methods. (b) comparison of the water–adsorbate interaction energies of the of 35 reaction intermediates calculated using the full DFT/MD and LSR/MD methods. For clarity, the graphs only plot the averaged values and do not include error bars. The grey line is the $y = x$ line, and the black line is the best fit line obtained using the method of least squares.

Figure 3.3 compares binding energies calculated with the different methods. Vacuum-phase binding energies calculated with the LSR are compared with their DFT-calculated analogues in Figure 3.3(a). We find good correlation and accuracy, with $R^2 = 0.98$ and MAE = 0.14 eV, indicating that the LSR is viable for calculating vacuum-phase binding energies. Aqueous-phase binding

energies calculated with the vacuum DFT/MD and LSR/ MD methods are compared with the full DFT/MD method in Figures 3.3(b) and (c), respectively. Both of these methods give aqueous-phase binding energies that are well correlated to the energies calculated with the full DFT/MD method, with R^2 values of 0.98 and 0.96, respectively. However, the MAE values are large, both around 0.5 eV. We find that E_{int} contributes on average 20% to the aqueous-phase binding energies, and it is likely the scatter in E_{int} that leads to the large MAEs in the aqueous-phase binding energies calculated with the vacuum DFT/MD and LSR/ MD methods.

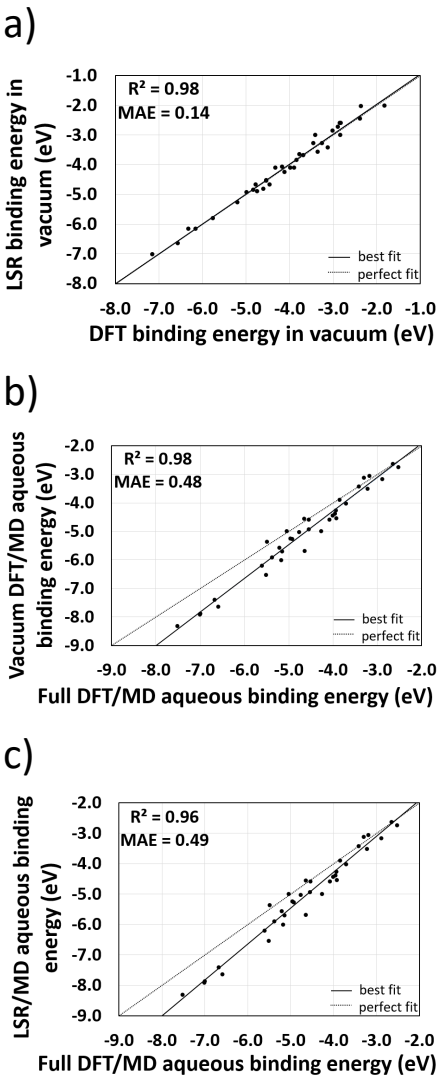

Figure 3.3: (a) comparison of vacuum-phase binding energies of the selected 35 reaction intermediates calculated with DFT vs. with LSR. (b) comparison of aqueous-phase binding energies calculated using the vacuum DFT/MD method vs. the full DFT/MD method. (c) comparison of aqueous-phase binding energies calculated using the LSR/MD method vs. the full DFT/MD method. For clarity, the graphs only plot the averaged values and do not include error bars. The grey line is the $y = x$ line, and the black line is the best fit line obtained using the method of least squares.

Vacuum-phase reaction energies calculated using values from the LSR are compared with

the analogous values calculated with DFT in Figure 3.4(a). We find reasonable correlation with R^2 = 0.79 and good accuracy, with MAE = 0.17 eV. Aqueous-phase reaction energies calculated with the vacuum DFT/MD and LSR/MD approaches are compared with the analogous values calculated with the full DFT/MD method in Figure 3.4(a) and (b), respectively. We find that even though these methods give E_{int} that are only loosely correlated to and remarkably different from the E_{int} that are calculated with the full DFT/MD approach, they are viable for calculating $E_{\text{rxn}}^{\text{aq}}$. The R^2 values for these methods are 0.88 and 0.84, respectively, and the MAEs are 0.24 and 0.28 eV, respectively. Notably, the MAEs are within our tolerance value of 0.3 eV.

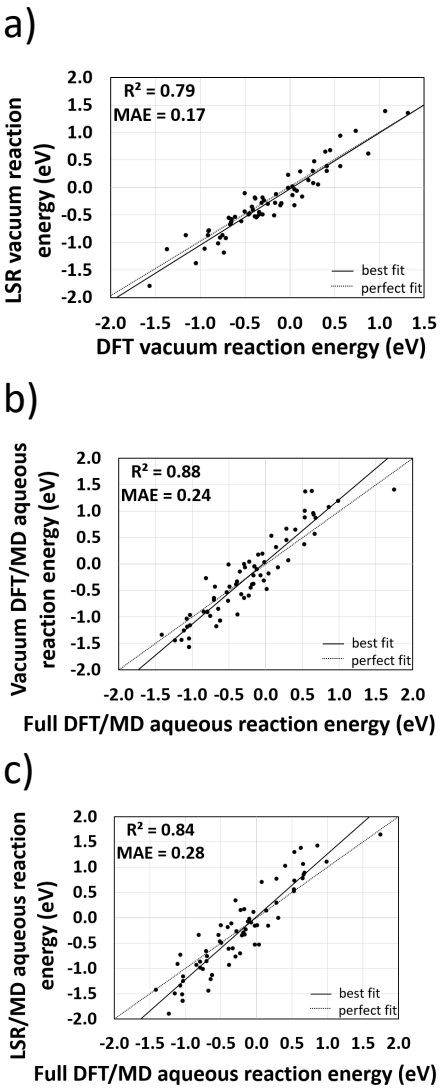

Figure 3.4: (a). comparison between vacuum-phase reaction energies calculated with DFT vs. the LSR. (b). comparison between the aqueous-phase reaction energies calculated using the vacuum DFT/MD method vs. the full DFT/MD method. (c). comparison between the aqueous-phase reaction energies calculated using the LSR/MD method vs. the full DFT/MD method. For clarity, the graphs only plot the averaged values and do not include error bars. The grey line is the $y = x$ line, and the black line is the best fit line obtained using the method of least squares.

3.5 Discussion

The interaction energy E_{int} is an important quantity in computational catalyst of aqueous-phase reaction studies. This is because it describes the strength of interaction between the water and the adsorbate, which can lead to different binding phenomena than in vacuum. Additionally, the interaction energy contributes to the reaction energy and thus the free energy difference in chemical reactions. However, this quantity is computationally expensive to obtain [11]. In this work, we evaluated using classical LJ + C potentials to obtain the water–adsorbate interaction energies instead of DFT, in order to reduce the computational expense. We found that the LJ + C method used in this work gives significantly different E_{int} than DFT does. However, when relative values of E_{int} are needed, as in the calculation of $E_{\text{rxn}}^{\text{aq}}$, the LJ + C method gives results that are in line with DFT. In part, this is because the vacuum-phase reaction energy, which yields good statistics, is the dominant contribution to the aqueous-phase reaction energy. The other contribution to $E_{\text{rxn}}^{\text{aq}}$ is ΔE_{int}, which gives better statistics than E_{int} due to cancellation of error. This is discussed further in SI Section 13.

Of the two methods that use the LJ + C potentials investigated in this work (i.e. vacuum DFT/MD and LSR/MD), the LSR/MD method is more efficient, because it only requires one coarsely converged DFT calculation per adsorbate. However, a hidden source of computational expense is in the establishment of the LSR itself. LSRs such as the one used in this work are limited to certain types of species [14, 16, 17], and thus new LSRs must be developed to study different reaction systems, and maybe even different branches of a reaction network in a single system. Further, calculating $E_{\text{rxn}}^{\text{aq}}$ with this method requires calculating energies for the gas-phase molecules and radicals with DFT, which adds to the computational expense. Thus, while it is the most computationally efficient method that we know of that incorporates explicit solvation and multiple configurations of H_2O molecules for computing reaction energies at quantum-level accuracy, the LSR/MD method still involves notable computational effort.

Finally, we note that all energies reported in this manuscript are electronic energies. Some of our ongoing work involves learning how to calculate other quantities (e.g. free energies).

3.6 Conclusions

Understanding aqueous-phase reforming of glycerol on Pt (1 1 1) remains challenging, due to the large amount of reactions and intermediates that are involved. Here, we provide a relatively efficient method for computing the reaction energies of surface reactions under aqueous phase. Specifically, this method uses an LSR to compute adsorbate binding energies and classical Lennard-Jones + Coulomb (LJ + C) potentials to calculate adsorbate interaction energies with liquid H2O molecules. This method is efficient, since it only requires one coarsely converged DFT calculation per adsorbate, while still incorporating the configurational disorder that is present in the liquid water structure. It also provides reasonable accuracy for calculating aqueous-phase reaction energies, with a MAE of 0.28 eV compared to the full DFT/MD method (which requires 21 DFT calculations per adsorbate). However, this method gives significantly different results for the absolute water–adsorbate interaction energies and aqueous-phase binding energies. Overall, the LSR/MD is viable for computing $E^{\text{vac}}_{\text{bind}}$, $E^{\text{vac}}_{\text{rxn}}$ and $E^{\text{aq}}_{\text{rxn}}$ with a good balance of accuracy and expense. Acknowledgement

3.7 Acknowledgments

This research was funded in part by the National Science Foundation (Award CBET-1438325), as well as the Chemical and Biomolecular Engineering Department at Clemson University. Simulations were performed on the Palmetto Supercomputer Cluster, which is maintained by the Cyberinfrastructure Technology Integration Group at Clemson University. We thank Dr. Steven Louis Pellizzeri, who worked as a postdoctoral associate in our group, for his help in applying the extended linear scaling relationship used in this work. We also thank undergraduate research assistants Grant Hummel and Andrew Bingham, who helped calculate energies for some of the adsorbates studied in this work. Grant and Andrew worked in our group as part of Clemson University's EURKEA! program, which is funded through the Clemson University Calhoun Honors College.

This work was adapted with permission from Xie, T., Sarupria, S., Getman, R. B. **(2017)**. A DFT and MD study of aqueous-phase dehydrogenation of glycerol on Pt (1 1 1): comparing chemical accuracy versus computational expense in different methods for calculating aqueous-phase system energies. *Molecular Simulation*, 43(5-6), 370-378. Copyright 2017 Taylor & Francis.

3.8 References

[1] Bin Liu and Jeffrey Greeley. "Decomposition pathways of glycerol via C-H, O-H, and C-C bond scission on Pt (111): A density functional theory study". *The Journal of Physical Chemistry C* 115.40 (2011), 19702–19709.

[2] Bin Liu and Jeffrey Greeley. "A density functional theory analysis of trends in glycerol decomposition on close-packed transition metal surfaces". *Physical Chemistry Chemical Physics* 15.17 (2013), 6475–6485.

[3] Y Chen, M Salciccioli, and DG Vlachos. "An efficient reaction pathway search method applied to the decomposition of glycerol on platinum". *The Journal of Physical Chemistry C* 115.38 (2011), 18707–18720.

[4] Omar Ali Abdelrahman, Andreas Heyden, and Jesse Q Bond. "Analysis of kinetics and reaction pathways in the aqueous-phase hydrogenation of levulinic acid to form γ-valerolactone over Ru/C". *ACS catalysis* 4.4 (2014), 1171–1181.

[5] Muhammad Faheem and Andreas Heyden. "Hybrid Quantum Mechanics/Molecular Mechanics Solvation Scheme for Computing Free Energies of Reactions at Metal-Water Interfaces". *Journal of chemical theory and computation* 10.8 (2014), 3354–3368.

[6] Ch Hartnig, J Grimminger, and E Spohr. "The role of water in the initial steps of methanol oxidation on Pt (2 1 1)". *Electrochimica acta* 52.6 (2007), 2236–2243.

[7] C Hartnig, J Grimminger, and E Spohr. "Adsorption of formic acid on Pt (1 1 1) in the presence of water". *Journal of Electroanalytical Chemistry* 607.1-2 (2007), 133–139.

[8] C. Hartnig and E. Spohr. "The role of water in the initial steps of methanol oxidation on Pt(111)". *Chemical Physics* 319.1-3 (2005), 185–191.

[9] Yasuharu Okamoto, Osamu Sugino, Yuji Mochizuki, Tamio Ikeshoji, and Yoshitada Morikawa. "Comparative study of dehydrogenation of methanol at Pt (1 1 1)/water and Pt (1 1 1)/vacuum interfaces". *Chemical physics letters* 377.1-2 (2003), 236–242.

[10] Hui-Fang Wang and Zhi-Pan Liu. "Formic acid oxidation at Pt/H2O interface from periodic DFT calculations integrated with a continuum solvation model". *The Journal of Physical Chemistry C* 113.40 (2009), 17502–17508.

[11] Cameron J Bodenschatz, Sapna Sarupria, and Rachel B Getman. "Molecular-Level Details about Liquid H2O Interactions with CO and Sugar Alcohol Adsorbates on Pt (111) Calculated Using Density Functional Theory and Molecular Dynamics". *The Journal of Physical Chemistry C* 119.24 (2015), 13642–13651.

[12] Nianjun Luo, Xianwen Fu, Fahai Cao, Tiancun Xiao, and Peter P Edwards. "Glycerol aqueous phase reforming for hydrogen generation over Pt catalyst–Effect of catalyst composition and reaction conditions". *Fuel* 87.17 (2008), 3483–3489.

[13] Jaime Gómez-Díaz and Núria López. "Mechanistic switch between oxidative (Andrussow) and nonoxidative (Degussa) formation of HCN on Pt (111) by density functional theory". *The journal of physical chemistry C* 115.13 (2011), 5667–5674.

[14] Aravind Asthagiri and Michael J Janik. *Computational catalysis*. Royal Society of Chemistry, 2013.

[15] Lars C Grabow, Felix Studt, Frank Abild-Pedersen, Vivien Petzold, Jesper Kleis, Thomas Bligaard, and Jens K Nørskov. "Descriptor-based analysis applied to HCN synthesis from NH3 and CH4". *Angewandte Chemie International Edition* 50.20 (2011), 4601–4605.

[16] Frank Abild-Pedersen, Jeff Greeley, Felix Studt, Jan Rossmeisl, TR Munter, Poul Georg Moses, Egill Skulason, Thomas Bligaard, and Jens Kehlet Nørskov. "Scaling properties of adsorption energies for hydrogen-containing molecules on transition-metal surfaces". *Physical review letters* 99.1 (2007), 016105.

[17] Jeffrey Greeley. "Theoretical heterogeneous catalysis: scaling relationships and computational catalyst design". *Annual review of chemical and biomolecular engineering* 7 (2016), 605–635.

[18] Glenn Jones, T Bligaard, Frank Abild-Pedersen, and Jens Kehlet Nørskov. "Using scaling relations to understand trends in the catalytic activity of transition metals". *Journal of Physics: Condensed Matter* 20.6 (2008), 064239.

[19] Isabela C Man et al. "Universality in oxygen evolution electrocatalysis on oxide surfaces". *ChemCatChem* 3.7 (2011), 1159–1165.

[20] Steve Plimpton. "Fast parallel algorithms for short-range molecular dynamics". *Journal of computational physics* 117.1 (1995), 1–19.

[21] Glenn J Martyna, Michael L Klein, and Mark Tuckerman. "Nosé–Hoover chains: the canonical ensemble via continuous dynamics". *The Journal of chemical physics* 97.4 (1992), 2635–2643.

[22] Guodong Wen, Yunpeng Xu, Huaijun Ma, Zhusheng Xu, and Zhijian Tian. "Production of hydrogen by aqueous-phase reforming of glycerol". *International Journal of Hydrogen Energy* 33.22 (2008), 6657–6666.

[23] David L King, Liang Zhang, Gordon Xia, Ayman M Karim, David J Heldebrant, Xianqin Wang, Tom Peterson, and Yong Wang. "Aqueous phase reforming of glycerol for hydrogen production over Pt–Re supported on carbon". *Applied Catalysis B: Environmental* 99.1 (2010), 206–213.

[24] Yunpeng Xu, Zhijian Tian, Guodong Wen, Zhusheng Xu, Wei Qu, and Liwu Lin. "Production of COx-free hydrogen by alkali enhanced hydrothermal catalytic reforming of biomass-derived alcohols". *Chemistry Letters* 35.2 (2006), 216–217.

[25] David D Hibbitts, Brett T Loveless, Matthew Neurock, and Enrique Iglesia. "Mechanistic role of water on the rate and selectivity of Fischer–Tropsch synthesis on ruthenium catalysts". *Angewandte Chemie International Edition* 52.47 (2013), 12273–12278.

[26] William L Jorgensen and Julian Tirado-Rives. "The OPLS [optimized potentials for liquid simulations] potential functions for proteins, energy minimizations for crystals of cyclic peptides and crambin". *Journal of the American Chemical Society* 110.6 (1988), 1657–1666.

[27] Daniel J Price and Charles L Brooks III. "A modified TIP3P water potential for simulation with Ewald summation". *The Journal of chemical physics* 121.20 (2004), 10096–10103.

[28] Hendrik Heinz, Tzu-Jen Lin, Ratan Kishore Mishra, and Fateme S Emami. "Thermodynamically consistent force fields for the assembly of inorganic, organic, and biological nanostructures: the INTERFACE force field". *Langmuir* 29.6 (2013), 1754–1765.

[29] HA Lorentz. "Ueber die Anwendung des Satzes vom Virial in der kinetischen Theorie der Gase [Application of the set of virial in kinetic theory of gases]." *Annalen der Physik* 248.1 (1881), 127–136.

[30] M Schoen and C Hoheisel. "The mutual diffusion coefficient D 12 in liquid model mixtures A molecular dynamics study based on Lennard-Jones (12-6) potentials: II. Lorentz-Berthelot mixtures". *Molecular Physics* 52.5 (1984), 1029–1042.

[31] Tianjun Xie, Sapna Sarupria, and Rachel B Getman. "A DFT and MD study of aqueous-phase dehydrogenation of glycerol on Pt (1 1 1): comparing chemical accuracy versus computational expense in different methods for calculating aqueous-phase system energies". *Molecular Simulation* 43.5-6 (2017), 370–378.

[32] Ahmed E Ismail, Gary S Grest, and Mark J Stevens. "Capillary waves at the liquid-vapor interface and the surface tension of water models". *arXiv preprint cond-mat/0605104* (2006).

[33] Giovanna Longhi, Alberto Ceselli, Sandro L Fornili, Sergio Abbate, Leopoldo Ceraulo, and Vincenzo Turco Liveri. "Molecular dynamics of electrosprayed water nanodroplets containing sodium bis (2-ethylhexyl) sulfosuccinate". *Journal of Mass Spectrometry* 48.4 (2013), 478–486.

[34] C. Clay, S. Haq, and A. Hodgson. "Hydrogen Bonding in Mixed OH + H_2O Overlayers on Pt(111)". *Phys. Rev. Lett.* 92 (4 Jan. 2004), 046102.

[35] Andre Clayborne, Hee-Joon Chun, Rees B. Rankin, and Jeff Greeley. "Elucidation of Pathways for NO Electroreduction on Pt(111) from First Principles". *Angewandte Chemie International Edition* 54.28 (2015), 8255–8258.

[36] P. Gambardella, Ž. Šljivan čanin, B. Hammer, M. Blanc, K. Kuhnke, and K. Kern. "Oxygen Dissociation at Pt Steps". *Phys. Rev. Lett.* 87 (5 July 2001), 056103.

[37] Jeff Greeley and Manos Mavrikakis. "A First-Principles Study of Methanol Decomposition on Pt(111)". *Journal of the American Chemical Society* 124.24 (2002), 7193–7201.

[38] Jeff Greeley and Manos Mavrikakis. "Competitive Paths for Methanol Decomposition on Pt(111)". *Journal of the American Chemical Society* 126.12 (2004), 3910–3919.

[39] Bin Liu and Jeffrey Greeley. "Decomposition Pathways of Glycerol via C–H, O–H, and C–C Bond Scission on Pt(111): A Density Functional Theory Study". *The Journal of Physical Chemistry C* 115.40 (2011), 19702–19709.

[40] S. Nie, Peter J. Feibelman, N. C. Bartelt, and K. Thürmer. "Pentagons and Heptagons in the First Water Layer on Pt(111)". *Phys. Rev. Lett.* 105 (2 July 2010), 026102.

[41] Peter Sutter, Jerzy T. Sadowski, and Eli Sutter. "Graphene on Pt(111): Growth and substrate interaction". *Phys. Rev. B* 80 (24 Dec. 2009), 245411.

[42] James D Pack and Hendrik J Monkhorst. "" Special points for Brillouin-zone integrations"—a reply". *Physical Review B* 16.4 (1977), 1748.

[43] Shengguang Wang et al. "Universal transition state scaling relations for (de) hydrogenation over transition metals". *Physical Chemistry Chemical Physics* 13.46 (2011), 20760–20765.

[44] Shengguang Wang et al. "Universal brønsted-evans-polanyi relations for C-C, C-O, C-N, N-O, N-N, and O-O dissociation reactions". *Catalysis letters* 141.3 (2011), 370–373.

Chapter 4

Insights into the Roles of Water on the Aqueous Phase Reforming of Glycerol

4.1 Abstract

Aqueous phase reforming (APR) of sugar alcohol molecules derived from biomass, e.g., $C_xH_{(2x+2)}O_x$ (aq) + $x H_2O \rightarrow x CO_2$ (g) + $(2x+1)H_2$ (g), creates hydrogen gas sustainably, making it an important component of future bio-refineries; however, problems with the cost, activity, and selectivity of present precious metal based catalysts impede its broader adoption. Ideally, new catalysts would be designed to optimize activity and selectivity; however, a comprehensive understanding of the APR mechanism is lacking. This is complicated by the fact that the primary biomass-derived sugar alcohols are large molecules (meaning that their reaction networks are large) and because of the presence of liquid water. Water influences catalytic phenomena in multiple ways, including altering the thermodynamics of catalytic surface species and participating in catalytic reactions. Understanding the mechanism of APR requires understanding these various effects; however, computational strategies based solely on density functional theory (DFT) are computationally prohibitive for such large and complicated reaction networks. In this work, we investigate the mechanism of APR reactions in the context of glycerol reforming. To calculate the reaction network, we combine

DFT calculations, force-field molecular dynamics (MD) simulations, linear scaling relations (LSRs), transition state scaling (TSS) relationships, and data from the literature into a microkinetic model. The microkinetic model is run under vacuum and aqueous phases in order to learn about the roles of water molecules on the mechanism of glycerol APR. We identify four such roles: providing surface hydroxyl groups, which promote oxidation of surface CO formed in glycerol decomposition; promoting C-H scissions; promoting O-H scissions; and inhibiting the thermodynamics of decarbonylation of C3 intermediates.

4.2 Introduction

A goal within the catalyst research community is to solve this problem, which first requires improving our understanding of the APR catalytic mechanism. From a big-picture standpoint, the mechanism of APR involves three branches: dehydrogenation (R-H* + * → R* + H*, where * are catalyst sites), decarbonylation (R-CO* + * → R* + CO*), and water-gas shift (WGS; CO* + H_2O → * + CO_2 + H_2). However, elucidating the individual steps in the different branches is not straightforward, for multiple reasons, including the large sizes and complex structures of APR feed molecules (which result in large reaction networks and numerous possible catalytic intermediates) and the aqueous reaction conditions themselves.

We use a combination of density functional theory (DFT) calculations, force field molecular dynamics (MD) simulations, and microkinetic modeling to learn about the mechanism of glycerol APR under aqueous conditions. Building on the literature, we construct and employ linear correlations for estimating the energies of catalytic C3 species in order to reduce the computational cost associated with studying such a large reaction network. Specifically, we use linear scaling relationships (LSRs) [1–9] built in our prior work [9] to estimate the energies of catalytic reactant and product species. Further, we build transition state scaling (TSS) relationships [10–17] to estimate the energies of transition states involved in dehydrogenation and decarbonylation reactions involving C3 catalytic intermediates. We additionally construct TSS relationships for hydrogenolysis reactions (R-OH* + * → R* + OH*) involving C3 species. To investigate the ability of H_2O to participate in the catalysis, we additionally simulate water-mediated dehydrogenation (R-H* + n' $1H_2O$* → R* + $H_{(2n+1)}O_n$*) and hydrogenolysis steps (R-OH* + $H_{(2n+1)}O_n$* → R* + $(n+1)$ H_2O*). We combine all of our calculated energies with energies obtained from the literature [18–21] for reactions involving C2 and C1 intermediates as well as WGS reactions into a microkinetic model, which we use to probe the mechanism of glycerol APR. Our results indicate that H_2O molecules play at least four roles in the APR of glycerol: supplying OH* for the WGS reaction, promoting C-H bond scissions, promoting O-H bond scissions, and inhibiting decarbonylation of C3 catalytic species.

4.3 Methods

We calculate energies for this manuscript in two ways: explicitly and using linear relationships. In explicit calculations, catalytic species are modeled under structures of liquid water

using a multi-timescale method that combines DFT calculations and MD simulations. This method is discussed below and elaborated in the Supporting Information Section 5 of our published work [22], which is available electronically at https://pubs.rsc.org/en/content/articlelanding/2018/re/c8re00267c/. In this chapter, unless otherwise stated, all Supporting Information occurrences refer to this electronic source.

4.3.1 Simulation Supercell

Pt(111) surfaces were modeled using three-layer 4 Pt × 4 Pt orthogonal slabs (i.e., with symmetries of $p\left(2\sqrt{2} \times 7/4\sqrt{2}\right) - R90°$) in periodic supercells. The slabs were constructed by cleaving a (111) surface from the calculated structure of bulk Pt. Catalytic intermediates and transition states were optimized on the topmost Pt layers only, and only one catalytic intermediate or transition state was included per slab, yielding a total coverage of 1/16 monolayer (ML, where 1 ML = 1 catalytic intermediate or transition state per surface Pt atom). The orthogonal supercells had dimensions of $a = 11.22$ Å and $b = 9.72$ Å (shown in Figure 4.1). A total of 36 H_2O molecules were added to the supercell in the space above the Pt(111) surfaces. It has been shown by López that rigidity in the liquid H_2O structure can influence reactivity [23]. To ensure the liquid H_2O is simulated at the correct density for the reaction conditions, i.e., $T = 500$ K and $P = 50$ bar, the c dimension of the supercell was determined using MD simulations performed in the NPT ensemble. This procedure is elaborated upon in Section 2 of the Supporting Information and in other publications from our group [24, 25]. Briefly, after the H_2O molecules are added to the supercell, a 5 ns MD simulation is performed in the NPT ensemble at a target temperature and pressure of 500 K and 50 bar, which are maintained by the Nosé–Hoover thermostat and barostat. The first 2 ns of the NPT simulation are used for system equilibration and the remaining 3 ns are used to determine the average value of the c dimension. The value of the c dimension that yields the proper H_2O density for these supercells is 20.18 Å. The resulting liquid water density is 0.857 g/cm^3, which is similar to the density of saturated liquid water at 500 K as calculated with TIP4P/2005 (0.850 g/cm^3 [26]) and as observed experimentally (0.844 g/cm^3 [27] and 0.837 g/cm^3 [**Yoshida2005**]).

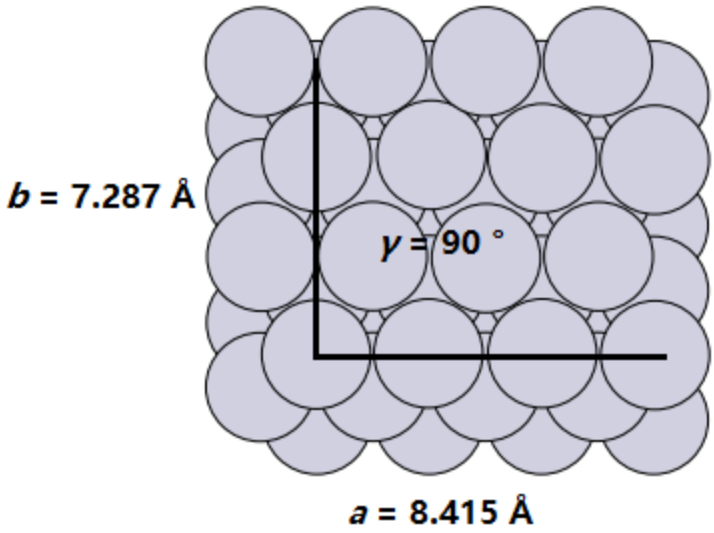

Figure 4.1: Top view of $p(2\sqrt{2} \times 7\frac{\sqrt{2}}{4} - R90°)$ Pt (111) catalyst model (unit cell). The light grey circles denote Pt atoms of the surface. Information about a, b, and γ is labeled in the graph.

4.3.2 Water Configurations from Molecular Dynamics Simulations

Molecular Dynamics (MD) simulations were conducted using the Large-scale Atomic/Molecular Massively Parallel Simulator (LAMMPS) [28]. Interactions of water molecules with catalytic intermediates and the Pt surface were calculated using Lennard Jones + Coulomb (LJ+C) potentials. LJ parameters for adsorbates, H_2O molecules, and Pt atoms were taken from the optimized potentials for liquid simulations (OPLS) [29], TIP4P/2005 [30], and INTERFACE force fields [31], respectively. Cross terms for the LJ interactions were computed using Lorentz–Berthelot mixing rules [32, 33]. Atomic partial charges used in the Coulomb potentials for the Pt atoms and adsorbates were calculated from density functional theory results using the density derived electrostatic and chemical (DDEC) package [34–39]. All LJ+C parameters are tabulated in the Supporting Information Section 3.

Configurations of liquid H_2O molecules around the catalytic species were generated in the NVT ensemble. The target temperature was set to 500 K, similar to the conditions employed experimentally [40–43]. The temperature was controlled by the Nosé–Hoover thermostat [44]. MD simulations were performed for 5 ns with 1 fs timesteps, where the first 2 ns were used for system equilibration and the final 3 ns were used for configurational sampling.

4.3.3 Energies of Catalytic Species from DFT

DFT calculations were performed based on information provided in Chapter 2 section 5. All transition state structures were confirmed by their vibrational frequencies. The final structures of all catalytic species calculated in this work are illustrated in Supporting Information Section 6. Additionally, their coordinates have been uploaded to our group's GitHub page [45]. VASP INCAR settings are provided in the Supporting Information Section 1.

4.3.4 Linear Scaling and Transition State Scaling Relationships

Since the reaction network for catalytic APR is rather large, we additionally estimated energies of catalytic species using linear correlations, as has been done by others working in this field [46]. Binding energies of C3 intermediates (reactant and product species) were estimated using an extended linear scaling relationship (LSR) based on the energies of their fragments [18, 47–55], as in our prior work [9]. In our prior work, we derived linear correlations to calculate the energies of intermediates with chemical formulas of $CH_{y'}O$–$CH_{y''}O$–$CH_{y'''}O$ as functions of the binding energies of their $CH_{y'}O$, $CH_{y''}O$, and $CH_{y'''}O$ fragments (the subscripts y', y'', and y''' denote different levels of saturation of the carbon atoms). Energies of transition states were estimated using transition state scaling (TSS) relationships [10–17], which are linear functions of the energies of the product species (commonly referred to as final state (FS) species in the literature). In this work, we input both DFT calculated FS energies and FS energies that were calculated using LSRs to the TSS relationships. How we combined LSRs and TSS relationships is demonstrated in the Supporting Information Section 4.

4.3.5 Reaction and Activation Energy Calculations

Reaction energies for vacuum phase reactions $E_{\text{rxn}}^{\text{vac}}$ were calculated using standard formulas. For example, the reaction energy for adsorbed glycerol $C_3H_8O_3$* dehydrogenation to $C_3H_7O_3$*, i.e., $C_3H_8O_3$* + * → $C_3H_7O_3$* + H* (where * indicates a catalytic site and a *'ed species indicates a species adsorbed on a Pt(111) catalytic site) is

$$E_{\text{rxn}}^{\text{vac}} = E(C_3H_7O_3^*) + E(H^*) - E(C_3H_8O_3^*) - E(^*) \tag{4.1}$$

where $E(C_3H_7O_3{}^*)$, $E(H^*)$, and $E(C_3H_8O_3{}^*)$ are the electronic energies of $C_3H_7O_3{}^*$, H^*, and glycerol $C_3H_8O_3{}^*$, and $E(^*)$ is the electronic energy of the clean Pt(111) surface. The energies of the carbon-containing species can be obtained using DFT calculations or LSRs.

We define the reaction energy in the aqueous phase as being equal to the reaction energy in vacuum phase plus the change in the water-catalytic species interaction energy, as in our prior work [9], i.e.,

$$E_{\text{rxn}}^{\text{aq}} = E_{\text{rxn}}^{\text{vac}} + \Delta E_{\text{int}} \tag{4.2}$$

For any catalytic species, the water-catalytic species interaction energy E_{int} is defined as the total interaction between the water structure and the catalytic species [56]. For example, the interaction energy for glycerol is

$$E_{\text{int}}(C_3H_8O_3{}^*) = E(H_2O + C_3H_8O_3{}^*) - E(H_2O + {}^*) - E(C_3H_8O_3{}^*) + E(^*) \tag{4.3}$$

E_{int} are reported as averages over 10 different configurations of water for catalytic species involved in non-water-mediated steps ± the calculated standard deviation. E_{int} for catalytic species involved in water-mediated steps are calculated using a single configuration of H_2O molecules.

ΔE_{int} is the change in interaction energy going from reactants to products. For example, in the reaction $C_3H_8O_3{}^*$ dehydrogenation to $C_3H_7O_3{}^*$, ΔE_{int} is

$$\Delta E_{\text{int}} = E_{\text{int}}(C_3H_7O_3{}^*) + E_{\text{int}}(H^*) - E_{\text{int}}(C_3H_8O_3{}^*) - E_{\text{int}}(^*) \tag{4.4}$$

We found that $E_{\text{int}}(H^*)$ is equal to 0. Further, $E_{\text{int}}(^*)$, i.e., E_{int} of the clean Pt(111) surface, is set to 0 by definition. Therefore, ΔE_{int} in this case can be calculated as $\Delta E_{\text{int}} = E_{\text{int}}(C_3H_7O_3{}^*) - E_{\text{int}}(C_3H_8O_3{}^*)$. When values of ΔE_{int} include ± values, they are the propagated uncertainties, which are determined using standard error propagation rules [57].

Activation energies are calculated analogously. For example, the activation energy for the glycerol dehydrogenation reaction, $C_3H_8O_3{}^* + {}^* \rightarrow TS^* \rightarrow C_3H_7O_3{}^* + H^*$ under vacuum is

$$E_{\text{act}}^{\text{vac}} = E(TS^*) - E(C_3H_8O_3{}^*) \tag{4.5}$$

where TS stands for transition state. Under aqueous phase, the activation energy is

$$E_{\text{act}}^{\text{aq}} = E_{\text{act}}^{\text{vac}} + \Delta E_{\text{int}} \tag{4.6}$$

where ΔE_{int} is the change of the interaction energy from the reactant to the transition state, i.e.,

$$\Delta E_{\text{int}} = E_{\text{int}}(\text{TS}^*) - E_{\text{int}}(\text{C}_3\text{H}_8\text{O}_3{}^*) \tag{4.7}$$

The above equations were used to calculate the activation energies in aqueous phase using DFT data. Since our TSS relationships are derived using transition states under aqueous phase, they already include the water-catalytic species interaction energy, and hence, the activation energy is simply

$$E_{\text{act}} = E(\text{TS}^*) - E(\text{IS}^*) \tag{4.8}$$

where IS stands for initial state and in this work is the reactant species.

4.3.6 Microkinetic Modeling

Microkinetic modeling was performed with the MKMCXX package [58]. Adsorption rate constants were calculated from the Hertz-Knudsen equation [59–61],

$$k_{\text{ads}} = \frac{yPA}{\sqrt{2\pi m k_B T}} \tag{4.9}$$

where y is the mole fraction of either the gas phase or aqueous phase species, P is the total pressure, A is the surface area of the adsorption site, m is molecular mass, k_{B} is the Boltzmann constant, and T is the temperature. Here, we set the initial mole fraction of glycerol to 0.1 for both the vacuum and aqueous phase microkinetic models. In the vacuum phase model, glycerol is supplied with a balance of inerts, and in the aqueous phase model, glycerol is supplied with a balance of H_2O (water to glycerol ratio of 9). The total pressure in both models is set to 1 atm. This procedure has been published previously by Heyden's group [19] for both gas and liquid phase microkinetic models. Essentially, it computes the adsorption rate constant from gas phase collision theory. To our knowledge, there is no well-tested theory for simulating the kinetics of chemisorption from liquid phase onto solid catalyst surfaces. Because of this, and also since our intent in this manuscript is

to learn about the roles of H_2O molecules on surface reactions involved in the reforming of glycerol, we have treated the adsorption in our gas and aqueous phase models similarly. That said, we stress that there is some uncertainty embedded into the thermodynamic and kinetic quantities pertaining to adsorption that are reported in this manuscript.

Desorption rate constants were calculated as [60–62],

$$k = \frac{k_B T^3}{h^3} \frac{A(2\pi m k_B)}{\sigma \theta_{rot}} \exp\left(\frac{-E_{des}}{k_B T}\right) \tag{4.10}$$

where h is the Plank's constant, σ is the symmetry number, θ is the rotational temperature of the species, and E_{des} is the desorption energy. Details about σ and θ are provided in the Supporting Information Section 7. In this formalism, adsorption and desorption proceed through a mobile precursor, which is a fluid phase species that has been trapped on the catalyst surface. The mobile precursor has two translational degrees of freedom (while the fluid phase species has three) and three rotational degrees of freedom, which are all lost when the species ultimately binds to the catalyst surface. Desorption energies for all species considered in this work are endothermic (i.e., their adsorption energies are exothermic).

Rate constants for surface reactions were calculated with the Arrhenius equation,

$$k = A \exp\left(\frac{-E_{act}}{k_B T}\right) \tag{4.11}$$

where A is the pre-exponential factor. Pre-exponential factors for surface reactions were set to 10^{13} s^{-1}.

Reaction energies and activation barriers that were input to the microkinetic model were obtained as follows. Energetics of reactions involving C3 species were calculated in this work using a combination of DFT data, LSRs, and TSS relationships, as described above. Modeling the APR of glycerol also requires energies of reactions involving C2 and C1 species and also water-gas shift. We obtained energies of these reactions from the literature, using references from Bligaard [18], Heyden [19], Vlachos [20], and Schneider [21]. During the review stage of this manuscript, we became aware of a recently published database [63], which houses structures and energies of species involved in catalytic APR over Pt [46]. An alternative approach would have been to use information from the database for the reactions involving C2 and C1 species and water-gas shift. All reaction

energetics that were used in the microkinetic models presented in this manuscript are tabulated in the Supporting Information Section 7.

The microkinetic models reported in this work employed single site models for simplicity. We note that due to the large sizes of some of the adsorbates, as well as the fact that on supported catalysts, interfacial sites are likely important to the catalysis [64], this is an approximation.

The temperature in our microkinetic models was set to 500 K. The MKM solver was iterated for 10^8 seconds to ensure convergence, and the absolute and relevant tolerances were both set to 10^{-8} mol/s.

4.4 Results

4.4.1 Role of H_2O on the Energetics of Reactions Involving $C_3H_yO_3$ Species

Reaction energies and activation barriers for non-water-mediated reactions are summarized in Table 4.1. Comparing the calculated reaction energies for vacuum and aqueous phases, the differences for the dehydrogenation steps are slight, indicating little influence of water. In contrast, reaction energies for decarbonylation steps are more endothermic in aqueous phase than in vacuum. Further, the energies of hydrogenolysis reactions 15, 16, and 18 are more exothermic in aqueous phase than in vacuum. To investigate the influence of water on the calculated activation barriers, Figure 4.2 plots the activation energies for the three types of reactions in both vacuum and aqueous phases. As shown in Figure 4.2a, the activation barriers for dehydrogenation reactions are for the most part similar in aqueous and vacuum phases. The activation barriers in the aqueous phase for decarbonylation reactions are larger than those under vacuum, with the exception of the activation barrier for Reaction 13 (CO-COH-COH* + * $\rightarrow$ COH-COH* + CO*), suggesting that there is a kinetic penalty for removing a carbonyl group from a $C_3H_yO_3$ catalytic intermediate under aqueous phase until a certain degree of dehydrogenation has occurred. Similarly, there is a kinetic penalty for removing a hydroxyl group from a C3 catalytic species under aqueous phase until a certain degree of dehydrogenation has occurred.

TSS relationships derived for non-water-mediated dehydrogenation, decarbonylation, and hydrogenation steps under vacuum and aqueous phases are shown in Figure 4.3. Comparing the TSS relationships derived for vacuum phase to those derived for aqueous phase, the dehydrogenation trends are only minorly different, whereas the decarbonylation and hydrogenolysis trends are

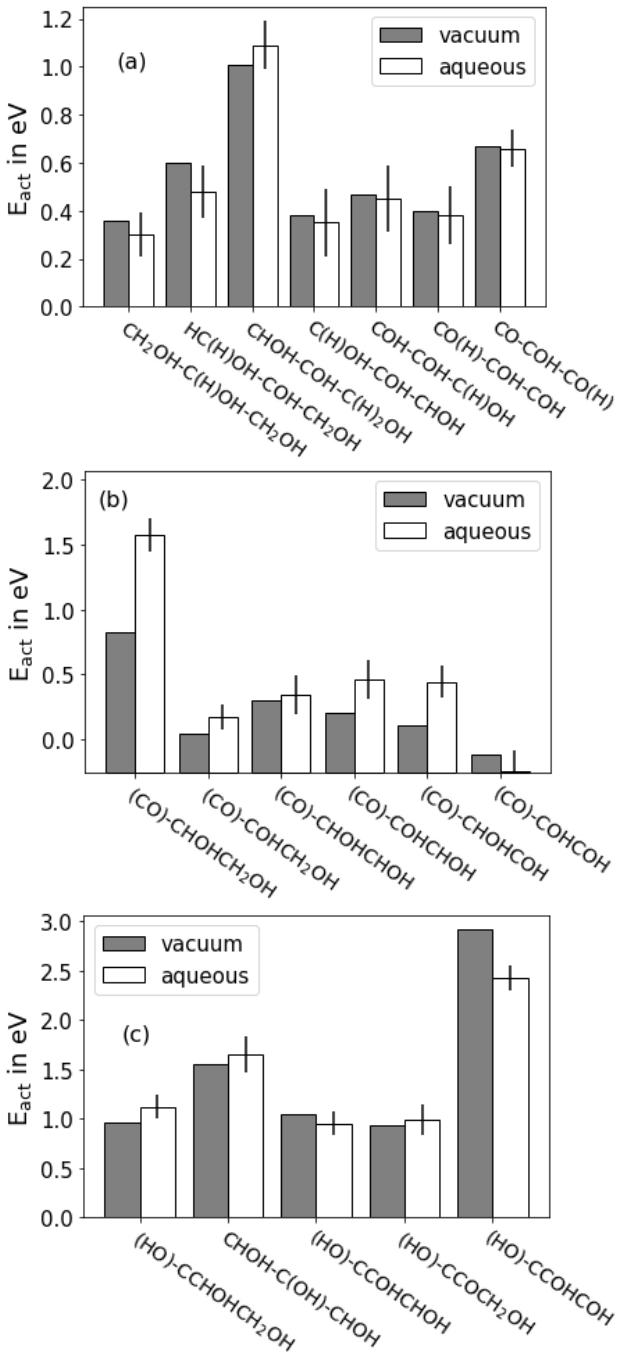

Figure 4.2: Comparison of activation energies calculated in vacuum (gray) and aqueous phases (white) for the non-water-mediated dehydrogenation (a), decarbonylation (b), and hydrogenolysis steps (c) calculated in this work. Bar labels are the transition states species with the species that is being removed in parentheses. Error bars denote the standard deviations of the average energies (caused by configurational fluctuations of the liquid H_2O molecules).

Table 4.1: Reaction energies (E_{rxn}) and activation energies (E_{act}) of non-water-mediated dehydrogenation (1 - 7), decarbonylation (8 - 13), and hydrogenolysis steps (14 - 18) under vacuum (vac) and aqueous phases (aq). Reaction numbers of the analogous water-mediated reactions are given in parentheses where applicable, the results for which are given in Table 4.2. All values are in unit of eV.

Number	Reaction	$E_{\text{rxn}}^{\text{vac}}$	$E_{\text{rxn}}^{\text{aq}}$	$E_{\text{act}}^{\text{vac}}$	$E_{\text{act}}^{\text{aq}}$
1	$CH_2OH\text{-}CHOH\text{-}CH_2OH^* + * \rightarrow CH_2OH\text{-}COH\text{-}CH_2OH^* + H^*$	-0.45	-0.44±0.10	0.36	0.30±0.10
2 (19)	$CH_2OH\text{-}COH\text{-}CH_2OH^* + * \rightarrow CHOH\text{-}COH\text{-}CH_2OH^* + H^*$	-0.35	-0.39±0.14	0.60	0.48±0.11
3 (20)	$CHOH\text{-}COH\text{-}CH_2OH^* + * \rightarrow CHOH\text{-}COH\text{-}CHOH^* + H^*$	-0.08	-0.10±0.10	1.01	1.09±0.10
4 (21)	$CHOH\text{-}COH\text{-}CHOH^* + * \rightarrow COH\text{-}COH\text{-}CHOH^* + H^*$	-0.19	-0.11±0.11	0.38	0.35±0.14
5 (22)	$COH\text{-}COH\text{-}CHOH^* + * \rightarrow COH\text{-}COH\text{-}COH^* + H^*$	-0.33	-0.38±0.12	0.47	0.45±0.14
6 (23)	$COH\text{-}COH\text{-}COH^* + * \rightarrow CO\text{-}COH\text{-}COH^* + H^*$	0.20	0.24±0.10	0.40	0.38±0.12
7 (24)	$CO\text{-}COH\text{-}COH^* + * \rightarrow CO\text{-}COH\text{-}CO^* + H^*$	0.26	0.26±0.09	0.67	0.66±0.08
8	$CO\text{-}CHOH\text{-}CH_2OH^* + * \rightarrow CHOH\text{-}CH_2OH^* + CO^*$	-0.94	-0.52±0.17	1.08	0.90±0.18
9	$CO\text{-}COH\text{-}CH_2OH^* + * \rightarrow COH\text{-}CH_2OH^* + CO^*$	-0.61	-0.34±0.16	0.30	0.43±0.10
10	$CO\text{-}CHOH\text{-}CHOH^* + * \rightarrow CHOH\text{-}CHOH^* + CO^*$	-1.17	-1.03±0.14	0.56	0.60±0.14
11	$CO\text{-}COH\text{-}CHOH^* + * \rightarrow COH\text{-}CHOH^* + CO^*$	-0.61	-0.55±0.10	0.46	0.72±0.12
12	$CO\text{-}CHOH\text{-}COH^* + * \rightarrow CHOH\text{-}COH^* + CO^*$	-0.34	0.15±0.12	0.37	0.70±0.15
13	$CO\text{-}COH\text{-}COH^* + * \rightarrow COH\text{-}COH^* + CO^*$	-0.96	-0.81±0.13	0.14	0.01±0.16
14 (25)	$COH\text{-}CHOH\text{-}CH_2OH^* + * \rightarrow C\text{-}CHOH\text{-}CH_2OH^* + OH^*$	0.30	0.37±0.10	0.96	1.12±0.12
15 (26)	$CHOH\text{-}COH\text{-}CHOH^* + * \rightarrow CHOH\text{-}C\text{-}CHOH^* + OH^*$	0.68	0.49±0.14	1.55	1.65±0.18
16 (27)	$COH\text{-}COH\text{-}CHOH^* + * \rightarrow C\text{-}COH\text{-}CHOH^* + OH^*$	0.40	0.20±0.13	1.05	0.94±0.12
17 (28)	$COH\text{-}CO\text{-}CH_2OH^* + * \rightarrow C\text{-}CO\text{-}CH_2OH^* + OH^*$	0.72	0.81±0.11	0.93	0.99±0.16
18 (29)	$COH\text{-}COH\text{-}COH^* + * \rightarrow C\text{-}COH\text{-}COH^* + OH^*$	2.53	2.07±0.15	2.92	2.43±0.13

significantly different. This means that the E_{int} for the transition states involved in dehydrogenation reactions are similar to the E_{int} of the product species, whereas the E_{int} for the transition states involved in decarbonylation and hydrogenolysis reactions are different than the E_{int} of the product species for those reactions. Thus, water interacts with the reactants, transition states, and products involved in dehydrogenation of C3 species similarly, whereas water interacts with the reactants, transition states, and products involved in decarbonylation and hydrogenolysis of C3 species differently. Specifically, the water environment stabilizes the reactants and transition states of the decarbonylation reactions more so than the products, and the water environment stabilizes reactant and product species of hydrogenolysis reactions more so than the transition states.

4.4.2 Role of H_2O on the Mechanisms of Reactions Involving $C_3H_yO_3$ Species

Mechanistically, H_2O molecules can mediate catalytic dehydrogenation reactions, forming $H_{2n+1}O_n$ complexes at either the transition state or as the product [65–73], and $H_{2n+1}O_n$ complexes can act as reactants in hydrogenolysis steps [74]. We calculated the energetics of 15 such water-mediated reactions, and they are presented in Table 4.2. The reaction energies for the water-

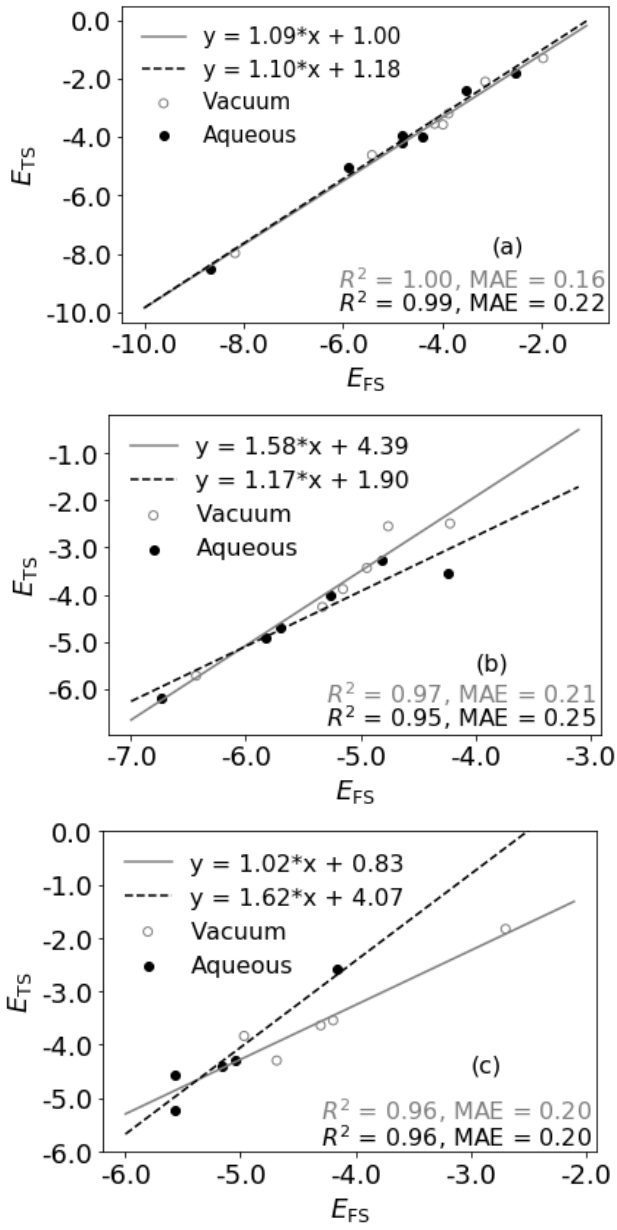

Figure 4.3: Regression training data (points) and linear TSS relationships (lines) for non-water-mediated dehydrogenation (a), decarbonylation (b), and hydrogenolysis steps (c) calculated under vacuum (solid lines and unfilled points) and aqueous phases (dotted lines and filled points). MAE stands for mean absolute error. Units on all values are eV.

Table 4.2: Reaction energies (E_{rxn}) and activation energies (E_{act}) of water-mediated dehydrogenation (19 - 25) and hydrogenolysis steps (25 - 29). Reaction energetics were calculated using one and/or two water molecules in the reactants. Numbers in parentheses are for the non-mediated analogues from Table 1. All values are in units of eV

Number	Reaction	E_{rxn}	E_{act}
19 (2)	$CH_2OH\text{-}COH\text{-}CH_2OH^* + H_2O^* \rightarrow CHOH\text{-}COH\text{-}CH_2OH^* + H_3O^*$	0.25	1.42
19 (2)	$CH_2OH\text{-}COH\text{-}CH_2OH^* + 2H_2O^* \rightarrow CHOH\text{-}COH\text{-}CH_2OH^* + H_5O_2^* + *$	0.26	1.18
20 (3)	$CHOH\text{-}COH\text{-}CH_2OH^* + H_2O^* \rightarrow CHOH\text{-}COH\text{-}CHOH^* + H_3O^*$	0.27	1.67
20 (3)	$CHOH\text{-}COH\text{-}CH_2OH^* + 2H_2O^* \rightarrow CHOH\text{-}COH\text{-}CHOH^* + H_5O_2^* + *$	0.26	1.75
21 (4)	$CHOH\text{-}COH\text{-}CHOH^* + H_2O^* \rightarrow COH\text{-}COH\text{-}CHOH^* + H_3O^*$	0.29	1.14
21 (4)	$CHOH\text{-}COH\text{-}CHOH^* + 2H_2O^* \rightarrow COH\text{-}COH\text{-}CHOH^* + H_5O_2^* + *$	0.37	1.20
22 (5)	$COH\text{-}COH\text{-}CHOH^* + H_2O^* \rightarrow COH\text{-}COH\text{-}COH^* + H_3O^*$	0.07	0.87
22 (5)	$COH\text{-}COH\text{-}CHOH^* + 2H_2O^* \rightarrow COH\text{-}COH\text{-}COH^* + H_5O_2^* + *$	-0.15	0.57
23 (6)	$COH\text{-}COH\text{-}COH^* + 2H_2O^* \rightarrow CO\text{-}COH\text{-}COH^* + H_5O_2^* + *$	-0.39	0.01
24 (7)	$CO\text{-}COH\text{-}COH^* + 2H_2O^* \rightarrow CO\text{-}COH\text{-}CO^* + H_5O_2^* + *$	-0.19	0.02
25 (14)	$COH\text{-}CHOH\text{-}CH_2OH^* + H_3O^* + * \rightarrow C\text{-}CHOH\text{-}CH_2OH^* + 2H_2O^*$	0.30	0.23
26 (15)	$CHOH\text{-}COH\text{-}CHOH^* + H_3O^* + * \rightarrow CHOH\text{-}C\text{-}CHOH^* + 2H_2O^*$	0.62	0.64
27 (16)	$COH\text{-}COH\text{-}CHOH^* + H_3O^* + * \rightarrow C\text{-}COH\text{-}CHOH^* + 2H_2O^*$	0.38	0.31
28 (17)	$COH\text{-}CO\text{-}CH_2OH^* + H_3O^* + * \rightarrow C\text{-}CO\text{-}CH_2OH^* + 2H_2O^*$	0.70	0.28
29 (18)	$COH\text{-}COH\text{-}COH^* + H_3O^* + * \rightarrow C\text{-}COH\text{-}COH^* + 2H_2O^*$	2.03	1.51

mediated C-H dehydrogenation steps are in general more endothermic than their non-water-mediated analogues, whereas the reaction energies for water-mediated O-H dehydrogenation steps are more exothermic than their non-water-mediated analogues, going from being endothermic to exothermic in both cases that we explicitly calculated (Reactions 23 and 24, i.e., $COH\text{-}COH\text{-}COH^* + H_2O^* \rightarrow CO\text{-}COH\text{-}COH^* + H_3O^*$ and $CO\text{-}COH\text{-}COH^* + H_2O^* \rightarrow CO\text{-}COH\text{-}CO^* + H_3O^*$). The reaction energies for water-mediated hydrogenolysis steps are for the most part similar to their non-water-mediated analogues, with the exception of Reaction 27 ($COH\text{-}COH\text{-}CHOH^* + H_2O^* \rightarrow C\text{-}COH\text{-}CHOH^* + H_3O^*$), which is 0.18 eV more exothermic.

Activation energies for water-mediated versus non-water-mediated reactions are shown in Figure 4.4. The activation energies for the water-mediated C–H scissions are all larger than their non-water-mediated analogues. In fact, with the exception of Reaction 22, the activation barriers for the water-mediated C-H scissions are all greater than 1 eV. The barrier for Reaction 22, i.e., COH–COH–CHOH* reacting to COH–COH–COH*, is 0.57 eV, compared to 0.45 eV for its non-water-mediated analogue. The barriers for water-mediated O-H scissions (Reactions 23 and 24) are essentially equal to 0, which is lower than their non-water-mediated analogues. Barriers ≈ 0 are expected for proton transfer reactions in liquid H_2O [75]. The activation energies for water-mediated hydrogenolysis reactions are lower than their non-mediated analogues, suggesting that hydrogenolysis steps could occur via water mediated routes, if sufficient concentration of $H_{2n+1}O_n$

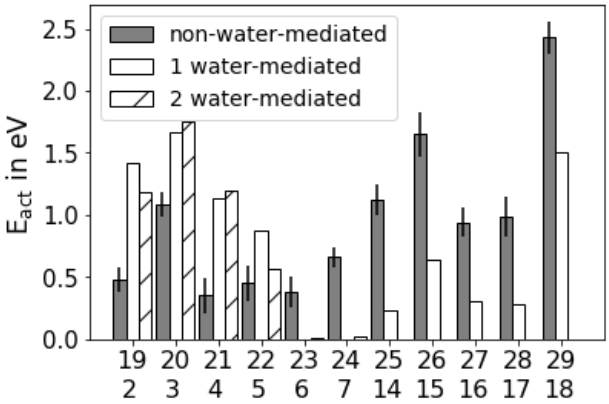

Figure 4.4: Comparison for activation energies for non-water-mediated (gray bars) reactions to their water-mediated (white and hashed bars) analogues. White bars indicate participation of 1 H_2O molecule, and hashed bars indicate participation of 2 H_2O molecules. Sets of bars are labeled by their reaction numbers. The first row of numbers are the reaction numbers for the water-mediated reactions (from Table 4.2), and the second row of numbers are the reaction numbers for their non-water-mediated analogues (from Table 4.1).

species is available.

4.4.3 Microkinetic Modeling Results

The reaction energetics calculated in this work, along with the TSS relationships that were derived, as well as reaction energetics available in the literature [18–21] allow for microkinetic modeling of catalytic glycerol reforming. We ran microkinetic models under both vacuum and aqueous phases. In vacuum phase, the initial water concentration was set to 0, so the water-gas shift reaction did not occur. Hence, the main products were H_2 and CO. In aqueous phase, the water supplied OH* to the surface, which reacted with CO* through water-gas shift steps [21]. The primary products in the aqueous phase model were H_2, CO_2, and CH_2OH–CH_2OH (ethylene glycol). Assuming the gas phase products are H_2 and CO_2, the mole fraction of H_2 in the gas phase was 65.6%, which agrees well with the experimental value of 64.8% observed by Cortright et al. [76]. Further, the selectivity to H_2 was 89.1%, compared to the experimental value of 85.0% reported by Davda et al. [77]. 32.8% of the carbon was converted to CO_2, in agreement with the experimentally observed value of 29.7% reported by Cortright et al. [76]. Reactions that contributed to the observed phenomena in both models along with their net rates are tabulated in Supporting Information Section 8. Under vacuum, glycerol decomposition proceeds through dehydrogenation steps until reaching the CO–COH–COH* intermediate, which then proceeds through a decarbonylation step to form

COH–COH*. This intermediate is then further dehydrogenated to CO–CO*, which is finally decomposed into 2 CO*. The pathway in aqueous phase is similar, with dehydrogenation occurring until reaching the CO–COH–COH* intermediate. However, water-mediated reactions become competitive with non-water-mediated reactions for both O–H and C–H scissions. Specifically, the rates of water-mediated COH–COH–CHOH* dehydrogenation to COH–COH–COH*, COH–COH–COH* dehydrogenation to CO–COH–COH*, and CO–COH–COH* dehydrogenation to CO–COH–CO* reactions are competitive with their non-water-mediate analogues. The CO–COH–COH* intermediate that is formed from water-mediated COH–COH–COH* dehydrogenation is decarbonylated to COH–COH*, which is dehydrogenated to CO–CO* and then decomposed to 2 CO*, like under vacuum. Similarly, the CO–COH–CO* that is formed from water-mediated CO–COH–COH* dehydrogenation is dehydrogenated to CO–CO–CO* and then decomposed into 3 CO*. In both microkinetic models, carbon atoms must be significantly dehydrogenated before the rates of O–H scissions start to become appreciable. Hydrogenolysis steps do not participate in the dominant reaction pathways for either the vacuum or aqueous-phase models. However, we note that our microkinetic model of the aqueous phase reforming of glycerol was carried out at neutral pH, which resulted in insufficient concentration of $H_{2n+1}O_n$ species to carry out water-mediated hydrogenolysis to any remarkable degree, despite that the rate constants for these reactions are larger than the non-water-mediated analogues.

4.5 Discussion

From the results of the last section, H_2O plays at least four roles in the aqueous phase reforming of glycerol. One, H_2O molecules dissociate on the catalyst surface, supplying the OH* and H* that are needed to promote oxidation of CO* and production of H_2. Two, H_2O molecules promote C–H scission. We find that the activation barrier for water-mediated COH–COH–CHOH* dehydrogenation to COH–COH–COH* is within 0.12 eV (although still higher) of its non-water-mediated analogue. The reaction energy of the water-mediated reaction is less exothermic than its non-water-mediated analogue by more than 0.2 eV; however, owing to the large concentration of H_2O, the rate of the water-mediated COH–COH–CHOH* dehydrogenation to COH–COH–COH* is competitive with its non-water-mediated analogue. Three, water molecules mediate O–H scission. The activation barriers of H_2O-mediated O–H scissions are ≈ 0 and their reaction energies

are exothermic. Thus the rates of water-mediated O-H scissions are higher than their non-water-mediated analogues, by up to five orders of magnitude. Four, water inhibits the thermodynamics of catalytic decarbonylation. Specifically, in both microkinetic models, decarbonylation occurs at at the CO-COH-COH* species. The activation energy for the decarbonylation step to COH–COH* is quite low in both vacuum and aqueous phases (0.14 eV in vacuum versus 0.01 eV in aqueous phase); however, the reaction energy is 0.17 eV more endothermic in aqueous phase than it is in vacuum. This is due to the loss of hydrophillicity that occurs over the course of the reaction. Specifically, E_{int} for CO–COH–COH* is more negative than for the combination of COH–COH* and CO* (with E_{int} for CO* being essentially equal to zero [56]). In fact, comparing the reaction energies in vacuum versus aqueous phase for all of the decarbonylation reactions calculated in this work, there is always an energy penalty associated, ranging from 0.06 eV (CO–COH–CHOH* $\rightarrow$ COH–CHOH*) to 0.49 eV (CO–CHOH–COH* $\rightarrow$ CHOH–COH*).

4.6 Conclusions

In this work, we have used DFT calculations, MD simulations, linear scaling relationships, transition state scaling relationships, and data from the literature to construct microkinetic models of catalytic glycerol reforming under vacuum and aqueous phases. We have specifically calculated steps in the pathways for dehydrogenation, decarbonlyation, and hydrogenolysis of C3 species, and we have included steps where H_2O molecules and $H_{2(n+1)}O_n$ species explicitly participate in the reactions. Results from our microkinetic models identified four roles of water on the catalytic mechanism of aqueous phase reforming of glycerol: supplying OH* needed in water-gas shift to oxidize CO*, promoting C-H scissions, promoting O-H scissions, and thermodynamically inhibiting decarbonylation of C3 species. Our results also suggest that protons in solution could mediate catalytic hydrogenolysis reactions if the reaction were run under sufficient pH. (In practice, hydrogenolysis reactions are likely promoted by acid sites on the catalyst or its support [78].) In this manuscript, we have attempted to present only the “big-picture" conclusions. This is because, even with the inclusion of an explicit liquid water environment and an extensive network of catalytic reactions, limitations in our models prevent us from providing a comprehensive mechanism of glycerol APR. For example, methods to properly model adsorption and desorption at a liquid water/catalyst interface and models that properly incorporate the participation of interfacial sites are needed to more

fully understand the mechanism of glycerol APR. We are presently working on addressing both issues.

4.7 Acknowledgments

This research was funded by the National Science Foundation through award number (CBET-1438325). Fellowship support for Cameron J. Bodenschatz through NASA Training Grant (NNX14AN43H) is gratefully acknowledged. Simulations were performed on the Palmetto Supercomputer Cluster, which is maintained by the Cyberinfrastructure Technology Integration Group at Clemson University. We thank Dr. Steven Louis Pellizzeri, who worked as a postdoctoral associate in our group, for his help in running the MKMCXX package.

This work was adapted with permission from Xie, T., Bodenschatz, C. J., and Getman, R. B. **(2019)**. Insights into the roles of water on the aqueous phase reforming of glycerol. *Reaction Chemistry Engineering*, 4(2), 383-392. Copyright 2019 Royal Society of Chemistry.

4.8 References

[1] Jaime Gómez-Díaz and Núria López. "Mechanistic switch between oxidative (Andrussow) and nonoxidative (Degussa) formation of HCN on Pt (111) by density functional theory". *The journal of physical chemistry C* 115.13 (2011), 5667–5674.

[2] Omar Ali Abdelrahman, Andreas Heyden, and Jesse Q Bond. "Analysis of kinetics and reaction pathways in the aqueous-phase hydrogenation of levulinic acid to form γ-valerolactone over Ru/C". *ACS catalysis* 4.4 (2014), 1171–1181.

[3] Aravind Asthagiri and Michael J Janik. *Computational catalysis*. Royal Society of Chemistry, 2013.

[4] Lars C Grabow, Felix Studt, Frank Abild-Pedersen, Vivien Petzold, Jesper Kleis, Thomas Bligaard, and Jens K Nørskov. "Descriptor-based analysis applied to HCN synthesis from NH3 and CH4". *Angewandte Chemie International Edition* 50.20 (2011), 4601–4605.

[5] Frank Abild-Pedersen, Jeff Greeley, Felix Studt, Jan Rossmeisl, TR Munter, Poul Georg Moses, Egill Skulason, Thomas Bligaard, and Jens Kehlet Nørskov. "Scaling properties of adsorption energies for hydrogen-containing molecules on transition-metal surfaces". *Physical review letters* 99.1 (2007), 016105.

[6] Jeffrey Greeley. "Theoretical heterogeneous catalysis: scaling relationships and computational catalyst design". *Annual review of chemical and biomolecular engineering* 7 (2016), 605–635.

[7] Glenn Jones, T Bligaard, Frank Abild-Pedersen, and Jens Kehlet Nørskov. "Using scaling relations to understand trends in the catalytic activity of transition metals". *Journal of Physics: Condensed Matter* 20.6 (2008), 064239.

[8] Isabela C Man et al. "Universality in oxygen evolution electrocatalysis on oxide surfaces". *ChemCatChem* 3.7 (2011), 1159–1165.

[9] Tianjun Xie, Sapna Sarupria, and Rachel B Getman. "A DFT and MD study of aqueous-phase dehydrogenation of glycerol on Pt (1 1 1): comparing chemical accuracy versus computational expense in different methods for calculating aqueous-phase system energies". *Molecular Simulation* 43.5-6 (2017), 370–378.

[10] J.K. Nørskov et al. "Universality in Heterogeneous Catalysis". *Journal of Catalysis* 209.2 (2002), 275–278.

[11] P. Ferrin, D. Simonetti, S. Kandoi, E. Kunkes, J. A. Dumesic, J. K. Nørskov, and M. Mavrikakis. "Modeling Ethanol Decomposition on Transition Metals: A Combined Application of Scaling and Brønsted-Evans-Polanyi Relations". *Journal of the American Chemical Society* 131.16 (2009), 5809–5815.

[12] Bin Liu and Jeffrey Greeley. "Decomposition Pathways of Glycerol via C–H, O–H, and C–C Bond Scission on Pt(111): A Density Functional Theory Study". *The Journal of Physical Chemistry C* 115.40 (2011), 19702–19709.

[13] Bin Liu, Lei Cheng, Larry Curtiss, and Jeffrey Greeley. "Effects of van der Waals density functional corrections on trends in furfural adsorption and hydrogenation on close-packed transition metal surfaces". *Surface Science* 622 (2014), 51–59.

[14] Bin Liu, Mingxia Zhou, Maria K. Y. Chan, and Jeffrey P. Greeley. "Understanding Polyol Decomposition on Bimetallic Pt–Mo Catalysts—A DFT Study of Glycerol". *ACS Catalysis* 5.8 (2015), 4942–4950.

[15] Y. Chen, M. Salciccioli, and D. G. Vlachos. "An Efficient Reaction Pathway Search Method Applied to the Decomposition of Glycerol on Platinum". *The Journal of Physical Chemistry C* 115.38 (2011), 18707–18720.

[16] R Alcala. "DFT studies for cleavage of C-C bond and C-O bonds in surface species derived from ethanol on Pt(111)". *Journal of Catalysis* 218.1 (2003), 178–190.

[17] David Loffreda, Françoise Delbecq, Fabienne Vigné, and Philippe Sautet. "Fast Prediction of Selectivity in Heterogeneous Catalysis from Extended Brønsted-Evans-Polanyi Relations: A Theoretical Insight". *Angewandte Chemie* 121.47 (2009), 9140–9142.

[18] S. Wang et al. "Universal transition state scaling relations for (de)hydrogenation over transition metals". *Physical Chemistry Chemical Physics* 13.46 (2011), 20760.

[19] Muhammad Faheem, Mohammad Saleheen, Jianmin Lu, and Andreas Heyden. "Ethylene glycol reforming on Pt(111): First-principles microkinetic modeling in vapor and aqueous phases". *Catalysis Science and Technology* 6.23 (2016), 8242–8256.

[20] Ying Chen and Dionisios G. Vlachos. "Hydrogenation of Ethylene and Dehydrogenation and Hydrogenolysis of Ethane on Pt (111) and Pt (211): A Density Functional Theory Study". *Journal of Physical Chemistry C* 114.11 (2010), 4973–4982.

[21] John P Clay, Jeffrey P Greeley, Fabio H Ribeiro, W Nicholas Delgass, and William F Schneider. "DFT comparison of intrinsic WGS kinetics over Pd and Pt". *Journal of Catalysis* 320 (2014), 106–117.

[22] Tianjun Xie, Cameron J Bodenschatz, and Rachel B Getman. "Insights into the roles of water on the aqueous phase reforming of glycerol". *Reaction Chemistry & Engineering* 4.2 (2019), 383–392.

[23] Luca Bellarosa, Rodrigo Garcı'a-Muelas, Guillem Revilla-López, and Núria López. "Diversity at the Water–Metal Interface: Metal, Water Thickness, and Confinement Effects". *ACS central science* 2.2 (2016), 109–116.

[24] Cameron J. Bodenschatz, Xiaohong Zhang, Tianjun Xie, Sapna Sarupria, and Rachel B. Getman. "Multi-Timescale Model for Calculating Configurations of Liquid Water Molecules in Aqueous Phase Heterogeneous Catalysis". *Journal of Visualized Experiments* (2018), submitted.

[25] Xiaohong Zhang, Ryan S DeFever, Sapna Sarupria, and Rachel B Getman. "Free Energies of Catalytic Species Adsorbed to Pt (111) Surfaces under Liquid Solvent Calculated Using Classical and Quantum Approaches". *Journal of chemical information and modeling* 59.5 (2019), 2190–2198.

[26] C Vega, JLF Abascal, and I Nezbeda. "Vapor-liquid equilibria from the triple point up to the critical point for the new generation of TIP4P-like models: TIP4P/Ew, TIP4P/2005, and TIP4P/ice". *The Journal of Chemical Physics* 125.3 (2006), 034503.

[27] John Brodholt and Bernard Wood. "Simulations of the structure and thermodynamic properties of water at high pressures and temperatures". *Journal of Geophysical Research: Solid Earth* 98.B1 (1993), 519–536.

[28] Steve Plimpton. "Fast parallel algorithms for short-range molecular dynamics". *Journal of computational physics* 117.1 (1995), 1–19.

[29] William L. Jorgensen and Julian Tirado-Rives. "The OPLS [optimized potentials for liquid simulations] potential functions for proteins, energy minimizations for crystals of cyclic peptides and crambin". *Journal of the American Chemical Society* 110.6 (1988), 1657–1666.

[30] Jose LF Abascal and Carlos Vega. "A general purpose model for the condensed phases of water: TIP4P/2005". *The Journal of Chemical Physics* 123.23 (2005), 234505.

[31] Hendrik Heinz, Tzu-Jen Lin, Ratan Kishore Mishra, and Fateme S. Emami. "Thermodynamically Consistent Force Fields for the Assembly of Inorganic, Organic, and Biological Nanostructures: The INTERFACE Force Field". *Langmuir* 29.6 (2013), 1754–1765.

[32] H. A. Lorentz. "Nachtrag zu der Abhandlung: Ueber die Anwendung des Satzes vom Virial in der kinetischen Theorie der Gase [Application of the set of virial in kinetic theory of gases]". *Annalen der Physik* 248.4 (1881), 660–661.

[33] M. Schoen and C. Hoheisel. "The mutual diffusion coefficientD12in liquid model mixtures A molecular dynamics study based on Lennard-Jones (12-6) potentials". *Molecular Physics* 52.5 (Oct. 1984), 1029–1042.

[34] Thomas A. Manz and David S. Sholl. "Chemically Meaningful Atomic Charges That Reproduce the Electrostatic Potential in Periodic and Nonperiodic Materials". *Journal of Chemical Theory and Computation* 6.8 (Oct. 2010), 2455–2468.

[35] Thomas A. Manz and David S. Sholl. "Methods for Computing Accurate Atomic Spin Moments for Collinear and Noncollinear Magnetism in Periodic and Nonperiodic Materials". *Journal of Chemical Theory and Computation* 7.12 (2011), 4146–4164.

[36] Thomas A. Manz and David S. Sholl. "Improved Atoms-in-Molecule Charge Partitioning Functional for Simultaneously Reproducing the Electrostatic Potential and Chemical States in Periodic and Nonperiodic Materials". *Journal of Chemical Theory and Computation* 8.8 (2012), 2844–2867.

[37] Thomas A. Manz and Nidia Gabaldon Limas. "Introducing DDEC6 atomic population analysis: part 1. Charge partitioning theory and methodology". *RSC Advances* 6.53 (2016), 47771–47801.

[38] Nidia Gabaldon Limas and Thomas A. Manz. "Introducing DDEC6 atomic population analysis: part 2. Computed results for a wide range of periodic and nonperiodic materials". *RSC Advances* 6.51 (2016), 45727–45747.

[39] Thomas A. Manz. "Introducing DDEC6 atomic population analysis: part 3. Comprehensive method to compute bond orders". *RSC Adv.* 7.72 (2017), 45552–45581.

[40] G Wen, Y Xu, H Ma, Z Xu, and Z Tian. "Production of hydrogen by aqueous-phase reforming of glycerol". *International Journal of Hydrogen Energy* 33.22 (2008), 6657–6666.

[41] David D. Hibbitts, Brett T. Loveless, Matthew Neurock, and Enrique Iglesia. "Mechanistic Role of Water on the Rate and Selectivity of Fischer-Tropsch Synthesis on Ruthenium Catalysts". *Angewandte Chemie* 125.47 (Feb. 2013), 12499–12504.

[42] David L. King, Liang Zhang, Gordon Xia, Ayman M. Karim, David J. Heldebrant, Xianqin Wang, Tom Peterson, and Yong Wang. "Aqueous phase reforming of glycerol for hydrogen production over Pt–Re supported on carbon". *Applied Catalysis B: Environmental* 99.1-2 (2010), 206–213.

[43] Yunpeng Xu, Zhijian Tian, Guodong Wen, Zhusheng Xu, Wei Qu, and Liwu Lin. "Production of COx-free Hydrogen by Alkali Enhanced Hydrothermal Catalytic Reforming of Biomass-derived Alcohols". *Chemistry Letters* 35.2 (2006), 216–217.

[44] Glenn J. Martyna, Michael L. Klein, and Mark Tuckerman. "Nosé–Hoover chains: The canonical ensemble via continuous dynamics". *The Journal of Chemical Physics* 97.4 (1992), 2635–2643.

[45] *https://github.com/getman-research-group/Geomtry-files-for-Insights-into-the-Roles-of-Water-on-the-Aqueous-Phase-Reforming-of-Glycerol.* `https://github.com/getman-research-group/Geomtry-files-for-Insights-into-the-Roles-of-Water-on-the-Aqueous-Phase-Reforming-of-Glycerol`. (accessed Dec, 2018).

[46] Qiang Li, Rodrigo Garcı'a-Muelas, and Núria López. "Microkinetics of alcohol reforming for H 2 production from a FAIR density functional theory database". *Nature communications* 9.1 (2018), 526.

[47] F. Abild-Pedersen, J. Greeley, F. Studt, J. Rossmeisl, T. R. Munter, P. G. Moses, E. Skúlason, T. Bligaard, and J. K. Nørskov. "Scaling Properties of Adsorption Energies for Hydrogen-Containing Molecules on Transition-Metal Surfaces". *Phys. Rev. Lett.* 99 (1 July 2007), 016105.

[48] Jaime Gómez-Díaz, Crisa Vargas-Fuentes, and Núria López. "C-N coupling on transition metal surfaces: A density functional theory study". *The Journal of Chemical Physics* 135.12 (2011), 124707.

[49] Jaime Gómez-Díaz and Núria López. "Mechanistic Switch between Oxidative (Andrussow) and Nonoxidative (Degussa) Formation of HCN on Pt(111) by Density Functional Theory". *The Journal of Physical Chemistry C* 115.13 (2011), 5667–5674.

[50] Glenn Jones, T Bligaard, Frank Abild-Pedersen, and Jens Kehlet Nørskov. "Using scaling relations to understand trends in the catalytic activity of transition metals". *Journal of Physics: Condensed Matter* 20.6 (2008), 064239.

[51] Isabela C Man et al. "Universality in oxygen evolution electrocatalysis on oxide surfaces". *ChemCatChem* 3.7 (2011), 1159–1165.

[52] Aravind Asthagiri and Michael J Janik. *Computational catalysis.* 14. Royal Society of Chemistry, 2013, 1–58.

[53] Aravind Asthagiri and Michael J Janik, editors. *Computational Catalysis*. Catalysis Series. The Royal Society of Chemistry, 2014, P001–266.

[54] Jeffrey Greeley. "Theoretical Heterogeneous Catalysis: Scaling Relationships and Computational Catalyst Design". *Annual Review of Chemical and Biomolecular Engineering* 7.1 (2016). PMID: 27088666, 605–635.

[55] Rodrigo Garcı'a-Muelas, Marcos Rellán-Piñeiro, Qiang Li, and Núria López. "Developments in the atomistic modelling of catalytic processes for the production of platform chemicals from biomass". *ChemCatChem* ().

[56] Cameron J. Bodenschatz, Sapna Sarupria, and Rachel B. Getman. "Molecular-Level Details about Liquid H2O Interactions with CO and Sugar Alcohol Adsorbates on Pt(111) Calculated Using Density Functional Theory and Molecular Dynamics". *The Journal of Physical Chemistry C* 120.1 (2015), 801–801.

[57] Philip R Bevington, D Keith Robinson, J Morris Blair, A John Mallinckrodt, and Susan McKay. "Data reduction and error analysis for the physical sciences". *Computers in Physics* 7.4 (1993), 415–416.

[58] Ivo A. W. Filot, Rutger A. van Santen, and Emiel J. M. Hensen. "The Optimally Performing Fischer–Tropsch Catalyst". *Angewandte Chemie International Edition* 53.47 (2014), 12746–12750.

[59] Kurt W Kolasinski. *Surface science: foundations of catalysis and nanoscience*. John Wiley & Sons, 2012, 203–203.

[60] Ivo AW Filot, Robin JP Broos, Jeaphianne PM van Rijn, Gerardus JHA van Heugten, Rutger A van Santen, and Emiel JM Hensen. "First-principles-based microkinetics simulations of synthesis gas conversion on a stepped rhodium surface". *ACS Catalysis* 5.9 (2015), 5453–5467.

[61] Ivo AW Filot, Bart Zijlstra, Robin JP Broos, Wei Chen, Robert Pestman, and Emiel JM Hensen. "Kinetic aspects of chain growth in Fischer–Tropsch synthesis". *Faraday discussions* 197 (2017), 153–164.

[62] A. P. J. Jansen. "Modeling Surface Reactions I". *An Introduction to Kinetic Monte Carlo Simulations of Surface Reactions*. Berlin, Heidelberg: Springer Berlin Heidelberg, 2012, 121–153.

[63] M Álvarez-Moreno, Cornelis De Graaf, Nuria Lopez, Feliu Maseras, Josep M Poblet, and Carles Bo. "Managing the computational chemistry big data problem: the ioChem-BD platform". *Journal of chemical information and modeling* 55.1 (2014), 95–103.

[64] Matteo Cargnello, Vicky VT Doan-Nguyen, Thomas R Gordon, Rosa E Diaz, Eric A Stach, Raymond J Gorte, Paolo Fornasiero, and Christopher B Murray. "Control of metal nanocrystal size reveals metal-support interface role for ceria catalysts". *Science* 341.6147 (2013), 771–773.

[65] Matthew Neurock, Sally A. Wasileski, and Donghai Mei. "From first principles to catalytic performance: tracking molecular transformations". *Chemical Engineering Science* 59.22 (2004). ISCRE18, 4703–4714.

[66] Xiaowa Nie, Monica R Esopi, Michael J Janik, and Aravind Asthagiri. "Selectivity of CO2 reduction on copper electrodes: the role of the kinetics of elementary steps". *Angewandte Chemie* 125.9 (2013), 2519–2522.

[67] Yufeng Zhao and Thomas Gennett. "Water-mediated cooperative migration of chemisorbed hydrogen on graphene". *Physical review letters* 112.7 (2014), 076101.

[68] Tao Cheng, Hai Xiao, and William A. Goddard. "Reaction Mechanisms for the Electrochemical Reduction of CO2 to CO and Formate on the Cu(100) Surface at 298 K from Quantum Mechanics Free Energy Calculations with Explicit Water". *Journal of the American Chemical Society* 138.42 (2016), 13802–13805.

[69] Thomas Loerting and Klaus R. Liedl. "Water-Mediated Proton Transfer: A Mechanistic Investigation on the Example of the Hydration of Sulfur Oxides". *The Journal of Physical Chemistry A* 105.21 (2001), 5137–5145.

[70] Xiaowa Nie, Wenjia Luo, Michael J. Janik, and Aravind Asthagiri. "Reaction mechanisms of CO2 electrochemical reduction on Cu(111) determined with density functional theory". *Journal of Catalysis* 312 (2014), 108–122.

[71] C. Hartnig and E. Spohr. "The role of water in the initial steps of methanol oxidation on Pt(111)". *Chemical Physics* 319.1 (2005). Molecular Charge Transfer in Condensed Media - from Physics and Chemistry to Biology and Nanoengineering in honour of Alexander M. Kuznetsov on his 65th birthday, 185–191.

[72] Shaonan Dong, Wenjing Shi, Jing Zhang, and Shuping Bi. "DFT Studies on the Water-Assisted Synergistic Proton Dissociation Mechanism for the Spontaneous Hydrolysis Reaction of Al3+ in Aqueous Solution". *ACS Earth and Space Chemistry* 2.3 (2018), 269–277.

[73] Líney Árnadóttir, Eric M. Stuve, and Hannes Jónsson. "The effect of coadsorbed water on the stability, configuration and interconversion of formyl (HCO) and hydroxymethylidyne (COH) on platinum (111)". *Chemical Physics Letters* 541 (2012), 32–38.

[74] Nils Spang, Matthias Müller, and Magnus R Buchner. "The phosphonium ion [Cy3PCHCl2]+: synthesis and properties". *European Journal of Inorganic Chemistry* 2018.32 (2018), 3652–3659.

[75] Dominik Marx. "Proton Transfer 200 Years after von Grotthuss: Insights from Ab Initio Simulations". *ChemPhysChem* 7.9 (2006), 1848–1870.

[76] R. D. Cortright, R. R. Davda, and J. A. Dumesic. "Hydrogen from catalytic reforming of biomass-derived hydrocarbons in liquid water." *Nature* 418.49 (2002), 964–967.

[77] Kerstin Lehnert and Peter Claus. "Influence of Pt particle size and support type on the aqueous-phase reforming of glycerol". *Catalysis Communications* 9.15 (2008), 2543–2546.

[78] Andreas Martin, Udo Armbruster, Inaki Gandarias, and Pedro Luis Arias. "Glycerol hydrogenolysis into propanediols using in situ generated hydrogen–A critical review". *European journal of lipid science and technology* 115.1 (2013), 9–27.

Chapter 5

Computational Modeling of Methanol Decomposition on Pt Catalyst Supported by Alumina

5.1 Abstract

In this chapter, a more advanced catalyst model than pure Pt metal is introduced as the active Pt catalyst component is modeled as a tetrahedral Pt_4 cluster, and it is supported on a γ alumina surface. This surface is constructed in a way in order to simulate a more realistic surface rather than the model that only captures the properties of pure Pt metal. Most importantly, the model is more representative for edge sites and sites at the metal support interface. By doing so, roles of alumina support in methanol decomposition can be examined. This advanced model is capable of simulating the type of binding site formed by under-coordinated metal atoms at the Pt/support interface, which is named as "edge" site. Results show distinctive thermodynamics phenomena of reactions and reaction intermediates on the edge sites with respect to the "terrace" sites. Studying those phenomena can shed light upon how to investigate and determine the most thermodynamically favored reaction pathway and most stable binding, i.e. it gives information of how likely a species is to stay on one type of the binding sites, or it is susceptible to diffuse onto a different type of binding site. The reaction pathways, that cover all chemical species in methanol decomposition reaction

network, which is based on reaction thermodynamics are presented. Reaction pathways on Pt(1 1 1) terrace model and the supported Pt_4/Al_2O_3 are included and compared. Results pertaining to vibrational IR spectra are also presented and put in comparison with our collaborator's experimental outcome. Our calculated results can agree with previous published findings and conclusions by our collaborator.

5.2 Introduction

In order to devise better catalysts for reactions related to aqueous phase reforming of sugars and polyols, we use computational methods to model current working catalyst systems. Methanol is chosen as the starting model compound. Despite methanol molecule is a small and simple molecule, its significant in the industry for example from syngas applications, it is important to have good understandings of the mechanism on the the currently working catalysts and related surface reactions. Unfortunately, the complexity of surface reactions, along with the number of possible intermediates and competitive branches of reaction pathways, has limited the amount of mechanistic insight that can be obtained [1]. On Pt, for example, several researchers suggested that a direct reaction path of methanol oxidation is possible [2–6]. However, if the catalyst composition changes, the reaction mechanism can differ drastically, with limited mechanistic information available [3]. One complication is simply understanding the natures of the catalytically active sites. For example, in APR carried out on supported catalysts, questions still remain unanswered as whether certain reactions prefer proceeding on sites on the metal catalyst components (terrace) or sites at the metal/support interface (edge). Previous study showed that the rate of CO formation from dehydrogenation of glycerol is limited by the lack of available Pt active sites and CO_B (bridge bound to Pt) is preferentially more active over CO_L (linear bound to Pt) in water–gas shift at room temperature [7].

In this chapter, we present results of computational studies aimed at learning the active sites for reaction steps in the dehydrogenation of methanol over alumina-supported platinum catalysts. Specifically, we calculated relative energies of intermediates in the methanol dehydrogenation pathway on Pt(1 1 1) "terrace site" models and Pt_4/Al_2O_3 "edge site" models(sites illustrated in Figure 5.1), in order to provide insight of which sites different species along the methanol dehydrogenation pathway prefer. Further, we compute infrared vibrational spectra for different intermediates and compare them with our experimental collaborator's results. We find our techniques can reproduce

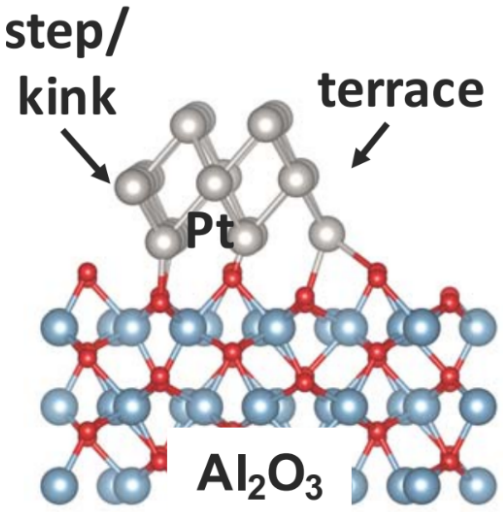

Figure 5.1: Illustration of two types of available catalyst sites available on a supported Pt catalyst particle, terrace and edge (kink) sites near the interface of Pt and Al_2O_3 [8]. Silver: Al, Red: O, White: Pt. Courtesy of Dr. Steven Pellizzeri, Department of Chemistry and Biochemistry, Eastern Illinois University.

signature peaks and help interpret the experimental spectra data well. On top of that, our calculated energies can reveal reactions thermodynamics and arrive at useful understandings, such as preferred binding on certain active sites, preferred reaction pathways, and dominant species.

5.3 Methods

5.3.1 Simulation Supercell

In this section, the catalyst model was constructed by loading Pt particles on a γ-Al_2O_3 surface. This model is intended to simulate realistic catalyst systems that have been studied experimentally [9, 10]. Including the support is a key step towards more realistic catalyst system modeling because it not only addresses the active component (here Pt particles) but also takes the support which is commonly hard to model and ignored into consideration. Studies based on this model can now yield insights of the support effects, which can include stabilization in adsorption from dispersion effects and participation of Lewis acid sites [11]. Additionally, this supported catalyst model can help elucidate initial steps of reactions which are suggested occur on edge sites instead of directly on Pt terrace sites [8]. The γ-Al_2O_3 surface was created by cleaving from the structure of

bulk Al_2O_3, which was taken from the literature [12, 13]. Specifically, we created a 2×2×2 cell with the (1 0 0) facet exposed of γ -Al_2O_3. The monoclinic surface has the planar lattice parameters a = b = 10.325 Åand an angle of 55.3 °. On the topmost layer of the γ-Al_2O_3 surface, a tetrahedral-like Pt_4 island was stabilized, the bond distance of Pt-Pt is 2.85 Å. The top view of the model can be view at Fig. 5.2. This Pt_4 cluster choice was made based on information from the literature, which indicates that a Pt_4 cluster is large enough to avoid significant influence from small size effects. Previously, Chao et al. evaluated Pt islands of size up to 13, reported flat lying bi-planar clusters with strong interaction energies are stabilized on the dehydrated (1 0 0) surface [14]. Cheng et al. investigated electron density of Pt clusters of size from Pt_1-Pt_{12} on the Al_2O_3 support and found that the clusters can be stably anchored on the surface at the oxygen sites [15]. Majumder et al. investigated reactions in the oxygen reduction reaction on alumina supported Pt clusters with sizes ranging from Pt_1 to Pt_{10}. Results indicated that there is limited difference in reaction enthalpies between a Pt_4 cluster and a Pt_{10} cluster [16]. Further, Christophe et al. investigated electronic electronic properties of small nanometer-sized Pt_n clusters ($n \leq 13$). Results showed that partial charges of the Pt atoms stabilize after Pt reaches a size of 4 [17], further suggesting that a size of 4 is sufficient to avoid small size effects. Combining these conclusions and the consideration of the computational expense, the Pt_4 metal cluster model is chosen in this thesis. This is in line with our goal that is to create a sufficiently realistic model to reflect our experimental collaborator's catalyst and to simulate methanol decomposition on various active sites with reasonable chemical accuracy and computational expense.

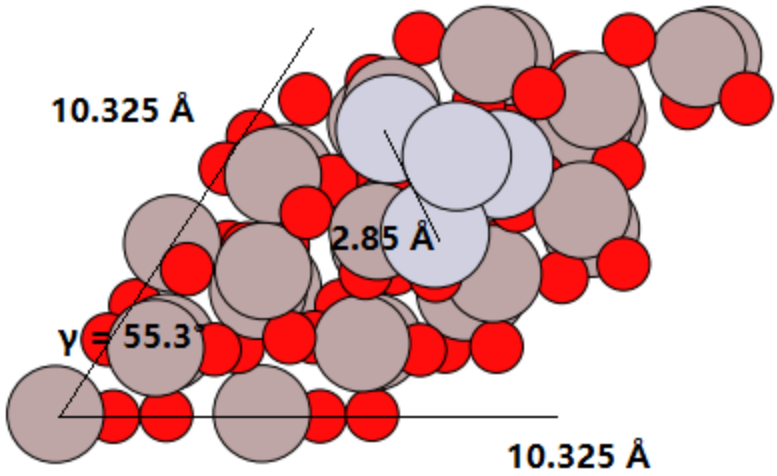

Figure 5.2: Top view of γ-Al_2O_3 supported Pt_4 catalyst model (unit cell). Light grey circles denote Pt atoms in the Pt_4 cluster. Information about a, b, and γ and inter-Pt distance is labeled in the graph. Color key: Grey: Pt, Red: O, Light brown: Al.

5.3.2 Energy Calculation

5.3.2.1 Binding Energy Calculation

The binding energy ΔE_b, is an energy of interest that describes the binding strength of a certain adsorbate, defined in Eqn. 5.1

$$\Delta E_b(\mathrm{CH}_x\mathrm{O}) = E(\mathrm{CH}_x\mathrm{O}*) - E(*) - \left(E_g(\mathrm{CH_3OH}) - \frac{4-x}{4}E_g(\mathrm{H_2})\right) \tag{5.1}$$

Where the energy terms on the right hand side of the equation refer to the electronic energies of the system containing the adsorbate, the clean catalyst model, and the gas phase energy of the adsorbate before adsorption. Note that binding energies are defined with respect to CH_3OH (g) and $H_22(g).The gas phase energy \mathrm{E_g}(\mathrm{CH}_x\mathrm{O})$ is calculated by relating the electronic energy referring to the full gas molecule [18, 19]. For example,

$$E_g(\mathrm{CH}_x\mathrm{O}) = E_g(\mathrm{CH_3OH}) - \frac{4-x}{4}E_g(\mathrm{H_2}) \tag{5.2}$$

Where the $E_{\mathrm{g}}(\mathrm{CH_3OH})$ and $E_{\mathrm{g}}(\mathrm{H_2})$ terms on the right hand side are the electronic energies of the the gas CH_3OH molecule and of the gas H_2 molecule.

5.3.2.2 Diffusion Energy Calculation

Diffusion of adsorbates is an important phenomena that needs attention. Our advanced model enables the investigation relative binding strengths in an attempt to learn whether diffusion between terrace sites and edge could be important. Energetics of these two types of sites shall be considered dynamically, that is to say, besides seeking for the lowest energy wells exist in the potential energy in terms of the binding energy ΔE_{b}, the diffusion heat shall also play a role in determining whether a species is stable on the surface, or on a particular type of binding site. In our diffusable model, reaction intermediates are allowed to diffuse between edge sites and terrace sites. Take adsorbate CO* as an example, the chemical equation that describes CO diffuses from the terrace site to the edge site can be written as in Eqn. 5.3 and the diffusion heat of this process can be defined as in Eqn. 5.4. Upon this consideration, the most stable binding will be chosen on the binding site that exhibits the most exothermicity, meanwhile counting the diffusion heat towards or against the binding energy.

$$\mathrm{CO} *_{\mathrm{terrace}} + *_{\mathrm{edge}} \rightarrow \mathrm{CO} *_{\mathrm{edge}} + *_{\mathrm{terrace}} \tag{5.3}$$

In which $\mathrm{CO}^*_{\mathrm{terrace}}$ and $\mathrm{CO}^*_{\mathrm{edge}}$ correspond to CO adsorbate on terrace site of Pt(1 1 1) surface and CO adsorbate on edge site of Pt_4/Al_2O_3 surface, respectively. And $*_{\mathrm{terrace}}$ and $*_{\mathrm{edge}}$ correspond to unoccupied terrace site of Pt(1 1 1) and unoccupied edge site of Pt_4/Al_2O_3 surface, respectively.

$$E(\mathrm{CO}*_{\mathrm{terrace}\rightarrow\mathrm{edge}}) = E(\mathrm{CO}*_{\mathrm{edge}}) - E(\mathrm{CO}*_{\mathrm{terrace}}) + E(*_{\mathrm{terrace}}) - E(*_{\mathrm{edge}}) \tag{5.4}$$

Which the diffusion heat of CO adsorbate diffuses from a terrace site to an edge site $E(\mathrm{CO}*_{\mathrm{terrace}\rightarrow\mathrm{edge}})$ is calculated based on the total electronic energy of CO adsorbate and the Pt(1 1 1) surface $E(\mathrm{CO}*_{\mathrm{edge}})$, the total electronic energy of CO adsorbate and the Pt_4/Al_2O_3 surface $E(\mathrm{CO}*_{\mathrm{terrace}})$, the electronic energy of clean Pt(1 1 1) surface $E(*_{\mathrm{terrace}})$, and the electronic energy of clean Pt_4/Al_2O_3 surface $E(*_{\mathrm{edge}})$. Note that current analyses are based off thermodynamics.

5.3.2.3 Reaction Energy Calculation

Energies of all catalytic species of methanol dehydrogenation were calculated using DFT, as discussed in Chapter 2. Reaction energies were calculated via Eq.(5.5) below,

$$\Delta E_{\text{rxn}} = E(\text{product}^*) - E(\text{reactant}^*) \tag{5.5}$$

Since the studied species undergo dehydrogenation reactions, the reaction energy can be written as,

$$\Delta E_{\text{rxn}} = E(\text{CH}_{x-1}\text{O}^*) + E(\text{H}^*) - E(\text{CH}_x\text{O}^*) \tag{5.6}$$

Where the x (ranging from 0-4) denotes the remaining hydrogen in the product CH_{x-1}O and reactant CH_xO, and the energies in the right hand side of equation denote the electronic energy of the system containing the product, adsorbed hydrogen atom, and reactant, respectively. The calculation of the reaction energy is carried out in a fashion which isolates the adsorbates in their separate unit cells, as in other similar studies [16, 18, 20–34].

Note that the geometries of all the reaction intermediates are created under vacuum and optimized to their local minima. The configurations shown later in this chapter are the most favorable geometries on the surface based on the total electronic energy of system and their binding energies. The geometries on Pt(1 1 1) terrace sites are examined and found to be in consistency with existing literature [18, 31]. The the most favorable geometry on the $\text{Pt}_4/\text{Al}_2\text{O}_3$ surface are examined with electronic structure convergence and vibrational frequencies studies, that ensures that the found geometries are stable and at their corresponding local minima.

5.3.2.4 Infrared Frequencies Calculation

Infrared (IR) frequencies of all converged structures from DFT can be estimated by a numerical method of calculating the gradient of the dipole moment of atoms in all six spatial degrees of freedom, i.e., the +x, -x, +y, -y, +z, and -z directions, using a step size of 0.01 Å. The vibrational modes and IR frequencies are calculated from the dynamical matrix [35–45]. All finite-difference based frequency calculations are performed in VASP using the the Atomic Simulation Environment (ASE) interface [46]. Precision is set to be accurate. Energy cutoff is set as 400 eV. The electronic convergence and force convergence are consistent with the criteria discussed in Chapter 2. Note

that this method shares the same principle that VASP originally offers which is commonly used to obtain vibrational modes [47–50] and also has the added functionality of including intensities which are calculated by calculating eigenfrequencies and eigenvectors of the Hamiltonian. This is also frequently done in regular VASP routines. Detailed mathematical implementation can be found at https://gitlab.com/ase/ase/blob/master/ase/vibrations/infrared.py. The ASE python interface is responsible for generating the workflow and communicating with VASP to generate a series of DFT calculations that iterate over all the chosen atoms and perturb them in finite displacement in all degrees of freedom and then run single point calculations on all images containing perturbed atom positions until electronic convergence. Details about how to carry out such calculation are described in Appendix D.

5.4 Results

5.4.1 Structures and Binding Energies of Reaction Intermediates

Chemical species CH_3OH*, CH_2OH*, CHOH*, COH*, CH_3O*, CH_2O*, CHO*, CO* are chosen for this study since they are all possible species that complete the methanol dehydrogenation network [28, 31]. The adsorbates marked with asterisk sign indicate that the chemical species are in their adsorbed states to the catalyst surface, e.g. CH_3OH* refers to the CH_3OH and catalytic site complex. Computed and optimized structures with the lowest total electronic energy for each intermediate of these adsorbates on the terrace Pt(1 1 1) catalyst surface and on Pt_4/Al_2O_3 edge surface are presented in Figure 5.3 and Figure 5.4, respectively. For clarity, views are zoomed in for viewing adsorbates structures.

We noticed that almost all the -OH containing adsorbates (except for CH_3OH), when adsorbed on edge sites, their most stable configurations prefer orientations that are nearly parallel to the surface. While C-O/C=O containing adsorbates (except for CHO), their most stable configurations prefer binding through O to Al atom of the alumina support, forming an angle between the C-O/C=O bond to the surface. These binding patterns are different than the ones we observed for terrace sites bound intermediates, that most of them (except for CH_2O) form 'angular' binding configurations, either through C or O atoms.

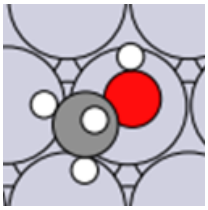

(a) Top view of CH_3OH*

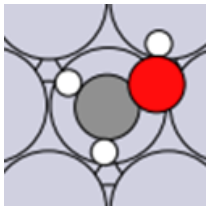

(b) Top view of CH_2OH*

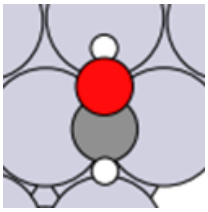

(c) Top view of CHOH*

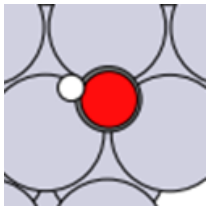

(d) Top view of COH*

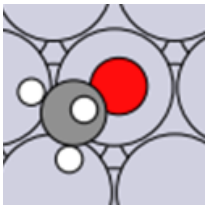

(e) Top view of CH_3O*

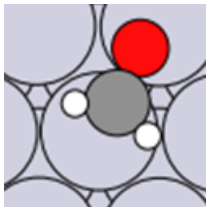

(f) Top view of CH_2O*

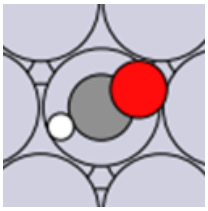

(g) Top view of CHO*

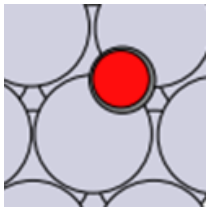

(h) Top view of CO*

Figure 5.3: Visualization of CH_3OH*, CH_2OH*, CHOH*, COH*, CH_3O*, CH_2O*, CHO*, CO* on Pt(1 1 1) terrace sites. Color key: Grey: Pt, Red: O, Dark grey: C, White: H.

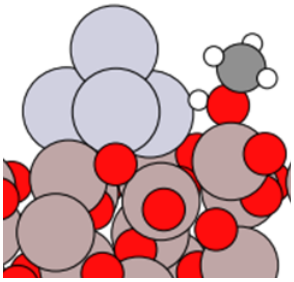

(a) Front view of CH_3OH^*

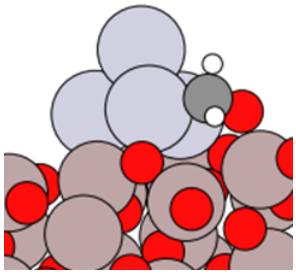

(b) Front view of CH_2OH^*

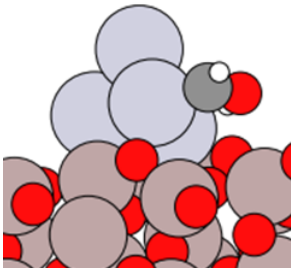

(c) Front view of $CHOH^*$

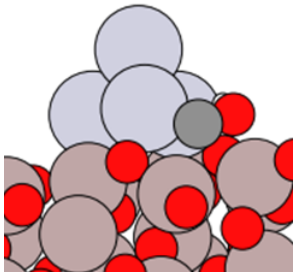

(d) Front view of COH^*

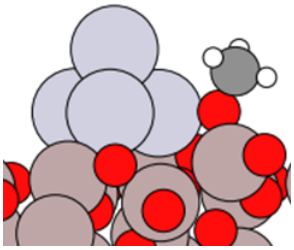

(e) Front view of CH_3O^*

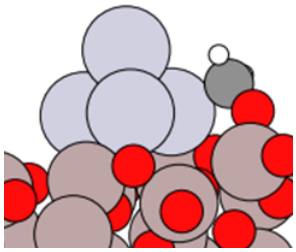

(f) Front view of CH_2O^*

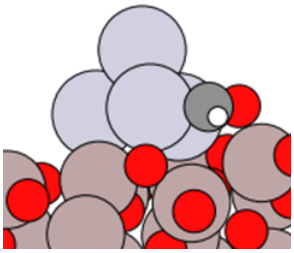

(g) Front view of CHO^*

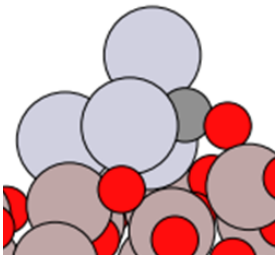

(h) Front view of CO^*

Figure 5.4: Visualization of CH_3OH^*, CH_2OH^*, $CHOH^*$, COH^*, CH_3O^*, CH_2O^*, CHO^*, CO^* on Pt_4/Al_2O_3 edge sites. Color key: Grey: Pt, Red: O, Light brown: Al, Dark grey: C, White: H.

Table 5.1: Binding energies for terrace and edge sites and calculated diffusion heat from terrace sites to edge sites. Energy unit in eV (1 eV = 96.485 kJ/mol). Note: Binding energies of CH_2O and CO in parentheses are the energies using CH_2O(gas) CO(gas) as their reference species.

Chemical Species Name	**Binding Energy (Terrace)**	**Binding Energy (Edge)**	**Diffusion Heat($_{terrace \rightarrow edge}$)**
CH_3OH	-0.72	-0.48	0.24
CH_2OH	-0.58	-0.19	0.39
CHOH	-0.34	0.27	0.61
COH	-0.39	0.35	0.74
CH_3O	0.25	-0.37	-0.62
CH_2O	0.29 (-1.14)	0.27 (-1.10)	-0.02
CHO	0.11	-0.69	-0.80
CO	-0.26 (-2.24)	-0.46 (-2.40)	-0.20

5.4.2 Calculated Energies

5.4.2.1 Binding Energies

DFT calculated binding energies of all possible dehydrogenated species of methanol decomposition on both terrace Pt(1 1 1) sites and on Pt_4/Al_2O_3 edge are listed in Table 5.1. It lists the binding energy of intermediates on terrace sites and edge sites, and the third column lists the calculated diffusion heat of each stable intermediate diffusing from terrace sites onto edge sites. If the diffusion direction is reversed, i.e. from edge sites to terrace sites, the signs of the diffusion heat are reversed correspondingly. This reported quantity measures the driving force of diffusion from the point view in thermodynamics. By including the diffusion heat into the binding energy, we can observe the preferable binding sites of all adsorbates. For CO and CH_2O, since they are saturated, we are able to calculate their binding energies that refer to their own gas phase energies, which are tabulated in the table with parentheses. More information of different binding modes of CO can be found in Appendix C. We found CH_2O exhibit the diffusion heat of a magnitude of 0.02 eV, implying it has no significant thermodynamic preference in binding on edge and terrace sites. Species containing OH groups, i.e. CH_3OH, CH_2OH, CHOH, and COH prefer binding on terrace

sites since all the diffusion heat to edge sites is endothermic. This is also suggested in the reaction pathways in Figure 5.5, that terrace sites of Pt(1 1 1) preferentially catalyze C-H bond breaking [3, 22, 28, 51, 52]. Species containing ether/carbonyl groups, i.e. CH_3O, CH_2O, CHO, and CO prefer binding on edge sites since all the diffusion heat to terrace sites is endothermic. This is also suggested in the reaction pathways in Figure 5.6, that edges sites of Pt_4/Al_2O_3 initially catalyze O-H bond breaking and stabilizes methoxy and its dehydrogenated derivatives.

5.4.2.2 Reaction Energies

DFT calculated reaction energies of elementary dehydrogenation reactions of methanol decomposition on both terrace Pt(1 1 1) sites and on Pt_4/Al_2O_3 edge sites with the diffusion heat of the final product are listed in Table 5.2. The 2nd column of the data, which corresponds to the reaction energies on terrace sites, shows a general trend that on terrace sites, dehydrogenation on alkyl hydrogen initially is more favorable than dehydrogenation on hydroxyl hydrogen: $CH_3OH^* + * \rightarrow CH_2OH^* + H^*$ having -0.48 eV of reaction heat vs $CH_3OH^* + * \rightarrow CH_3O^* + H^*$ having 1.12 eV of reaction heat. The subsequent dehydrogenation on alkyl hydrogen also shows favorable reaction thermodynamics. Same favorableness is found for derivatives of methoxy, although the methoxy group is unlikely to form at first place due to very endothermic reaction energy on terrace sites. The 3rd column includes the reaction energies on edge sites, shows that the initial dehydrogenation over the oxygen atom becomes facilitated. That is to say, the inhibited $CH_3OH^* + * \rightarrow CH_3O^* + H^*$ reaction on terrace site becomes just slightly endothermic, the reaction energy goes down from 1.12 eV on the terrace site to 0.15 eV on the edge site. In fact, this reaction energy is less than half of the energy of the competing reaction that dehydrogenates alkyl hydrogen on the edge site, $CH_3OH^* + * \rightarrow CH_2OH^* + H^*$, which shows 0.32 eV. Upon the consideration of reaction energies in the table, steps of

- $CH_3OH + * \rightarrow CH_3OH^*$ favors reaction on a terrace site,
- $CH_2OH^* + * \rightarrow CHOH^* + H^*$ favors reaction on a terrace site,
- $CH_2OH^* + * \rightarrow CHOH^* + H^*$ favors reaction on a terrace site,
- $CHOH^* + * \rightarrow COH^* + H^*$ favors reaction on a terrace site,
- $COH^* + * \rightarrow CO^* + H^*$ favors reaction on an edge site,

- $CH_3OH^* + * \rightarrow CH_3O^* + H^*$ favors reaction on an edge site,
- $CH_3O^* + * \rightarrow CH_2O^* + H^*$ favors reaction on a terrace site,
- $CH_2O^* + * \rightarrow CHO^* + H^*$ favors reaction on a terrace site,
- $CHO^* + * \rightarrow CO^* + H^*$ favors reaction on an edge site,
- $CH_2OH^* + * \rightarrow CH_2O^* + H^*$ favors reaction on a terrace site,
- $CHOH^* + * \rightarrow CHO^* + H^*$ favors favors reaction on an edge site.

A general observation can be made that dehydrogenation of –CH are favored on terrace sites and dehydrogenation of –OH can be initiated on edge sites.

Table 5.2: Reaction energy for elementary dehydrogenation reactions of methanol decomposition on terraces sites on Pt(1 1 1) surface and edges sites on Pt_4/γ -Al_2O_3 surface. Energy unit in eV (1 eV = 96.485 kJ/mol).

Reaction	$\mathbf{E_{rxn}}$ **terrace sites**	$\mathbf{E_{rxn}}$ **edge sites**
$\mathbf{CH_3OH + * \rightarrow CH_3OH^*}$	-0.53	-0.41
$\mathbf{CH_3OH^* + * \rightarrow CH_2OH^* + H^*}$	-0.48	0.32
$\mathbf{CH_2OH^* + * \rightarrow CHOH^* + H^*}$	-0.39	0.53
$\mathbf{CHOH^* + * \rightarrow COH^* + H^*}$	-0.65	1.98
$\mathbf{COH^* + * \rightarrow CO^* + H^*}$	-0.51	-2.57
$\mathbf{CH_3OH^* + * \rightarrow CH_3O^* + H^*}$	1.12	0.15
$\mathbf{CH_3O^* + * \rightarrow CH_2O^* + H^*}$	-0.58	0.70
$\mathbf{CH_2O^* + * \rightarrow CHO^* + H^*}$	-0.73	1.41
$\mathbf{CHO^* + * \rightarrow CO^* + H^*}$	-1.08	-1.99
$\mathbf{CH_2OH^* + * \rightarrow CH_2O^* + H^*}$	0.26	1.41
$\mathbf{CHOH^* + * \rightarrow CHO^* + H^*}$	-0.08	-2.57

5.4.3 Identification of Reaction Pathways

By examining the listed reaction energies along different pathways in methanol decomposition on on Pt(1 1 1) terrace sites and Pt_4/Al_2O_3 edge sites. It is found that the initial steps of dehydrogenation that occur on Pt(1 1 1) terrace sites are likely to be in the order of depleting alkyl hydrogen atoms first, leaving the alcoholic function group -OH intact until the very last step of dehydrogenation to CO. Consequently, the reaction route are likely to be $CH_3OH \rightarrow CH_2OH \rightarrow CHOH \rightarrow COH \rightarrow CO$ (as highlighted in bold arrows in Fig. 5.5). This finding is in good agreement with existing literature [18, 31]. As a result, we expect CH_3OH, CH_2OH, CHOH, COH, CHO, and CO species to be the present species on terrace sites.

On the other hand, the initial steps of dehydrogenation that occur on Pt_4/Al_2O_3 edge sites are likely to be in the order of depleting alcoholic function group -OH first, then starting depleting alkyl hydrogen atoms. Consequently, the reaction route are likely to be $CH_3OH \rightarrow CH_3O$ (as highlighted in bold arrows in Fig. 5.6). Unlike the preferred reaction route on terrace sites, this reaction route is likely to end at CH_3O due to the endothermic reaction energies for further steps. As a result, we expect CH_3O to be present on edge sites but not as dominant species compared to CO and CH_xOH derivatives.

We found that the reaction energies for the Pt_4/Al_2O_3 edge sites provide a different energy landscape than the one from the terrace sites. This result suggested that the edge site may play a role in initial step and provided competency of dehydrogenation of O-H group instead Pt terrace sites which are known for promoting C-H bond breaking [3, 22, 28, 51, 52]. Similarly, published work addressed the importance of edge sites in oxygenation oxidation and reforming, for example, it is suggested that the edge site may serve a crucial role in C-O bond activation according to Wieckowski et al [51]. It was also suggested that edge sites of Pt/Al_2O_3 catalyst is preferentially promoting decarbonylation reactions, by Sievers et al [53] and Tornquist et al [54]. Our results show that as the reaction proceeds on the edge sites, further dehydrogenation along the preferred pathway becomes significant endothermic after the first step, which indicates that the reaction may seek alternative routes to proceed, that is to say, the most thermodynamically favorable reaction pathway may very well not all occur on a standalone type of sites. In fact, after combining the point view of reaction and diffusion, the last step of the thermodynamically favored reaction pathway of terrace sites, can end with an extra diffusion step, which corresponding to an exothermic heat of

CO diffusing from a terrace site to an edge site.

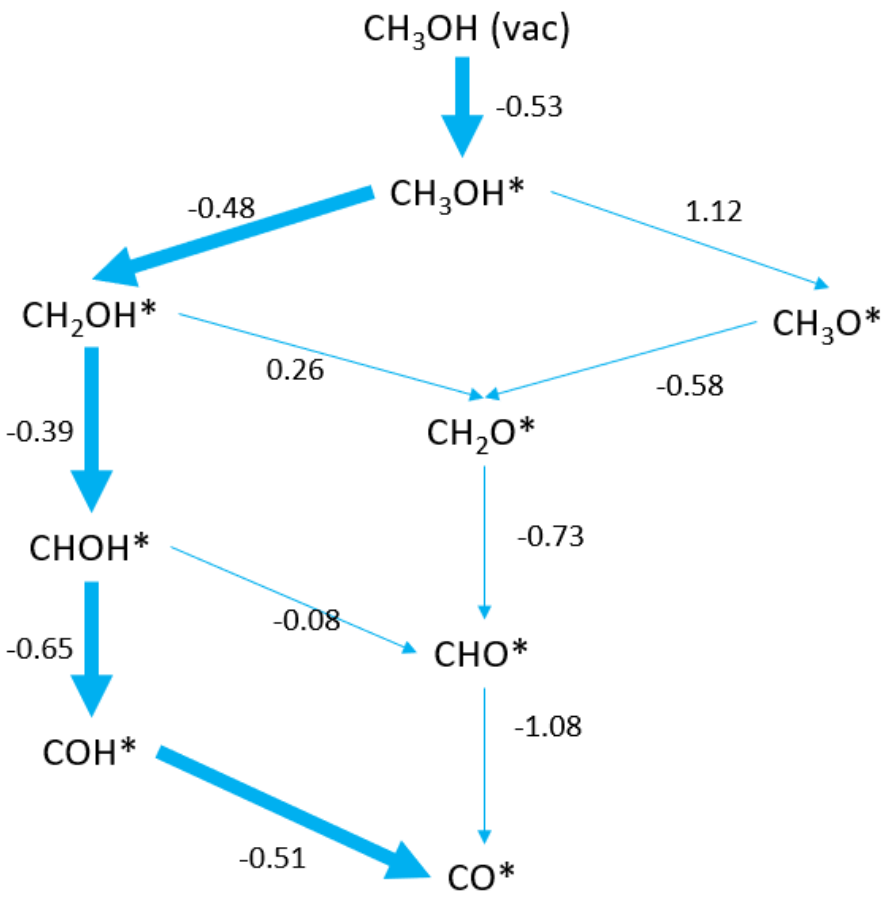

Figure 5.5: Schematic view of the reaction pathways of methanol dehydrogenation towards CO on Pt(1 1 1) terrace sites. Arrows indicate the reaction proceeding direction. Arrows in bold are preferred reactions in perspective of reaction energy (labeled, unit in eV). For clarity, top view of each configuration of the adsorbate is attached next to the chemical name of the adsorbate. Color key: Grey: Pt, Red: O, Dark grey: C, White: H.

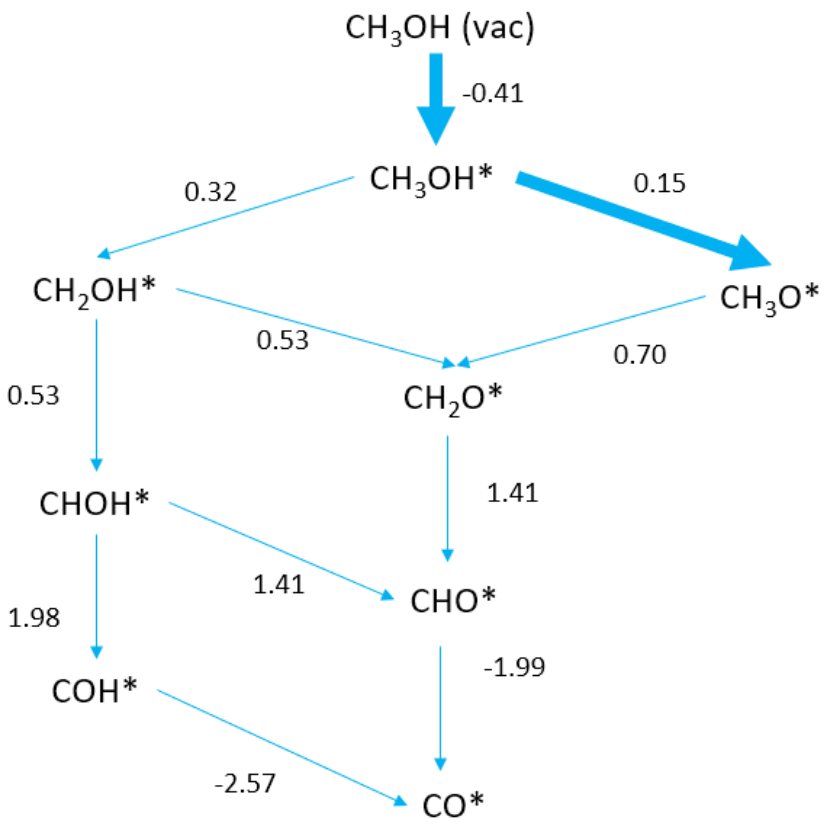

Figure 5.6: Schematic view of the reaction pathways of methanol dehydrogenation towards CO on Pt_4/Al_2O_3 edge sites. Arrows indicate the reaction proceeding direction. Arrows in bold are preferred reactions in perspective of reaction energy (labeled, unit in eV). For clarity, top view and front view of each configuration of the adsorbate are attached next to the chemical name of the adsorbate. Color key: Grey: Pt, Red: O, Light brown: Al, Dark grey: C, White: H.

5.4.4 Experimental and Calculated Infrared Vibrational Frequencies

Dipole moment based IR frequencies are calculated in DFT for all possible intermediates within the methanol decomposition reaction network. The set of spectra can be found in Figure 5.7. Each sub-figure represents the calculated IR spectra of a certain chemical species adsorbed on a terrace site and on an edge site.

Figure 5.8 shows our experimental collaborator's findings on IR spectra of the catalyst after ramping the temperature from 50 C° to 450 C°. At low temperatures, (50 C° to 250 C°), methanol did not undergo full decomposition, possibly due to insufficient kinetic energies to overcome reaction

barriers. The broad shoulder in the 3500 - 3000 cm $^{-1}$ that corresponds to O-H stretching and strong peaks in 3000 - 2750 cm $^{-1}$ that corresponds to C-H stretching also indicate the incompletion of the methanol decomposition. C=O stretching peak at 2000 cm $^{-1}$ was not well pronounced. Whereas at high temperatures, (350 C° to 450 C°), reaction can undergo thoroughly to arrive at CO, by overcoming kinetic barriers. From the obtained spectroscopy, the O-H stretching shoulder and C-H stretching peaks significantly decreased and the intensity of C=O stretching peak at 2000 cm $^{-1}$ significantly increased. This indicates that after the temperature reached 350 C^o and above, methanol went though a more thorough decomposition than the ones at low temperatures. More evidence comes from the peak near 2000 cm $^{-1}$, which intensified with the increase of temperature, as the major product CO is produced and accumulated on the surface. Combining the observation from the computational and experimental spectra, we can hypothesize the following:

For simplicity all the binding sites are abbreviated in parenthesis following the chemical names of the adsorbates, for example, CH_3OH(edge) refers to CH_3OH adsorbate on an edge site, same for CH_3OH(terrace) refers to CH_3OH adsorbate on a terrace site.

- Peaks between 3000 cm $^{-1}$ to 2700 cm $^{-1}$ corresponding to C-H stretching, indicating C-H containing species may exist on the catalyst surface. We found intermediates CH_3O(edge), CH_2O(edge), CHO(edge), CH_2OH(edge) and CHOH(edge), along with CH_3O(terrace) can have well pronounced peaks at this location therefore can be present at the catalyst surface.

- Peaks near 2000 cm $^{-1}$ corresponding to C=O stretching, indicating C=O containing species may exist on the catalyst surface. Our calculations predict that only CH_3OH(edge) and CO_L(terrace) can exhibit such peaks therefore they can be at presence on the surface.

- Peaks between 2000 cm $^{-1}$ and 1700 cm $^{-1}$ corresponding to C=O stretching. Calculated frequencies show that all bridge binding CO_B, (i.e. hcp, fcc and bridge of terrace sites) they all fall in this region. While the CO(edge) exhibits the peak near 1450 cm^{-1}. This ether like CO stretching peak is from the oxygen atom binding to an Al atom of the alumina support thus behaves as saturated O.

- Peaks between 1300 cm $^{-1}$ and 1000 cm $^{-1}$ corresponding to C–O stretching. Our calculated frequencies imply that adsorbates CH_2OH(terrace), CHOH(terrace), COH(terrace), CH_2O(terrace), along with CH_3O(edge), CH_2O(edge) are the possible sources of the peaks.

Assumptions about which chemical species are at presence on the surface are made based on the information of the peaks of functional groups such as C-O, C=O, and C-H and their intensities are made, and on the comparison between the experimental and computational spectra. It can be deduced that, CH_2OH, CHOH, COH and CO on terrace sites are likely to be dominant species on terrace sites. On the other hand, CH_3O and CO are likely to be dominant species on edge sites. These assumptions can reflect the major peak locations on the experimental IR spectra. Moreover, the peak slightly below 1500 cm^{-1}, the source can be related to the ether peak from CO(edge) species. The assumptions are well in line with the results in previous subsection that the alkyl dehydrogenation preferentially occur on terrace sites and dehydrogenation involving methoxy and its derivatives preferentially occur on edge sites.

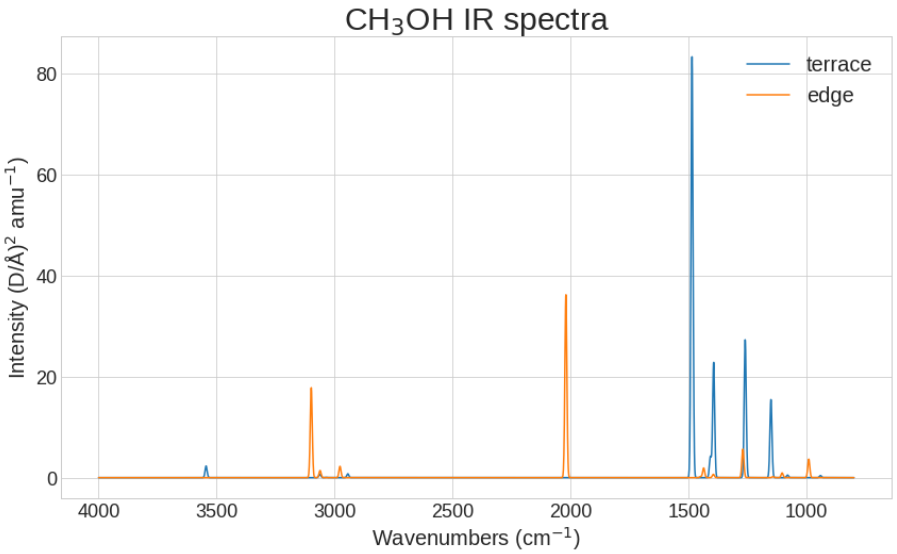

(a) Calculated Infrared Spectra of CH_3OH

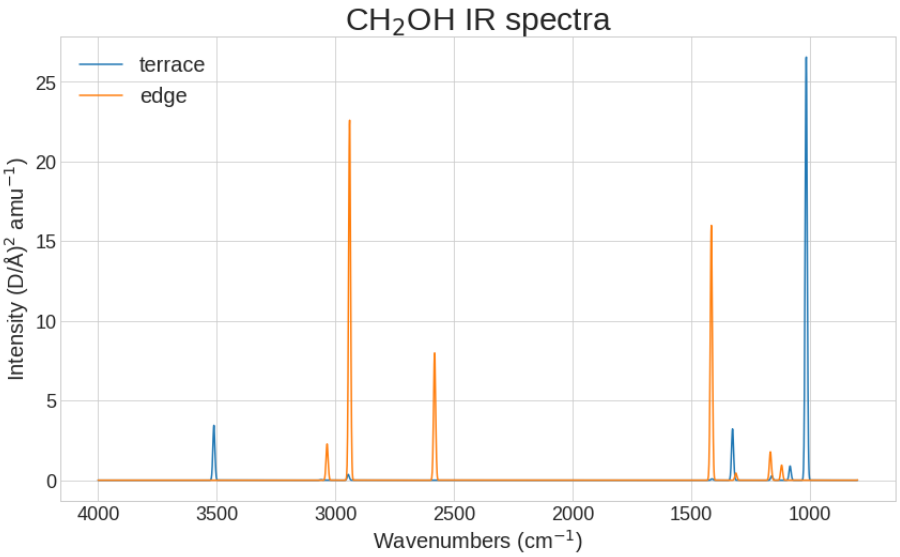

(b) Calculated Infrared Spectra of CH_2OH

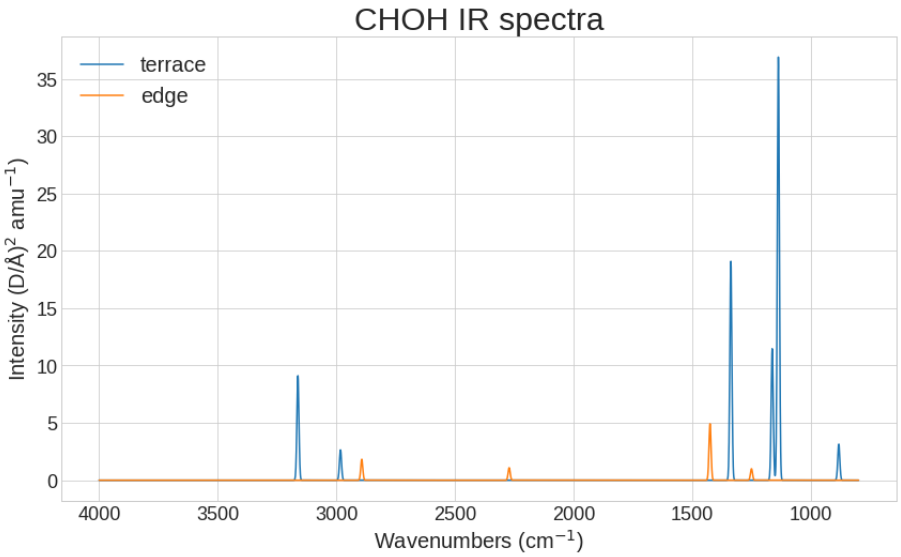

(c) Calculated Infrared Spectra of CHOH

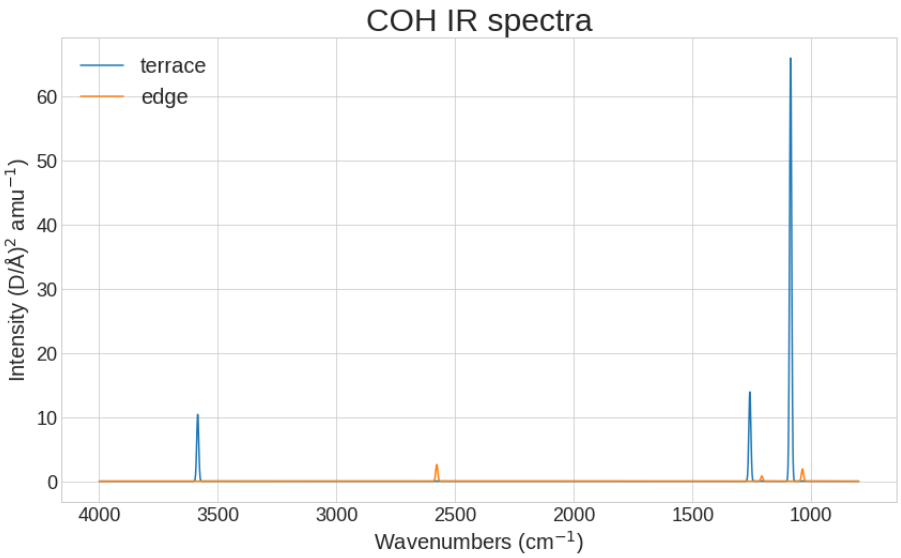

(d) Calculated Infrared Spectra of COH

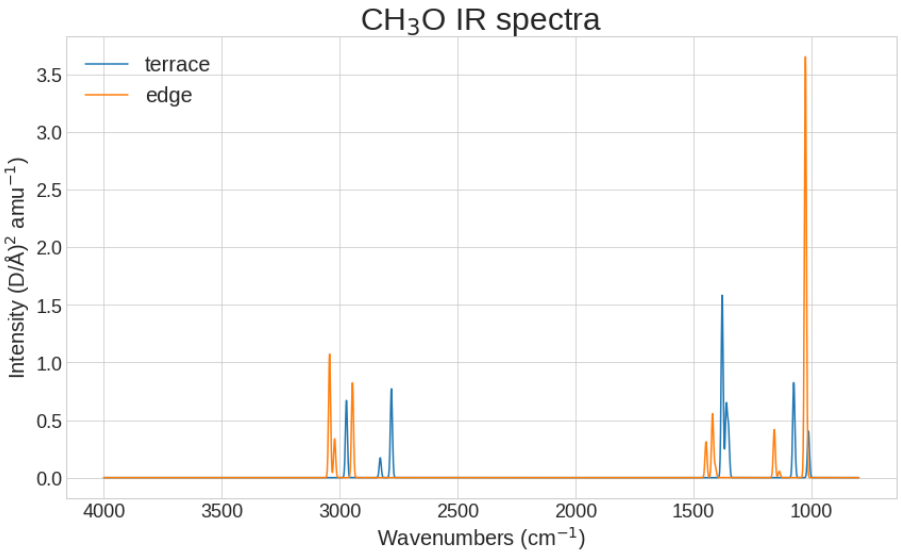

(e) Calculated Infrared Spectra of CH_3O

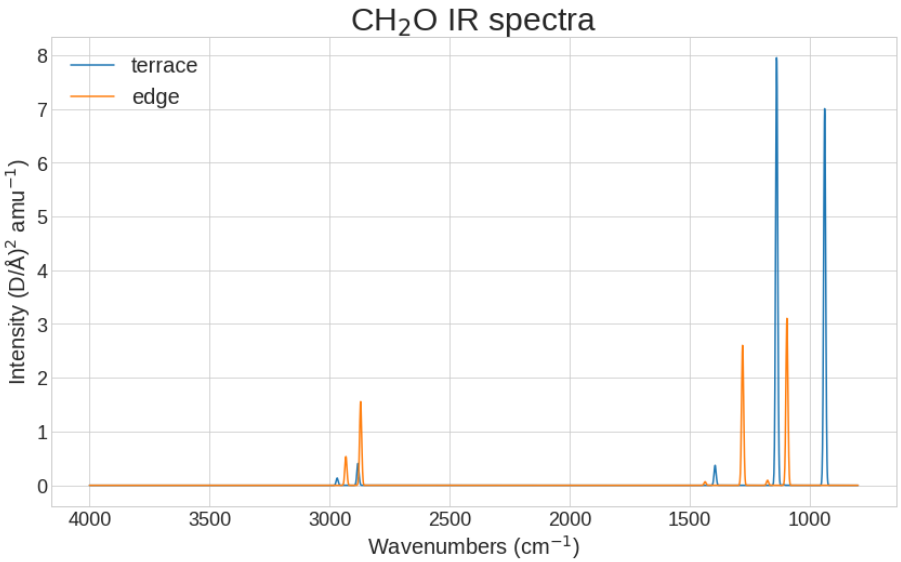

(f) Calculated Infrared Spectra of CH_2O

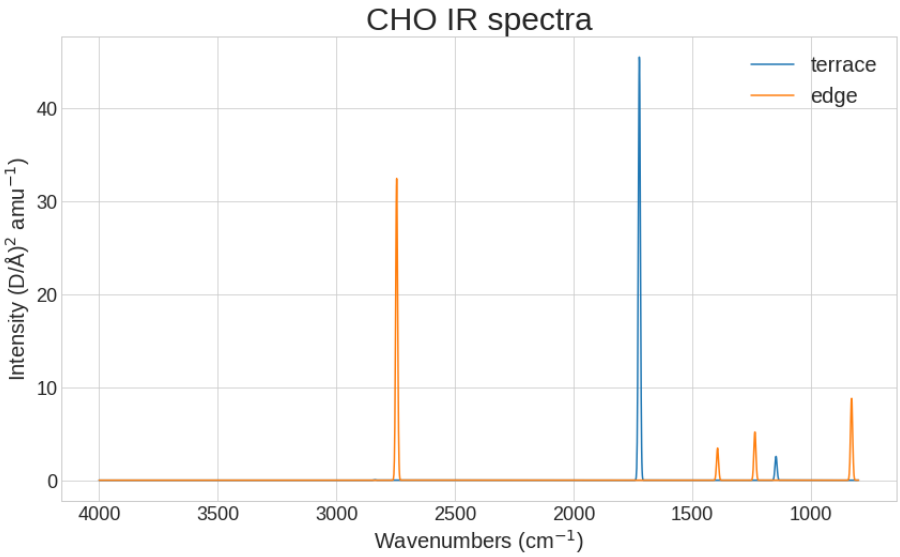

(g) Calculated Infrared Spectra of CHO

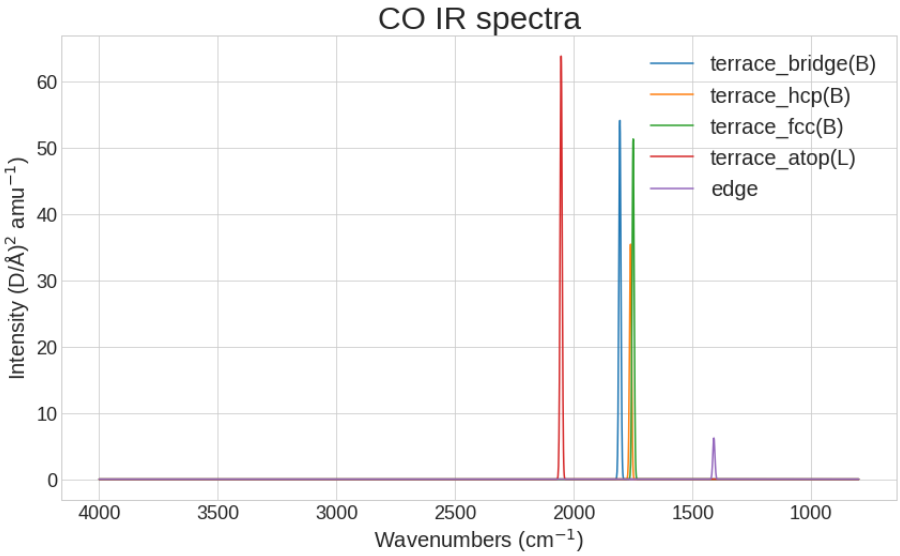

(h) Calculated Infrared Spectra of CO

Figure 5.7: Calculated IR spectra of all possible species of methanol dehydrogenation on terrace and edge sites

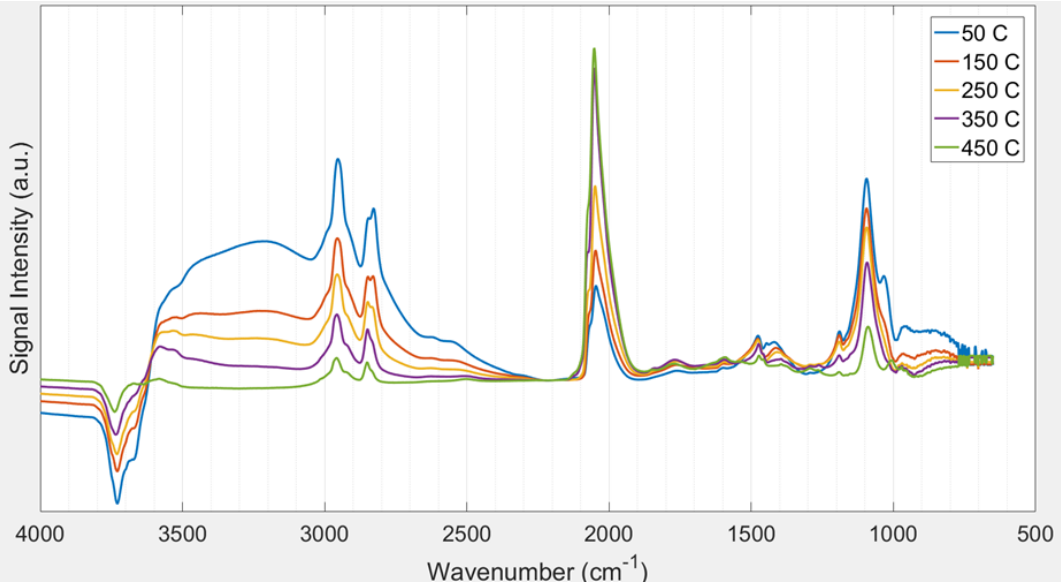

Figure 5.8: Experimental IR spectra of MeOH on 1% Pt/Al_2O_3 (reduced at 500 C^o) at different temperatures.
Courtesy of Bryan Hare and Dr. Carsten Sievers, School of Chemical and Biomolecular Engineering, Georgia Institute of Technology.

5.5 Discussion

Our studies of methanol dehydrogenation on an advanced catalyst model along with a traditional catalyst model, allow us to reflect terrace sites and edge sites that can exist in real catalyst of Pt/Al_2O_3, and to investigate thermodynamics that can be used to shed light upon preferred binding sites, dominant surface species, and preferred reaction pathways. The binding energy combined with diffusion energy between terrace sites and edge sites are taken into consideration to determine the preferred binding sites. In general, the diffusion will not change the binding preference on the type of active sites of adsorbates. In a scenario where the surface coverage is low, i.e. the surface is not crowded with intermediates, species containing –OH group will prefer terrace binding since all the diffusion heat to edge sites is endothermic; Species containing –CO groups prefer edge binding since all the diffusion heat to terrace sites is endothermic. Future work can refer to literature from Mavrikakis's systematically presented adsorption and diffusion of atomic and diatomic species (H, C, N, O, CO, and NO) on nanometer-sized Pt and Cu. They showed that there can be a BEP (Brønsted-Evans-Polanyi) type linear correlation established between the transition diffusion state

energy and the initial state energy for adsorbate diffusion across the edges of Pt and Cu nanoparticles [55]. Though the R^2 value of 0.62 is far from being perfect, the explicitly calculated activation barrier of CO diffusion across the edges is found to be 0.41 eV. With CO being possibly the strongest bound species on the surface (See binding energies of CO on terrace and edge sites in Table 5.1), the diffusion barriers for other species are likely to have an upper bound value equal to 0.41 eV. This barrier could be due to the small size of the Pt_4 cluster, and other species sterically blocking the edge sites.

From the study of IR spectra of terrace site bound and edge site bound CO, we found that terrace site bound CO_L is more dominant on surface that is matching with the experimental spectra. This is possibly a consequence of terrace sites being more available than edge sites. It could also be from the used generalized-gradient-approximation exchange-correlation failed to accurately capture the correct binding mode of CO [56–60]. Speculations are also made for other possible dominant species on both terrace and edge sites. CH_2OH, CHOH, COH and CO on terrace sites are likely to be dominant. While CH_3O and CO on edge sites are likely to be dominant. This information is useful to gain insights of the surface chemistry and help interpret our experimental collaborator's results in depth.

5.6 Conclusions

In this work, we investigated thermodynamics of reactions pertaining to methanol decomposition, on two type of catalytic sites that exist in realistic supported catalyst: terrace sites and edge sites. The binding energies of intermediates on these two sites show distinctive hierarchy. Intermediates that contain intact –OH group have lower binding energies on terrace sites than those on edge sites, meaning they are more stable on terrace sites. Intermediates that do not contain intact –OH group have lower binding energies on edge sites than those on terrace sites, meaning they are more stable on edge sites. One exception being formaldehyde CH_2O, shows nearly identical binding hierarchy on terrace and edge sites. Binding hierarchy can be useful for further study since it enables the study of diffusion of intermediates between terrace and edge sites, which likely to occur in real experiments. Reaction energies are also calculated to propose reaction pathways that are thermodynamically favored. Proposed reaction pathways of methanol decomposition on both terrace Pt(1 1 1) sites are presented. On the terrace site, the most thermodynamically favored pathway is CH_3OH

$\rightarrow CH_3O \rightarrow CH_2O \rightarrow CHO \rightarrow CO$. On the edge site, the most thermodynamically favored pathway is $CH_3OH \rightarrow CH_3O$. The steps after CH_2O on the edge sites are unlikely to occur, possibly due to the endothermic reaction thermodynamics and the tendency of CH_2O desorption. Our result of CO binding to the edge site compared to the terrace site, which exhibit a exothermic diffusion heat, can be an evidence that linking to the tendency of CO crowding the edge sites, which is observed by our experimental collaborator [53]. Computationally derived IR spectroscopy data is generated for all possible intermediates on terrace and edge sites. It is used to hint the present species when compared to real IR spectroscopy data. We propose CH_2OH, CHOH, COH and CO are likely to be present on terrace sites; and CH_3O and CO are likely to be present on edge sites.

5.7 Acknowledgments

This research was funded in part by the National Science Foundation (Award CBET-1764296), as well as the Chemical and Biomolecular Engineering Department at Clemson University. Simulations were performed on the Palmetto Supercomputer Cluster, which is maintained by the Cyberinfrastructure Technology Integration Group at Clemson University. We thank Dr. Carsten Sievers and his graduate student Bryan J. Hare at Georgia Institute of Technology, for providing experimental data and feedback.

5.8 Reference

[1] Dangguo Gong, Vishnu Priya Subramaniam, James G Highfield, Yuxin Tang, Yuekun Lai, and Zhong Chen. "In situ mechanistic investigation at the liquid/solid interface by attenuated total reflectance FTIR: Ethanol photo-oxidation over pristine and platinized TiO2 (P25)". *Acs Catalysis* 1.8 (2011), 864–871.

[2] D Cao, G-Q Lu, Andrzei Wieckowski, Sally A Wasileski, and Matthew Neurock. "Mechanisms of methanol decomposition on platinum: A combined experimental and ab initio approach". *The Journal of Physical Chemistry B* 109.23 (2005), 11622–11633.

[3] Jeremy Kua and William A Goddard. "Oxidation of methanol on 2nd and 3rd row group VIII transition metals (Pt, Ir, Os, Pd, Rh, and Ru): application to direct methanol fuel cells". *Journal of the American Chemical Society* 121.47 (1999), 10928–10941.

[4] VS Bagotzky, Yu B Vassiliev, and OA Khazova. "Generalized scheme of chemisorption, electrooxidation and electroreduction of simple organic compounds on platinum group metals". *Journal of Electroanalytical Chemistry and Interfacial Electrochemistry* 81.2 (1977), 229–238.

[5] Yan Xia Chen, Atsushi Miki, Shen Ye, Hidetada Sakai, and Masatoshi Osawa. "Formate, an active intermediate for direct oxidation of methanol on Pt electrode". *Journal of the American Chemical Society* 125.13 (2003), 3680–3681.

[6] NM Marković and PN Ross Jr. "Surface science studies of model fuel cell electrocatalysts". *Surface Science Reports* 45.4-6 (2002), 117–229.

[7] John R Copeland, Guo Shiou Foo, Lindsey A Harrison, and Carsten Sievers. "In situ ATR-IR study on aqueous phase reforming reactions of glycerol over a Pt/γ-Al2O3 catalyst". *Catalysis today* 205 (2013), 49–59.

[8] Prateek Mehta, Jeffrey Greeley, W Nicholas Delgass, and William F Schneider. "Adsorption Energy Correlations at the Metal–Support Boundary". *ACS Catalysis* 7.7 (2017), 4707–4715.

[9] J Christopher Brown and Erdogan Gulari. "Hydrogen production from methanol decomposition over Pt/Al2O3 and ceria promoted Pt/Al2O3 catalysts". *Catalysis Communications* 5.8 (2004), 431–436.

[10] Rong He, Rupali R Davda, and James A Dumesic. "In Situ ATR-IR Spectroscopic and Reaction Kinetics Studies of Water- Gas Shift and Methanol Reforming on Pt/Al2O3 Catalysts in Vapor and Liquid Phases". *The Journal of Physical Chemistry B* 109.7 (2005), 2810–2820.

[11] A Sarkany, Gy Stefler, and JW Hightower. "Participation of support sites in hydrogenation of 1, 3-butadiene over Pt/Al2O3 catalysts". *Applied Catalysis A: General* 127.1-2 (1995), 77–92.

[12] Xénophon Krokidis, Pascal Raybaud, Anne-Elisabeth Gobichon, Bernadette Rebours, Patrick Euzen, and Hervé Toulhoat. "Theoretical study of the dehydration process of boehmite to γ-alumina". *The Journal of Physical Chemistry B* 105.22 (2001), 5121–5130.

[13] M Digne, Philippe Sautet, Pascal Raybaud, P Euzen, and H Toulhoat. "Use of DFT to achieve a rational understanding of acid–basic properties of γ-alumina surfaces". *Journal of Catalysis* 226.1 (2004), 54–68.

[14] Chao Hao Hu, Céline Chizallet, Christophe Mager-Maury, Manuel Corral-Valero, Philippe Sautet, Hervé Toulhoat, and Pascal Raybaud. "Modulation of catalyst particle structure upon support hydroxylation: Ab initio insights into Pd13 and Pt13/γ-Al2O3". *Journal of Catalysis* 274.1 (2010), 99–110.

[15] Chenggang Zhou, Jinping Wu, TJ Dhilip Kumar, Naduvalath Balakrishnan, Robert C Forrey, and Hansong Cheng. "Growth pathway of Pt clusters on α-Al2O3 (0001) surface". *The Journal of Physical Chemistry C* 111.37 (2007), 13786–13793.

[16] Sandeep Nigam and Chiranjib Majumder. "ORR viability of alumina-supported platinum nanocluster: exploring oxidation behaviour by DFT". *Physical Chemistry Chemical Physics* 19.29 (2017), 19308–19315.

[17] Christophe Mager-Maury, C Chizallet, P Sautet, and P Raybaud. "Platinum nanoclusters stabilized on γ-alumina by chlorine used as a capping surface ligand: a density functional theory study". *ACS catalysis* 2.7 (2012), 1346–1357.

[18] Jeff Greeley and Manos Mavrikakis. "Competitive Paths for Methanol Decomposition on Pt(111)". *Journal of the American Chemical Society* 126.12 (2004), 3910–3919.

[19] Cameron J. Bodenschatz, Sapna Sarupria, and Rachel B. Getman. "Molecular-Level Details about Liquid H2O Interactions with CO and Sugar Alcohol Adsorbates on Pt(111) Calculated Using Density Functional Theory and Molecular Dynamics". *The Journal of Physical Chemistry C* 120.1 (2015), 801–801.

[20] Ryosuke Jinnouchi, Kensaku Kodama, and Yu Morimoto. "DFT calculations on H, OH and O adsorbate formations on Pt (111) and Pt (332) electrodes". *Journal of Electroanalytical Chemistry* 716 (2014), 31–44.

[21] Vassili Vorotnikov, Giannis Mpourmpakis, and Dionisios G Vlachos. "DFT study of furfural conversion to furan, furfuryl alcohol, and 2-methylfuran on Pd (111)". *Acs Catalysis* 2.12 (2012), 2496–2504.

[22] Irineo Pedro Zaragoza, Roberto Salcedo, and Jaime Vergara. "DFT: a dynamic study of the interaction of ethanol and methanol with platinum". *Journal of molecular modeling* 15.5 (2009), 447.

[23] Chaoquan Hu, Siu-Wa Ting, Kwong-Yu Chan, and Wei Huang. "Reaction pathways derived from DFT for understanding catalytic decomposition of formic acid into hydrogen on noble metals". *International Journal of Hydrogen Energy* 37.21 (2012), 15956–15965.

[24] Chunrong Song, Qingfeng Ge, and Lichang Wang. "DFT studies of Pt/Au bimetallic clusters and their interactions with the CO molecule". *The Journal of Physical Chemistry B* 109.47 (2005), 22341–22350.

[25] Tianjun Xie, Sapna Sarupria, and Rachel B Getman. "A DFT and MD study of aqueous-phase dehydrogenation of glycerol on Pt (1 1 1): comparing chemical accuracy versus computational expense in different methods for calculating aqueous-phase system energies". *Molecular Simulation* 43.5-6 (2017), 370–378.

[26] Tianjun Xie, Cameron J Bodenschatz, and Rachel B Getman. "Insights into the roles of water on the aqueous phase reforming of glycerol". *Reaction Chemistry & Engineering* 4.2 (2019), 383–392.

[27] Bin Liu and Jeffrey Greeley. "A density functional theory analysis of trends in glycerol decomposition on close-packed transition metal surfaces". *Physical Chemistry Chemical Physics* 15.17 (2013), 6475.

[28] Jeff Greeley and Manos Mavrikakis. "Competitive paths for methanol decomposition on Pt (111)". *Journal of the American Chemical Society* 126.12 (2004), 3910–3919.

[29] Jeff Greeley, Thomas F Jaramillo, Jacob Bonde, IB Chorkendorff, and Jens K Nørskov. "Computational high-throughput screening of electrocatalytic materials for hydrogen evolution". *Materials For Sustainable Energy: A Collection of Peer-Reviewed Research and Review Articles from Nature Publishing Group*. World Scientific, 2011, 280–284.

[30] Jeff Greeley, Jens K Nørskov, Ludwig A Kibler, Ahmed M El-Aziz, and Dieter M Kolb. "Hydrogen evolution over bimetallic systems: Understanding the trends". *ChemPhysChem* 7.5 (2006), 1032–1035.

[31] Jeff Greeley and Manos Mavrikakis. "A First-Principles Study of Methanol Decomposition on Pt(111)". *Journal of the American Chemical Society* 124.24 (2002), 7193–7201.

[32] Bin Liu and Jeffrey Greeley. "Decomposition Pathways of Glycerol via C–H, O–H, and C–C Bond Scission on Pt(111): A Density Functional Theory Study". *The Journal of Physical Chemistry C* 115.40 (2011), 19702–19709.

[33] Cameron J Bodenschatz, Xiaohong Zhang, Tianjun Xie, Jeremy Arvay, Sapna Sarupria, and Rachel B Getman. "Multiscale sampling of a heterogeneous water/metal catalyst interface using density functional theory and force-field molecular dynamics". *JoVE (Journal of Visualized Experiments)* 146 (2019), e59284.

[34] Cameron J Bodenschatz, Sapna Sarupria, and Rachel B Getman. "Molecular-level details about liquid H2O interactions with CO and sugar alcohol adsorbates on Pt (111) calculated using density functional theory and molecular dynamics". *The Journal of Physical Chemistry C* 119.24 (2015), 13642–13651.

[35] Dirk Porezag and Mark R. Pederson. "Infrared intensities and Raman-scattering activities within density-functional theory". *Phys. Rev. B* 54 (11 Sept. 1996), 7830–7836.

[36] Hubert Cybulski and Joanna Sadlej. "On the calculations of the vibrational Raman spectra of small water clusters". *Chemical Physics* 342.1 (2007), 163–172.

[37] P. Bobadova-Parvanova, K. A. Jackson, S. Srinivas, M. Horoi, C. Köhler, and G. Seifert. "Scanning the potential energy surface of iron clusters: A novel search strategy". *Journal of Chemical Physics* 116.9 (2002), 3576–3587.

[38] Chengwu Yang et al. "Methanol adsorption on monocrystalline ceria surfaces". *Journal of Catalysis* 336 (2016), 116–125.

[39] Christian Schilling, Alexander Hofmann, Christian Hess, and M. Verónica Ganduglia-Pirovano. "Raman Spectra of Polycrystalline CeO2: A Density Functional Theory Study". *Journal of Physical Chemistry C* 121.38 (2017), 20834–20849.

[40] Trent L. Silbaugh, Javier B. Giorgi, Ye Xu, Aashani Tillekaratne, Francisco Zaera, and Charles T. Campbell. "Adsorption Energy of tert-Butyl on Pt(111) by Dissociation of tert-Butyl Iodide: Calorimetry and DFT". *Journal of Physical Chemistry C* 118.1 (2014), 427–438.

[41] E. Moreira, J.M. Henriques, D.L. Azevedo, E.W.S. Caetano, V.N. Freire, and E.L. Albuquerque. "Structural, optoelectronic, infrared and Raman spectra of orthorhombic SrSnO3 from DFT calculations". *Journal of Solid State Chemistry* 184.4 (2011), 921–928.

[42] Florencia C Calaza, Ye Xu, David R Mullins, and Steven Steve H Overbury. "Oxygen Vacancy-Assisted Coupling and Enolization of Acetaldehyde on CeO2(111)". *Journal of the American Chemical Society* 134.43 (2012), 18034–18045.

[43] Jeffrey A. Herron, Scott Tonelli, and Manos Mavrikakis. "Atomic and molecular adsorption on Pd(111)". *Surface Science* 606.3 (2018), 159–174.

[44] V. Milman et al. "Electron and vibrational spectroscopies using DFT, plane waves and pseudopotentials: CASTEP implementation". *Journal of Molecular Structure-theochem* 954.1 (2010), 22–35.

[45] Jennifer E Laaser, Jeffrey R Christianson, Tracey A Oudenhoven, Yongho Joo, Padma Gopalan, JR Schmidt, and Martin T Zanni. "Dye self-association identified by intermolecular couplings between vibrational modes as revealed by infrared spectroscopy, and implications for electron injection". *The Journal of Physical Chemistry C* 118.11 (2014), 5854–5861.

[46] Ask Hjorth Larsen et al. "The atomic simulation environment — a python library for working with atoms". *Journal of Physics: Condensed Matter* 29.27 (2017), 273002.

[47] D Loffreda, D Simon, and P Sautet. "Vibrational frequency and chemisorption site: a DFT-periodic study of NO on Pd (111) and Rh (111) surfaces". *Chemical physics letters* 291.1-2 (1998), 15–23.

[48] Ahmed M Abuelela, Tarek A Mohamed, and Oleg V Prezhdo. "DFT simulation and vibrational analysis of the IR and Raman spectra of a CdSe quantum dot capped by methylamine and trimethylphosphine oxide ligands". *The Journal of Physical Chemistry C* 116.27 (2012), 14674–14681.

[49] D Loffreda, D Simon, and P Sautet. "Dependence of stretching frequency on surface coverage and adsorbate–adsorbate interactions: a density-functional theory approach of CO on Pd (111)". *Surface science* 425.1 (1999), 68–80.

[50] Mouna Ben Yahia, Frederic Lemoigno, Thomas Beuvier, Jean-Sebastien Filhol, Mireille Richard-Plouet, Luc Brohan, and Marie-Liesse Doublet. "Updated references for the structural, electronic, and vibrational properties of TiO 2 (B) bulk using first-principles density functional theory calculations". *The Journal of chemical physics* 130.20 (2009), 204501.

[51] Matthew Neurock, Michael Janik, and Andrzej Wieckowski. "A first principles comparison of the mechanism and site requirements for the electrocatalytic oxidation of methanol and formic acid over Pt". *Faraday discussions* 140 (2009), 363–378.

[52] Tian Sheng, Xiao Lin, Zhao-Yang Chen, Peijun Hu, Shi-Gang Sun, You-Qun Chu, Chun-An Ma, and Wen-Feng Lin. "Methanol electro-oxidation on platinum modified tungsten carbides in direct methanol fuel cells: a DFT study". *Physical Chemistry Chemical Physics* 17.38 (2015), 25235–25243.

[53] Jungseob So, Yoona Chung, David S Sholl, and Carsten Sievers. "In-situ ATR-IR study of surface reaction during aqueous phase reforming of glycerol, sorbitol and glucose over Pt/γ-Al2O3". *Molecular Catalysis* 475 (2019), 110423.

[54] Chung S Kim, Carol Korzeniewski, and Wade J Tornquist. "Site specific co-adsorption at Pt (335) as probed by infrared spectroscopy: Structural alterations in the CO adlayer under aqueous electrochemical conditions". *The Journal of chemical physics* 100.1 (1994), 628–630.

[55] Guowen Peng and Manos Mavrikakis. "Adsorbate diffusion on transition metal nanoparticles". *Nano letters* 15.1 (2014), 629–634.

[56] Peter J Feibelman, Bjørk Hammer, Jens Kehlet Nørskov, F Wagner, Matthias Scheffler, Roland Stumpf, R Watwe, and J Dumesic. "The CO/Pt (111) puzzle". *The Journal of Physical Chemistry B* 105.18 (2001), 4018–4025.

[57] Christopher J Cramer and Donald G Truhlar. "Density functional theory for transition metals and transition metal chemistry". *Physical Chemistry Chemical Physics* 11.46 (2009), 10757–10816.

[58] R Alcala, M Mavrikakis, and James A Dumesic. "DFT studies for cleavage of C-C and C-O bonds in surface species derived from ethanol on Pt (111)". *Journal of Catalysis* 218.1 (2003), 178–190.

[59] Wei Liu, Alexandre Tkatchenko, and Matthias Scheffler. "Modeling adsorption and reactions of organic molecules at metal surfaces". *Accounts of chemical research* 47.11 (2014), 3369–3377.

[60] Reinhard J Maurer, Victor G Ruiz, Javier Camarillo-Cisneros, Wei Liu, Nicola Ferri, Karsten Reuter, and Alexandre Tkatchenko. "Adsorption structures and energetics of molecules on

metal surfaces: Bridging experiment and theory". *Progress in Surface Science* 91.2 (2016), 72–100.

Chapter 6

Conclusions and Recommendations

6.1 Conclusions

The protocol presented in Chapter 2 - Multi-scale Simulation Strategy and Its Application, is capable of modeling quantum and thermal phenomena in liquid phase heterogeneous catalysis. It is the first to our knowledge to incorporate quantum mechanics with complete sampling of an explicit liquid environment. Configurations of liquid molecules generated from this method represent those expected under actual reaction conditions and can be used to explore molecular-level phenomena that depend on the spatial arrangements of molecules, which can provide insight into the roles that solvent plays on liquid phase heterogeneous catalysis. For example, these obtained configurations can be used in a quantum mechanics or QM/MM simulation, or they could be used to analyze statistics related to the spatial positions of the molecules. This technique paves the way for future research to explore the roles that liquid reaction environments have on catalysis by generating realistic configurations of liquid molecules at catalytic interfaces.

The methods provided in Chapter 3 -A DFT and MD Study of Aqueous-phase Dehydrogenation of Glycerol on Pt (1 1 1): Comparing Chemical Accuracy versus Computational Expense in Different Methods for Calculating Aqueous-phase System Energies, presents a multi-scale modeling strategy that employs a linear scaling relationship to compute adsorbate binding energies and classical Lennard- Jones + Coulomb (LJ + C) potentials to calculate adsorbate interaction energies with liquid H_2O molecules. It is the first to our knowledge in adapting linear scaling relationship in aqueous phase reaction energy calculation. This method decreases the dependency of extensive

DFT calculations per adsorbate, while still incorporating the configurational disorder that is present in the liquid water structure. It also provides reasonable chemical accuracy in calculating aqueous-phase reaction energies of a MAE of 0.28 eV compared to the full DFT/MD method [1]. Overall, the LSR/MD is established to overcome the computational expense problems that exist in aqueous phase catalysis modeling, and it can be extended to thermodynamic intermediates and reactions screening of aqueous phase reactions.

In the work presented in Chapter 4 - Insights into the Roles of Water on the Aqueous Phase Reforming of Glycerol, presents our work towards further extending our usage of our developed multi-scale modeling ttechniquesto investigate various types of reactions that exisit within glycerol APR reaction network, which are dehydrogenation, decarbonlyation, and hydrogenolysis. We have used DFT calculations, MD simulations, linear scaling relationships, transition state scaling relationships to explore the thermodynamics and kinetics perspectives of those reactions. Combined with data from the literature, we constructed microkinetic models to simulation catalytic glycerol reforming under vacuum and aqueous phases. To gain insight of the roles of water molecules in glycerol APR, we calculated and included steps where H_2O molecules and $H_{2(n+1)}O_n$ species explicitly participate in the reactions. We concluded four roles of water molecules on the catalytic mechanism of aqueous phase reforming of glycerol from our microkinetic modeling results, they are: supplying OH* needed in water-gas shift to oxidize CO*, promoting C-H scissions, promoting O-H scissions, and inhibiting decarbonylation of C3 backbone. Our results also suggest that hydrogenolysis reactions would be facilitated in a low pH environment.

In the work presented in Chapter 5 - Computational Modeling of Methanol Decomposition on Pt Catalyst Supported by Alumina, expands our scope of study to more realistic catalyst modeling aimed to reflect two types of catalyst active sites exist in real catalyst, i.e. terrace and edge sites. We used the advanced model investigated thermodynamics of binding, diffusion, and reactions within the dehydrogenation reaction network of methanol. Furthermore, our routines of vibrational frequency calculation is more robust than the commonly used method and matches key locations from experimental spectra. By analyzing computationally and experimentally yielded spectra data, we can deduce the dominant species on a particular type of binding sites which is a question that is still outstanding in the literature. Our studies on thermodynamic energy calculations on chemical binding and reactions on terrace sites can successfully relate to other published results while supplying more perspectives to the overall chemistry with our findings on chemical binding and reactions on

edge sites. Our generated IR spectra from vibrational frequency calculations can achieve good agreement with our experimental collaborator's past and current findings. This is an important step that brings our methods closer to our long term goal, which is using computational approaches to gain insights of the catalytic species and reactions, and facilitate new catalyst research and development.

To summarize, in this thesis, different multi-scale simulation methods are assessed, among which the LSR/MD method was chosen to calculate reaction thermodynamics due its tested balance in accuracy and efficiency. Additionally, TSS relations are implemented to fast estimate kinetics of various types of reactions within DFT accuracy. Once thermodynamics and kinetics information are gathered, microkinetic modeling simulations are conducted, in attempt to simulate a total over 300 hundred elementary reaction steps of glycerol APR under realistic reacting conditions, i.e. initial composition, temperature and pressure. The results from microkinetic modeling can reach good agreement in production distribution and selectivity of experimental results from existing literature. These results show that the multi-scale modeling, LSR, and TSS approaches are able to capture experimentally observed phenomena. Further, the development of the LSR and TSS is what makes this possible, since simulating such a large reaction network would be computationally intractable using the multi-scale modeling approach alone. Last but not least, a more advanced catalyst model that includes support in the catalyst surface is used for the study of methanol decomposition. This more advanced model features two types of active sites, allowing us to gain more knowledges of preferred binding, preferred reaction pathways, and dominant surface species on different active sites. Our results can reproduce and agree with existing literature and findings by our experimental collaborator.

6.2 Recommendations

6.2.1 Apply Different Force-Field Current Multi-scale Modeling Method

Our current multi-scale modeling method the first to our knowledge that combines DFT and MD calculations which has the capability to sample and calculate varying system configurations in the aqueous phase and their corresponding energies. This method is based on the work flow of DFT $\rightarrow$ MD $\rightarrow$ DFT simulations. Extra steps can be taken to atone the difference in energy potentials between DFT and MD methods, such as a re-optimize step after the MD sampling. However, the concern of fixating the surface during MD simulations is still in need of remedy. The current state

of undertaking this method is from the lack of appropriate force fields (FFs) in MD. In future work, I recommend applying ReaxFF (Reactive Force Field), which is a bond order-based force field developed by Adri van Duin, William A. Goddard, III, and co- workers at the California Institute of Technology [2]. In contrast to traditional force fields are unable to model chemical reactions because of the requirement of breaking and forming bonds, ReaxFF eschews explicit bonds in favor of bond orders, which allows for continuous bond formation/breaking. ReaxFF aims to be as general as possible and has been parameterized and tested for hydrocarbon reactions, alkoxysilane gelation, transition-metal-catalyzed nanotube formation, and high-energy materials. Recently, ReaxFF has been developed to study oxygen interactions with realistic silica surfaces. This version of ReaxFF is based on highly accurate and benchmarking density functional studies. Highly accurate density functional results are achieved by employing Minnesota Functionals [3–6].

Another recommendation is to develop in-house FFs. Dr. Paul Meza-Morales in our group made great progress in realizing methanol adsorption and desorption on Pt(1 1 1) surface as regards the FFs predicted and DFT calculated energies under aqueous phase environment. Indeed this is a painstaking step in the work but the results are rewarding. In his most recent report the FFs reached great accuracy in reproducing the binding energies of methanol on Pt(1 1 1) as the RMSE for in-plane configurations remains as low as 0.0628 eV when compared to DFT calculated energies (The out-of-plane configurations have not been included as of the writing of this dissertation).

6.2.2 Exponential Pre-factor Calculation

Complete representation of the reaction kinetics requires knowledges of reaction heat, reaction barriers and pre-exponential factos. Pre-exponential factors, as one of the key information needed in Arrhenius equation [7, 8], are often estimated. If a more precise description is in need, it can be calculated from construction of eigenfrequencies based on Vineyard equation [9–11]. The methodology is decribed in equation in the following Eqn (6.1),

$$A = \frac{\prod_{3N-6}^{i=1} v_i}{\prod_{3N-7}^{i=1} v_i'} \tag{6.1}$$

where v_i are the eigenfrequencies of vibrations of the cluster in the state corresponding to the minimum of the potential energy for all 3N - 6 normal coordinates, and v_i' are the frequencies of vibrations at the saddle point corresponding to the maximum of potential energy for one normal

coordinate and to the minimum for all the other coordinates.

6.2.3 Workflow in Thermochemical and Kinetic Parameter Estimation

Estimating the thermo-chemical properties of systems is important in many fields such as material science and catalysis. D.G. Vlachos and his team has developed a Python based multiscale thermochemistry toolbox, named pMuTT [12]. It is a Python software library aimed to streamline the conversion of ab-initio data to thermo-chemical properties using statistical mechanics, to perform thermodynamic analysis, and to create input files for kinetic modeling software. The core classes developed include a statistical mechanical model in which energy modes can be included or excluded to suit the application, empirical models for rapid thermodynamic property estimation, and a reaction model to calculate kinetic parameters or changes in thermodynamic properties. In addition, pMuTT supports other features, such as Brønsted–Evans–Polanyi (BEP) relationships, coverage effects, and even ab-initio phase diagrams.

Adaptation of this package can increase the productivity and possibly bring more stability in the thermo-chemical and kinetic parameters that will be used in microkinetic modeling, since the package is equipped with statistical mechanical and empirical handlers.

6.2.4 Parameter Tuning for Faster Electronic Structure Convergence

Electronic structure convergence can be an issue for DFT calculations of systems of large size and complicated atom compositions. For example, during the calculations of the IR spectra of different species based on different catalyst models, it is observed that same chemical species bound to the terrace Pt(1 1 1) can reach electronic convergence a lot faster than that from the Pt_4/Al_2O_3 surface. Technically the latter system contains a lot less heavy Pt atoms and thus less plane-waves are needed to describe the system (given the two catalyst system cells have similar volume). Changing the mixing rules of eigenvalues of the charge dielectric matrix from conjugate gradient algorithm preconditioned rule [13] to a linear rule can yield a good speed boost for Pt_4/Al_2O_3 surface. The following are the changes to make in INCAR input file for VASP calculations,

AMIX = 0.2,

BMIX = 0.0001,

AMIX_MAG = 0.8,

BMIX_MAG = 0.0001,

This is particularly good for metal oxides but will still struggle for metals like conjugate gradient preconditioned rule. Since the Pt_4/Al_2O_3 catalyst model consists primarily of Al_2O_3 rather than pure Pt metal. Adaptation of the linear mixing rule was made. As a result, the convergence speed achieved about 2x of boost, therefore for future studies on systems containing considerable metal oxides, the linear mixing rule is recommended.

6.3 References

[1] Cameron J Bodenschatz, Sapna Sarupria, and Rachel B Getman. "Molecular-Level Details about Liquid H2O Interactions with CO and Sugar Alcohol Adsorbates on Pt (111) Calculated Using Density Functional Theory and Molecular Dynamics". *The Journal of Physical Chemistry C* 119.24 (2015), 13642–13651.

[2] Adri CT Van Duin, Siddharth Dasgupta, Francois Lorant, and William A Goddard. "ReaxFF: a reactive force field for hydrocarbons". *The Journal of Physical Chemistry A* 105.41 (2001), 9396–9409.

[3] Narbe Mardirossian and Martin Head-Gordon. "Characterizing and understanding the remarkably slow basis set convergence of several Minnesota density functionals for intermolecular interaction energies". *Journal of chemical theory and computation* 9.10 (2013), 4453–4461.

[4] Lars Goerigk. "Treating London-dispersion effects with the latest Minnesota density functionals: problems and possible solutions". *The journal of physical chemistry letters* 6.19 (2015), 3891–3896.

[5] Narbe Mardirossian and Martin Head-Gordon. "How accurate are the Minnesota density functionals for noncovalent interactions, isomerization energies, thermochemistry, and barrier heights involving molecules composed of main-group elements?" *Journal of chemical theory and computation* 12.9 (2016), 4303–4325.

[6] DeCarlos E Taylor et al. "Blind test of density-functional-based methods on intermolecular interaction energies". *The Journal of chemical physics* 145.12 (2016), 124105.

[7] Svante Arrhenius. "Über die Dissociationswärme und den Einfluss der Temperatur auf den Dissociationsgrad der Elektrolyte". *Zeitschrift für physikalische Chemie* 4.1 (1889), 96–116.

[8] Svante Arrhenius. "Über die Reaktionsgeschwindigkeit bei der Inversion von Rohrzucker durch Säuren". *Zeitschrift für physikalische Chemie* 4.1 (1889), 226–248.

[9] George H Vineyard. "Frequency factors and isotope effects in solid state rate processes". *Journal of Physics and Chemistry of Solids* 3.1-2 (1957), 121–127.

[10] Handan Yildirim, Abdelkader Kara, Sondan Durukanoglu, and Talat S Rahman. "Calculated pre-exponential factors and energetics for adatom hopping on terraces and steps of Cu (1 0 0) and Cu (1 1 0)". *Surface science* 600.2 (2006), 484–492.

[11] Henry H Wu and Dallas R Trinkle. "Direct diffusion through interpenetrating networks: Oxygen in titanium". *Physical review letters* 107.4 (2011), 045504.

[12] Jonathan Lym, Gerhard R Wittreich, and Dionisios G Vlachos. "A Python Multiscale Thermochemistry Toolbox (pMuTT) for thermochemical and kinetic parameter estimation". *Computer Physics Communications* (2019), 106864.

[13] Martin Fodslette Møller. "A scaled conjugate gradient algorithm for fast supervised learning". *Neural networks* 6.4 (1993), 525–533.

[14] Stefan Grimme, Stephan Ehrlich, and Lars Goerigk. "Effect of the damping function in dispersion corrected density functional theory". *Journal of computational chemistry* 32.7 (2011), 1456–1465.

Appendices

Appendix A GPU Parallelization in VASP

A.1 Hardware Requirement

It is generally recommended to use GPU architecture with Kepler or newer: Tesla K40 or Tesla K80, with 12 and 24 GB memory respectively, are strongly recommended.

Tesla K20 and Tesla K20, with 5 GB and 6 GB respectively, may run out of memory on larger problems. In fact, a small system (27 Pt atoms) will often run into K20 memory issues.

Therefore K40 or newer GPU is strongly recommended.

The most important thing to make VASP run efficiently is to make sure that you have the MPS system active on the node. MPS is the "Multi Process Service" – it virtualizes the GPU so that many MPI ranks can access the GPU independently without of having to wait for each other. Nvidia has an overview on their web site describing MPS and how set it up. Basically, the user need to check if the nvidia-cuda-mps-control process is running. If it is not, user can manually start such process in their bash script when submitting a new GPU-VASP job.

$ mkdir /tmp/nvidia-mps

$ export CUDA_MPS_PIPE_DIRECTORY=/tmp/nvidia-mps

$ mkdir /tmp/nvidia-log

$ export CUDA_MPS_LOG_DIRECTORY=/tmp/nvidia-log

$ nvidia-cuda-mps-control -d

A.2 VASP Input

It is also important to set input parameters in the INCAR file correctly, details of the parameterization regarding parallelization will be discussed later. GPU-VASP requires

LREAL = .TRUE.

LCALCEPS = .FALSE.

LSCAAWARE = .FALSE.

NCORE = 1.

The GPU version of VASP has no gamma point optimizations therefore no gamma point settings in the KPOINTS file should appear.

If the GPU-VASP is initialized successfully, a message in the output file should be expected:

WARNING: The GPU port of VASP has been extensively

tested for: ALGO=Normal, Fast, and VeryFast.

Other algorithms may produce incorrect results or

yield suboptimal performance. Handle with care!

POSCAR, INCAR and KPOINTS ok, starting setup

creating 32 CUDA streams...

creating 32 CUDA streams...

creating 32 CUDA streams...

creating 32 CUDA streams...

creating 32 CUDA streams...

creating 32 CUDA streams...

creating 32 CUDA streams...

creating 32 CUDA streams...

creating 32 CUDA streams...

creating 32 CUDA streams...

creating 32 CUDA streams...

creating 32 CUDA streams...

creating 32 CUDA streams...

creating 32 CUDA streams...

creating 32 CUDA streams...

creating 32 CUDA streams...

creating 32 CUFFT plans with grid size 100 x 48 x 56...

creating 32 CUFFT plans with grid size 100 x 48 x 56...

creating 32 CUFFT plans with grid size 100 x 48 x 56...

creating 32 CUFFT plans with grid size 100 x 48 x 56...

creating 32 CUFFT plans with grid size 100 x 48 x 56...

creating 32 CUFFT plans with grid size 100 x 48 x 56...

creating 32 CUFFT plans with grid size 100 x 48 x 56...

creating 32 CUFFT plans with grid size 100 x 48 x 56...

creating 32 CUFFT plans with grid size 100 x 48 x 56...

creating 32 CUFFT plans with grid size 100 x 48 x 56...

creating 32 CUFFT plans with grid size 100 x 48 x 56...

creating 32 CUFFT plans with grid size 100 x 48 x 56...

creating 32 CUFFT plans with grid size 100 x 48 x 56...

creating 32 CUFFT plans with grid size 100 x 48 x 56...

creating 32 CUFFT plans with grid size 100 x 48 x 56...

creating 32 CUFFT plans with grid size 100 x 48 x 56...

FFT: planning ...

A.3 Optimization on Parallelization

KPAR parallelization is strongly recommended since it is well tested and it exhibits almost linear boost in the performance. It is adviced to use the KPAR number as high as possible, but the consequence of this practise is that the memory demand increases significantly with high KPAR numbers.

The parameter that affects the performance of parallelization next to KPAR is NPAR, normally a good recommendation of setting NPAR is,

NPAR = $\approx \sqrt{\text{number of cores}}$

The parameter that affects the performance of parallelization next to NPAR is NSIM. A good approximation of NSIM tag is,

NSIM = NBANDS / (2*cores)

The settings of KPAR and NPAR are not tribute, that often the optimal combination of these two are determined by running benchmark tests. Jonathan Skelton from University of Bath has developed an excellent repository on Github that can benchmark the above three parameters in an automated workflow,

https://github.com/JMSkelton/VASP-GPU-Benchmarking/tree/master/Scripts

Only minor changes are needed to conduct such benchmark testings, and it can be submitted as a regular PBS job. The ket modification needed is to set up the arrays for the iteration of KPAR, NPAR and NSIM. Detailed settings are set in GPUTest.py in the repository. The array controlling KPAR iteration is at Line 20; the array for controlling NPAR iteration is at Line 6; and the array for controlling NPAR iteration is at Line 10.

Appendix B Supplemental Materials for DFT Calculations in VASP

The following VASP input INCAR parameters are attached as following, for geometry optimization simulations. Note that the D2 values appeared in the INCAR are intended for a system consisting of Pt, C, O, and H atoms.

NWRITE = 1

LWAVE = .FALSE. ! write WAVECAR?

LCHARG = .FALSE. ! write CHGCAR?

LVTOT = .FALSE. ! write LOCPOT?

Electronic relaxation

IALGO = 48 ! 8: CG, 48: DIIS algorithm for electrons

ENCUT = 400

ALGO = Fast

ISMEAR = 0 ! 0: Gaussian, electron smearing

SIGMA = 0.100

PREC = accurate

LREAL = Auto

ROPT = 2e-4 2e-4 2e-4 2e-4

ISTART = 0

ADDGRID = T

NELM = 1000

NELMIN = 6

EDIFF = 1e-6

ISPIN = 1 ! polarization

IDIPOL = 3

Ionic relaxation

NSW = 300 ! # of steps in optimization (default 0!)

ISIF = 2 ! 0: relax ions, 1,2:relax ions,calc stresses, 3:relax ion+cell

IBRION = 1 ! 1: quasi-NR, 2:CG algorithm for ions

NFREE = 10 ! number of DIIS vectors to save

POTIM = 0.35 ! reduce trial step in optimization

EDIFFG = -0.03

Dispersion

LVDW = .TRUE.

VDW_C6 = 42.440 1.750 0.700 0.140

VDW_R0 = 1.750 1.452 1.342 1.001

DOS

RWIGS = 1.300 0.770 0.730 0.320 ! Wigner-Seitz radii

The following VASP input INCAR parameters are attached as following, for geometry optimization simulations with D3 dispersion correction with Becke and Johnson damping (BJ-damping) [14]. Note that the D3 values are implemented in VASP executable by default. If customization of the parameters is needed, `https://www.chemie.uni-bonn.de/pctc/mulliken-center/software/dft-d3/get-the-current-version-of-dft-d3` has the information.

NWRITE = 1

LWAVE = .FALSE. ! write WAVECAR?

LCHARG = .FALSE. ! write CHGCAR?

LVTOT = .FALSE. ! write LOCPOT?

Electronic relaxation

IALGO = 48 ! 8: CG, 48: DIIS algorithm for electrons

ENCUT = 400

ALGO = Fast

ISMEAR = 0 ! 0: Gaussian, electron smearing

SIGMA = 0.100

PREC = accurate

LREAL = Auto

ROPT = 2e-4 2e-4 2e-4 2e-4

ISTART = 0

ADDGRID = T

NELM = 1000

NELMIN = 6

EDIFF = 1e-6

ISPIN = 1 ! polarization

IDIPOL = 3

Ionic relaxation

NSW = 300 ! # of steps in optimization (default 0!)

ISIF = 2 ! 0: relax ions, 1,2:relax ions,calc stresses, 3:relax ion+cell

IBRION = 1 ! 1: quasi-NR, 2:CG algorithm for ions

NFREE = 10 ! number of DIIS vectors to save

POTIM = 0.35 ! reduce trial step in optimization

EDIFFG = -0.03

Dispersion

IVDW = 12

DOS

RWIGS = 1.300 0.770 0.730 0.320 ! Wigner-Seitz radii

VASP provides the functionality for regular NEB calculation. Recent developed vtstool by Henkelman XXX implented climibing image to the VASP package. Below is a typical VASP setting for a cNEB simulation for system that consists of Pt, C, O and H atoms. It is to be noted that the dimer simulation utilizes the vtstool extension, thus requiure VASP to be re-compiled with the vtstool source codes.

NWRITE = 1

LWAVE = .FALSE. ! write WAVECAR?

LCHARG = .FALSE. ! write CHGCAR?

LVTOT = .FALSE. ! write LOCPOT?

Electronic relaxation

ENCUT = 400

ALGO = Fast

ISMEAR = 0 ! 0: Gaussian, electron smearing

SIGMA = 0.100

PREC = med

LREAL = Auto

LCLIMB = .TRUE.

IMAGES = 5

ISTART = 0

NELM = 40

EDIFF = 1e-6

ISPIN = 1 ! polarization?

IDIPOL = 3

Ionic relaxation

NSW = 500 ! # of steps in optimization (default 0!)

ISIF = 2 ! 0: relax ions, 1,2:relax ions,calc stresses, 3:relax ion+cell

IBRION = 1 ! 1: quasi-NR, 2:CG algorithm for ions

NFREE = 40 ! number of DIIS vectors to save

POTIM = 0.5 ! reduce trial step in optimization

EDIFFG = -0.5

Dispersion

LVDW = .TRUE.

VDW_C6 = 42.440 1.750 0.700 0.140

VDW_R0 = 1.750 1.452 1.342 1.001

DOS

RWIGS = 1.300 0.770 0.730 0.320 ! Wigner-Seitz radii

The following INCAR parameters are intended for dimer simulations in search for saddle points in VASP, for a system consists of Pt, C, O, and H atoms. It is to be noted that the dimer simulation utilizes the vtstool extension (same as seen for cNEB simulations), thus requiure VASP to be re-compiled with the vtstool source codes.

NWRITE = 1

LWAVE = .FALSE. ! write WAVECAR?

LCHARG = .FALSE. ! write CHGCAR?

LVTOT = .FALSE. ! write LOCPOT?

LSCAAWARE = .FALSE.

Electronic relaxation

IALGO = 48 ! 8: CG, 48: DIIS algorithm for electrons

ENCUT = 400

ALGO = Fast

ISMEAR = 0 ! 0: Gaussian, electron smearing

SIGMA = 0.100

PREC = normal

LREAL = Auto

ISTART = 0

NELM = 40

EDIFF = 1e-7

ISPIN = 1 ! polarization?

IDIPOL = 3

Ionic relaxation

NSW = 500 ! number of steps in optimization (default 0!)

ISIF = 2 ! 0: relax ions, 1,2:relax ions,calc stresses, 3:relax ion+cell

IBRION = 3 ! 1: quasi-NR, 2:CG algorithm for ions

NFREE = 4 ! number of DIIS vectors to save

EDIFFG = -0.03

Dimer setup

ICHAIN = 2

IOPT = 2

POTIM = 0.0 ! reduce trial step in optimization

DRotMax = 1 ! max rotation step each dimer iteration

Dispersion

LVDW = .TRUE.

VDW_C6 = 42.440 1.750 0.700 0.140

VDW_R0 = 1.750 1.452 1.342 1.001

DOS

RWIGS = 1.300 0.770 0.730 0.320 ! Wigner-Seitz radii

The following INCAR parameters are intended for vibrational mode simulations in calculating vibrational frequencies in VASP, for a system that is previously converged from dimer calculations.

NWRITE = 1

LWAVE = .FALSE. ! write WAVECAR?

LCHARG = .FALSE. ! write CHGCAR?

LVTOT = .FALSE. ! write LOCPOT?

Electronic relaxation

IALGO = 48 ! 8: CG, 48: DIIS algorithm for electrons

ENCUT = 400

ALGO = Fast

ISMEAR = 0 ! 0: Gaussian, electron smearing

SIGMA = 0.100

PREC = normal

LREAL = Auto

ISTART = 0

NELM = 40

EDIFF = 1e-6

ISPIN = 1 polarization?

IDIPOL = 3

Ionic relaxation

NSW = 1 ! # of steps in optimization (default 0!)

ISIF = 2 ! 0: relax ions, 1,2:relax ions,calc stresses, 3:relax ion+cell

IBRION = 5 ! 1: quasi-NR, 2:CG algorithm for ions

NFREE = 2 ! number of DIIS vectors to save

POTIM = 0.015 ! reduce trial step in optimization

EDIFFG = -0.03

Dispersion

LVDW = .TRUE.

VDW_C6 = 42.440 1.750 0.700 0.140

VDW_R0 = 1.750 1.452 1.342 1.001

DOS

RWIGS = 1.300 0.770 0.730 0.320 ! Wigner-Seitz radii

The following INCAR parameters are intended for single point DFT calculations in calculating system electronic energies without perturbing the geometries in VASP.

NWRITE = 1

LWAVE = .FALSE. ! write WAVECAR?

LCHARG = .FALSE. ! write CHGCAR?

LVTOT = .FALSE. ! write LOCPOT?

Electronic relaxation

IALGO = 48 ! 8: CG, 48: DIIS algorithm for electrons

ENCUT = 400

ALGO = Fast

ISMEAR = 0 ! 0: Gaussian, electron smearing

SIGMA = 0.100

PREC = accurate

LREAL = Auto

ROPT = 2e-4 2e-4 2e-4 2e-4

ISTART = 0

ADDGRID = T

NELM = 1000

NELMIN = 6

EDIFF = 1e-6

ISPIN = 1 ! polarization

IDIPOL = 3

Ionic relaxation

NSW = 0 ! # of steps in optimization (default 0!)

ISIF = 2 ! 0: relax ions, 1,2:relax ions,calc stresses, 3:relax ion+cell

IBRION = 1 ! 1: quasi-NR, 2:CG algorithm for ions

NFREE = 10 ! number of DIIS vectors to save

POTIM = 0.35 ! reduce trial step in optimization

EDIFFG = -0.03

Dispersion

LVDW = .TRUE.

VDW_C6 = 42.440 1.750 0.700 0.140

VDW_R0 = 1.750 1.452 1.342 1.001

DOS

RWIGS = 1.300 0.770 0.730 0.320 ! Wigner-Seitz radii

Likewise in the previous chapter, the INCAR for single point calculation, with D3 dispersion correction (BJ damping enabled) is attached.

NWRITE = 1

LWAVE = .FALSE. ! write WAVECAR?

LCHARG = .FALSE. ! write CHGCAR?

LVTOT = .FALSE. ! write LOCPOT?

Electronic relaxation

IALGO = 48 ! 8: CG, 48: DIIS algorithm for electrons

ENCUT = 400

ALGO = Fast

ISMEAR = 0 ! 0: Gaussian, electron smearing

SIGMA = 0.100

PREC = accurate

LREAL = Auto

ROPT = 2e-4 2e-4 2e-4 2e-4

ISTART = 0

ADDGRID = T

NELM = 1000

NELMIN = 6

EDIFF = 1e-6

ISPIN = 1 ! polarization

IDIPOL = 3

Ionic relaxation

NSW = 0 ! # of steps in optimization (default 0!)

ISIF = 2 ! 0: relax ions, 1,2:relax ions,calc stresses, 3:relax ion+cell

IBRION = 1 ! 1: quasi-NR, 2:CG algorithm for ions

NFREE = 10 ! number of DIIS vectors to save

POTIM = 0.35 ! reduce trial step in optimization

EDIFFG = -0.03

Dispersion

IVDW = 12

Appendix C CO Binding on Terrace and Edge Sites

This appendix is intended for examination of CO and its binding on various terrace and edge sites. The representative bound CO, the ones show the strongest binding strength on the surfaces are reported in Chapter 5.

C.1 Binding Geometries

Configurations of CO bound on various types of sites are shown in the graph below. For the illustration of the geometries for CO bound on terrace sites, the top view is rendered for the best result. For the illustration of the geometries for CO bound on edge sites, the side view is rendered for the best result.

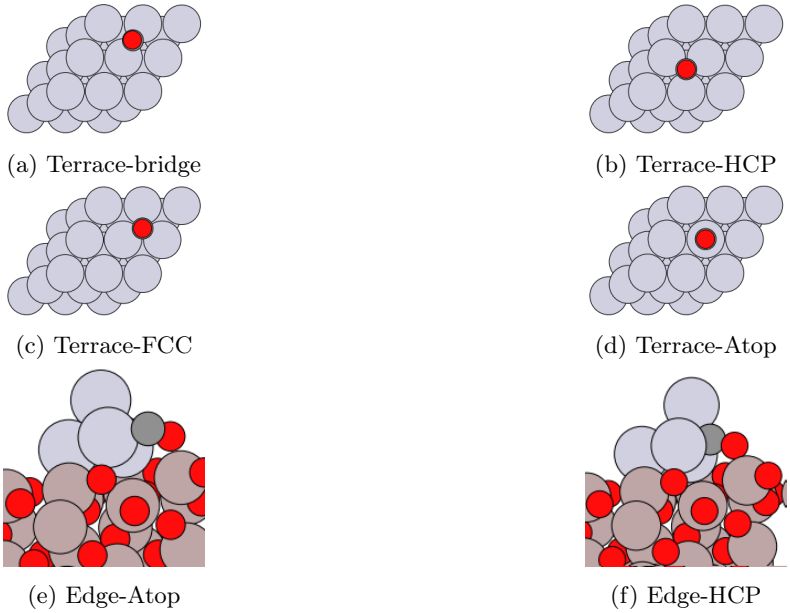

(a) Terrace-bridge (b) Terrace-HCP

(c) Terrace-FCC (d) Terrace-Atop

(e) Edge-Atop (f) Edge-HCP

Figure 1: Visualization of CH_3OH*, CH_2OH*, CHOH*, COH*, CH_3O*, CH_2O*, CHO*, CO* on Pt(1 1 1) terrace sites. Color key: Grey: Pt, Red: O, Dark grey: C, White: H.

It is found that CO approaches the Pt atoms via C on both terrace sites and edge sites. CO bound on terrace sites will always have a upward configuration, while CO bound on edge sites will tend to have a flat configuration due to the interaction of O atom with Al atom from the support.

C.2 Binding Energies

Specifications of how DFT calculations are conducted are discussed in Chapter 2. The top layer of Pt and the CO adsorbate are unfixed. Binding energies are calculated according to Eqn (5.1) in Chapter 5. The gas phase energy is calculated in reference to CO molecule since CO itself is considered a saturated species. The binding energies of CO on different binding sites are listed in the following table.

Table 1: Binding energies for CO on terrace and edge sites. Energy unit in eV (1 eV = 96.485 kJ/mol).

Binding Site	**Binding Energy**
Terrace-bridge	-2.24
Terrace-HCP	-2.23
Terrace-FCC	-2.23
Terrace-Atop	-2.10
Edge-Atop	-2.30
Edge-HCP	-2.40

By observing the calculated binding energies, it can be concluded that CO on terrace-bridge site exhibits the strongest binding strength among all terrace sites, and CO on edge-HCP site exhibits the stronger binding strength between the edge sites. Therefore the CO on terrace-bridge and CO on edge-HCP are of the strongest binding strength therefore they are chosen as the representative CO binding configuration for more studies in Chapter 5.

Appendix D Vibrational Frequency Calculations in VASP with ASE Interface

D.1 Environment Requirement

It is generally recommended to use CPU-VASP to conduct vibrational frequency calculations, espeically when VASP interfaces with ASE, it is not well know how GPU-VASP would behave.

The prerequirets are VASP, Python and OpenMPI support.

export VASP_COMMAND should be defined in the submission script for functions from ASE sourcing the VASP executable.

export VASP_PP_PATH should be also defined in the submission script for functions from ASE locating various pseudopotential (PPs).

The submission script should also activate the dependencies of ASE. This can be easily achieved by installing ASE under an Anaconda virtual environment and activating Anaconda after installation.

D.2 ASE Script in Python

A Python script that sources ASE libraries can be as following,

```
from mpi4py import MPI
from ase.io import read
from ase.calculators.vasp import Vasp
from ase.vibrations import Infrared
import ase.io.vasp
import os, sys
system = read('POSCAR',format="vasp", parallel = False) # read pre-relaxed structure of system
calc = Vasp(prec='Accurate',
            ialgo = 48,
            ediff = 1E-6,
            encut = 300.0,
            isym = 0,
```

```
                icharg = 1,
                pp = 'PBE', # will automatically construct POTCAR, INCAR, KPOINTS
                idipol = 4, # calculate the total dipole moment
                kpts = [7,7,1], # need to change for gas or adsorbed state
                gamma = True,
                dipol = system.get_center_of_mass(scaled=True),
                npar = 4,
                nsim = 4,
                ldipol = True,
                lcharg = True,
                lwave = True,
                nelm = 200,
                ivdw = 12)
system.set_calculator(calc) # run VASP
ir = Infrared(system,indices = [27,28])
ir.run()
ir.summary()
ir.write_spectra()
```

The *system* step defines the input of POSCAR;

The *calc* step defines calculator as VASP executable in ASE, and ASE initializes other VASP input as specified in this line;

The *system.set_calculator(calc)* and *ir* steps initialize iterative workload for the vibrational frequency calculations;

The *ir.run()* runs VASP iteratively by perturbing the geometry and recording all the force matrices;

The *ir.summary()* and *ir.write_spectra()* output the final projected IR spectra data in a .dat file.